DC Anisotropic Resistivity Sensitivity and Inversion

presented by

Timothy C. Wiese
B.Sc. Hons. (Physics)

THE UNIVERSITY
of ADELAIDE

The University of Adelaide
School of Chemistry and Physics
Discipline of Physics

Submitted in fulfilment of the requirements for the degree of Doctor of Philosophy

March 2012

Contents

Abstract

Many rocks and layered/fractured sequences have a clearly expressed electrical anisotropy, although it is rare in practice to incorporate anisotropy into the interpretation of electrical resistivity survey data. This thesis comprises a series of journal papers directed at increasing understanding of electrical anisotropy in resistivity investigations. Particular attention is given to how anisotropy affects both forward modelling and the resistivity inverse problem.

Chapter 2 derives the analytic solutions for the electric potential, current density and Fréchet derivatives inside a 3D tilted transversely isotropic medium. The solutions hold for a surface current source above an anisotropic but otherwise homogeneous medium. Profiles for potential, current density and sensitivity are presented for various strike and dip orientations of the axis of symmetry. Equipotentials exhibit an elliptical pattern and are not orthogonal to the current density vectors. Sensitivity patterns are strongly asymmetric compared to the isotropic case, with strong dependence on the axis of symmetry direction.

Chapter 3 presents a general numerical formulation for calculating the electric potential and Fréchet derivatives in an arbitrary 3D anisotropic heterogeneous medium. It is based on a new Gaussian quadrature grid formulation for calculating the 3D Green's functions. Explicit expressions for the Green's functions and their gradients are developed. A critical factor in the equations is the derivative of the conductivity tensor with respect to the principal conductivity values and angles defining the axes of symmetry. Special cases such as an isotropic earth and tilted transversely isotropic media emerge from the general solutions.

Chapter 4 makes use of the given analytic and numerical sensitivity formulations to examine the various sensitivity patterns which emerge for different uniform anisotropic media and for various surface electrode array configurations. Pole-pole, pole-dipole, Wenner and square arrays produce distinctive patterns, valuable in assessing resolution. It was found that sensitivity patterns vary greatly for different anisotropic model parameters in terms of strength and shape, depending on the nature of the anisotropy.

Chapter 5 presents a reformulation for the description of anisotropic media in terms of the coefficient of anisotropy λ and the geometric mean (average) conductivity σ_m. Sensitivity functions are plotted and described for these parameters. Also comparison of sensitivity patterns for isotropic, homogeneous models with those for equivalent transversely isotropic medium parameters is given by plotting the ratios of the Fréchet derivatives of the anisotropic to the isotropic values. Prominent differences in both sign and magnitude are observed, especially for steep dips and strong anisotropy. The plots highlight the dangers of an isotropic assumption. Even for mildly anisotropic rock ($\lambda < 1.2$), there is potential for error in interpretation.

Chapter 6 presents 2.5D synthetic inversion experiments for various electrode configurations and anisotropic models. The experiments compare image reconstructions obtained using the correct anisotropic inversion code and those obtained using the false but widely used isotropic assumption. Superior reconstruction in terms of reduced data misfit, true anomaly shape and position is obtained when the correct anisotropic assumption is employed. When an isotropic inversion algorithm is used to invert anisotropic data, the images are dominated by patterns of banded artefacts and high data misfits. Various data sets were investigated and evaluated for the accuracy of the inversion result, the corresponding eigenspectra (information content) of the pseudo Hessian matrix and the relative resolution plots. An effective data selection strategy based on high sensitivity measurements is presented. It drastically reduces the

number of data to be inverted but still produces comparable results to that obtained from the comprehensive data set. Inversion was carried out using transversely isotropic model parameters described in two different co-ordinate frames for the conductivity tensor: Cartesian versus natural or eigenframe. The Cartesian frame provided a more stable inversion product. This can be explained by the differing magnitudes of the eigenspectra of the pseudo-Hessian matrix for the two model descriptions.

Originality Statement

I, Timothy Wiese certify that this work contains no material which has been accepted for the award of any other degree or diploma in any university or other tertiary institution and, to the best of my knowledge and belief, contains no material previously published or written by another person, except where due reference has been made in the text.

I give consent to this copy of my thesis when deposited in the University Library, being made available for loan and photocopying, subject to the provisions of the Copyright Act 1968.

The author acknowledges that copyright of published works contained within this thesis (as listed below *) resides with the copyright holder(s) of those works.

I also give permission for the digital version of my thesis to be made available on the web, via the University's digital research repository, the Library catalogue, the Australian Digital Theses Program (ADTP) and also through web search engines, unless permission has been granted by the University to restrict access for a period of time.

Timothy Wiese
March 2012

*** Publications Arising out of this Research:**

1. Greenhalgh S.A., Marescot L., Zhou B., Greenhalgh M., Wiese T.C., 2009. Electric potential and Fréchet derivatives for a uniform anisotropic medium with a tilted axis of symmetry. *Pure and Applied Geophysics* **166**, 673 – 699.

2. Greenhalgh S.A., Zhou B., Greenhalgh M., Marescot L., Wiese T.C., 2009. Explicit expressions for the Fréchet derivatives in 3D anisotropic resistivity inversion. *Geophysics* **74**, 31 – 43.

3. Wiese T.C., Greenhalgh S.A., Marescot L., 2009. DC Resistivity sensitivity patterns for tilted transversely isotropic media. *Near Surface Geophysics* **7**, 125 – 139.

4. Greenhalgh S.A., Wiese T.C., Marescot L., 2010. Comparison of DC sensitivity patterns for anisotropic and isotropic media. *Journal of Applied Geophysics* **70**, 103 – 112.

5. Wiese T., Greenhalgh S.A., Zhou B., 2011. Resistivity inversion in 2D anisotropic media: numerical experiments. *Geophysical Prospecting*, (accepted subject to moderate revision, 2011).

Bibliographic Data:

1. Pure and Applied Geophysics
Published by Springer
ISSN 0033-4553 (printed)
ISSN 1420-9136 (electronic)

2. Geophysics
Published by Society of Exploration Geophysicists (SEG)
ISSN: 0016-8033

3. Near Surface Geophysics
Published by European Association of Geoscientists and Engineers (EAGE)
ISSN: 1569-4445

4. Journal of Applied Geophysics
Published by Elsevier Science
ISSN: 0926-9851

5. Geophysical Prospecting
Published by John Wiley and Sons
ISSN: 0016-8025 (printed)
ISSN: 1365-2478 (electronic)

Acknowledgements

This thesis would not have come to fruition without the help of a great many people. First and foremost I am deeply grateful to my supervisors: Professor Stewart Greenhalgh and Dr. Bing Zhou. I regard myself as privileged to have received your technical guidance, encouragement and patience throughout my studies. I acknowledge the help of Dr Jing-Ping Zhe who provided useful field based training and data sets.

I also wish to thank my fellow postgraduate colleagues at the University of Adelaide, Mark Greenhalgh, Catherine Sinclair, Xu Liu and Peter Moran, for the stimulating discussion, friendship and fond memories. The University of Adelaide Physics Department staff deserve special mention for their valuable support, especially Ramona Adorjan.

I thank the entire ETH Zurich Geophysics group for the remarkable experience gained while studying there. In particular I express gratitude to Alain Plattner, Laurent Marescot, Mark Blome and Joseph Doetsch for making me so welcome and for sharing their wealth of knowledge. I reiterate my sincere appreciation for the positive experiences gained during these times at ETH which were organised by Professor Stewart Greenhalgh.

I am indebted to my family, Allan, Jane, Jon and Jack, for their support, understanding and love. Finally, I thank Tia for her unwavering belief in me.

Chapter 1: Introduction

Exploration geophysics is a well established discipline that seeks to image the Earth's interior by exploiting natural physical field variations (e.g., gravity, magnetic, heat flow, telluric currents, radioactivity) or artificially created ones (seismic, electrical, electromagnetic). It relies on variations in certain physical subsurface properties (e.g., density, magnetic susceptibility, electrical conductivity, dielectric constant, elastic constants) to cause variations in the fields which can then be sensed and the data variations interpreted in terms of subsurface structure and constitution. Geophysics is widely practiced in areas such as oil and gas exploration, mineral search, geotechnical engineering, hydrological investigations and environmental monitoring. This thesis concentrates on the DC electrical resistivity method which is an artificial field method routinely applied for high resolution near surface imaging in connection with environmental, hydrological and engineering investigations as well as mineral exploration. The importance and applicability of the method continues to grow with the ever increasing demands on global natural resources, infrastructure and water supplies.

1.1 Basic Concept and Applications

Electrical and electromagnetic geophysical techniques which use a controlled impressed source field can be broadly categorised according to operating frequency and method of coupling to the ground. Signal frequencies can vary from 0 (DC) to GHz (Radar) and the coupling can be either galvanic (direct contact via electrodes) or inductive (via coils of wire).

The resistivity (or geo-electric) method utilizes a DC power source to get current to flow in the ground between a source electrode and a sink electrode. The pattern of current flow (hence the electric field) depends on the subsurface resistivity distribution. By measuring the variations in electric potential between numerous pairs of receiver electrodes placed on the surface or in boreholes (also galvanically coupled) one can infer the conductivity distribution. The resistivity method is treated comprehensively in many standard textbooks (Kunetz, 1966; Keller and Frischknech, 1966; Ward, 1990; Telford *et al.*, 1992; Reynolds, 2011) and so only the fundamentals will be reviewed here. Figure 1 shows an example of current flow between electrodes A and B and the corresponding equipotential contours for a homogeneous half space. Because the medium is isotropic, the equipotentials are perpendicular to the current flow lines. For heterogeneous media the pattern would be far more complicated. It is now standard practice to convert the collected potential (or voltage) data from mobile receiver electrodes M and N for various current electrode (A and B) positions and spacings into a map of the subsurface resistivity structure. Subsequent to this a geological interpretation of the resultant physical model (resistivity or its inverse, conductivity) is carried out that can be used to infer rock/soil type, degree of weathering, water content, etc.

Figure 1: Current and potential lines in a homogeneous isotropic half-space (after Van Nostrand and Cook, 1966). A and B symbolise current electrodes (sources) with M and N being potential electrodes (receivers).

The method is widely used to delineate and characterise the subsurface across a range of disciplines such as geotechnical engineering (Pettifer *et al.,* 2000), hydrogeology (Doetsch *et al.,* 2010), environmental monitoring (Rucker *et al.,* 2011), archaeological search (Noel and Xu, 1991; Papadopolous *et al.*, 2011), landslide research (Travelletti *et al*., 2011; Cassiani *et al.*, 2009*)* and resource exploration (Bibby *et al.,* 1984). Other disciplines outside of geophysics, such as medical imaging (Brown, 2003) and materials testing (Kupke *et al*., 2001), exploit the same resistivity principle in visualising opaque objects via impedance tomography.

Considerable advances in multi-electrode arrays, automated recording instrumentation, as well as computer hardware and software over the last twenty years have enabled 2D and 3D resistivity investigations (with associated modelling and inversion code) to become commonplace and widely available. Surveys can be carried out quickly and economically using multi-electrode acquisition systems.

1.2 Resistivity of Earth Materials

Current flow in a resistor is governed by the well known Ohm's law:

$$I = U / R \qquad (1)$$

where U is potential difference (Volts), R is resistance (Ohms) and I is current (Amps). Electrical resistance depends on the size and geometry of the sample. In the case of a cylinder of length L and cross sectional area A it is given by:

$$R = \rho L/A \qquad (2)$$

where ρ (Ohm – metre) is the electrical resistivity of the material. Resistivity is a fundamental and intrinsic point property of a material which is a measure of how strongly the material in question impedes the flow of electricity. Resistivity is the reciprocal of conductivity, σ (Siemens per metre), and by rearranging (2) for the cylinder we have:

$$\rho = 1/\sigma = RA/L \quad (3)$$

Several different current conduction mechanisms are possible in typical Earth materials. In very pure metallic minerals, electronic conduction can occur. These materials have very low resistivities ($< 10^{-8}$ Ohm-m) because high mobility electrons are the charge carriers. Semi conduction occurs in igneous rocks and sulphides where the charge carriers are ions (holes). Mobility of ions is temperature dependent and lower than that of electrons. Resistivities for this type of conduction vary from 10^{-3} to 10^{-5} Ohm-m.

Current flow in the subsurface is largely electrolytic in nature. Dissolved salts distributed in pores and fractures enable the movement of charge carriers. The relationship between salt content, saturation, porosity (ϕ) and permeability contributes to the overall resistivity of a medium. Archie (1942) described the resistivity of a completely saturated whole rock (ρ_o) with a pore fluid resistivity of (ρ_w) through an empirical relationship, which was later extended to the more general form which includes partial saturation (not considered here):

$$\frac{\rho_o}{\rho_w} = F = a\phi^{-m} \quad (4)$$

where *F* is the formation factor, *a* is the tortuosity factor (related to pore shape and connectedness) and *m* is the cementation factor. Typical values for the cementation factor are: 1.8 - 2.0 for consolidated sandstones to 1.3 for unconsolidated sands; while the tortuoisty varies between 0.6 - 1. The salinity of the fluid is considered in the ρ_w term.

Texture and sorting also have an influence on resistivity. If there is limited pore space or connectivity such as in unweathered basalt there is also limited means for current conduction. Figure 2 shows textures of some common rock types.

Figure 2: Various textures of commonly encountered rock (after Ward, 1990).

Clay mineral content in rocks can provide an extra conduction pathway via an electrical double layer that forms at clay water interfaces. The double layer forms as a result of the clay minerals absorbing cations and retaining them in an exchangeable state; the clay mineral surface then acts as a separate conducting path in addition to the solution path. Waxman and

Smits (1968) investigated the effects on resistivity due to conduction through the double layer.

To summarise, the main factors that can decrease the electrical resistivity of a medium are:

- additional pore-fluid
- higher salinity fluid
- increased fracturing (weathering) and interconnection between pores
- additional clay content
- increased temperature

Resistivity of earth material increases with:

- greater levels of compaction (where less pathways become available for electric current flow)
- lithification (where pores are blocked by mineral deposition)

The key advantage of the resistivity method is that the electrical properties of the Earth vary over many orders of magnitude. Figure 3 shows a summary of resistivity values for common rocks. Other geophysical properties such as seismic velocity, density, and relative permittivity vary over a much smaller range (Keller and Frischknecht., 1966).

Figure 3: Typical range of electrical resistivities / conductivities of earth materials (after Ward, 1990).

1.3 Field Measurements and Equipment

The electric potential U at an electrode M due to a surface point source of current A situated a distance r_{AM} away in a homogeneous isotropic half space is given by:

$$U_{\mathrm{M}} = \rho I / 2\pi r_{\mathrm{AM}} \tag{5}$$

Taking into account also the potential due to the current sink (B) located a distance r_{BM} away the total potential at M is:

$$U_{\mathrm{M}} = \frac{I\rho}{2\pi}\left[\frac{1}{r_{\mathrm{AM}}} - \frac{1}{r_{\mathrm{BM}}}\right] \tag{6}$$

It is common to measure the potential difference or voltage drop between two receiver electrodes M and N. By the principle of superposition, the potential difference ΔU between M and N would then be:

$$\Delta U_{MN} = \frac{I\rho}{2\pi}\left[\frac{1}{r_{\mathrm{AM}}} - \frac{1}{r_{\mathrm{BM}}} - \frac{1}{r_{\mathrm{NA}}} + \frac{1}{r_{\mathrm{NB}}}\right] = \frac{I\rho}{K} \tag{7}$$

The quantity K is referred to as the geometric factor which describes the electrode configuration geometry. In practice it is common to normalise the potential difference measurements for the effect of the current strength I and the geometric factor K to obtain the apparent resistivity (ρ_a):

$$\rho_a = K\frac{\Delta U}{I} \tag{8}$$

which has the same units as the true resistivity. For a homogeneous Earth the apparent resistivity is equal to the true resistivity. Any departures of the Earth from uniform resistivity and flat topography are revealed by variations in the apparent resistivity with electrode positions. Apparent resistivity data taken in the field for surface measurements are often plotted in the form of a pseudo-section (Loke and Barker, 1996). This involves plotting the raw data values at a horizontal position equal to the array midpoint and at a depth position equal to some fraction of the electrode separation (e.g. for the Wenner array, it is one third of the distance between the current electrodes). Contouring of the pseudosections is a valuable tool used in preliminary interpretation and data quality control (Dahlin, 1996). Buried electrodes used in cross-hole surveys require a more complex consideration of image sources to correctly compute apparent resistivity and do not easily lend themselves to display as a pseudosection (Marescot *et al*., 2006).

The relative simplicity of equipment needed for fieldwork is displayed in Figure 4. Most field techniques use two current electrodes (a source and sink) and two potential electrodes for a single measurement. Low frequency current waveforms are sometimes employed to suppress electrode polarization and self potential effects (Dahlin, 2000). It is possible to place one of each of the current (sink) and potential (reference) electrodes at a large distance from the others to simulate pole-pole measurements. If only one of the current electrodes is located remotely then this gives rise to the pole-dipole array. Standard four-electrode arrays commonly used are: Schlumberger, Wenner, dipole-dipole and the gradient. A comprehensive compilation and discussion of array types can be found in Szalai and Szarka (2008).

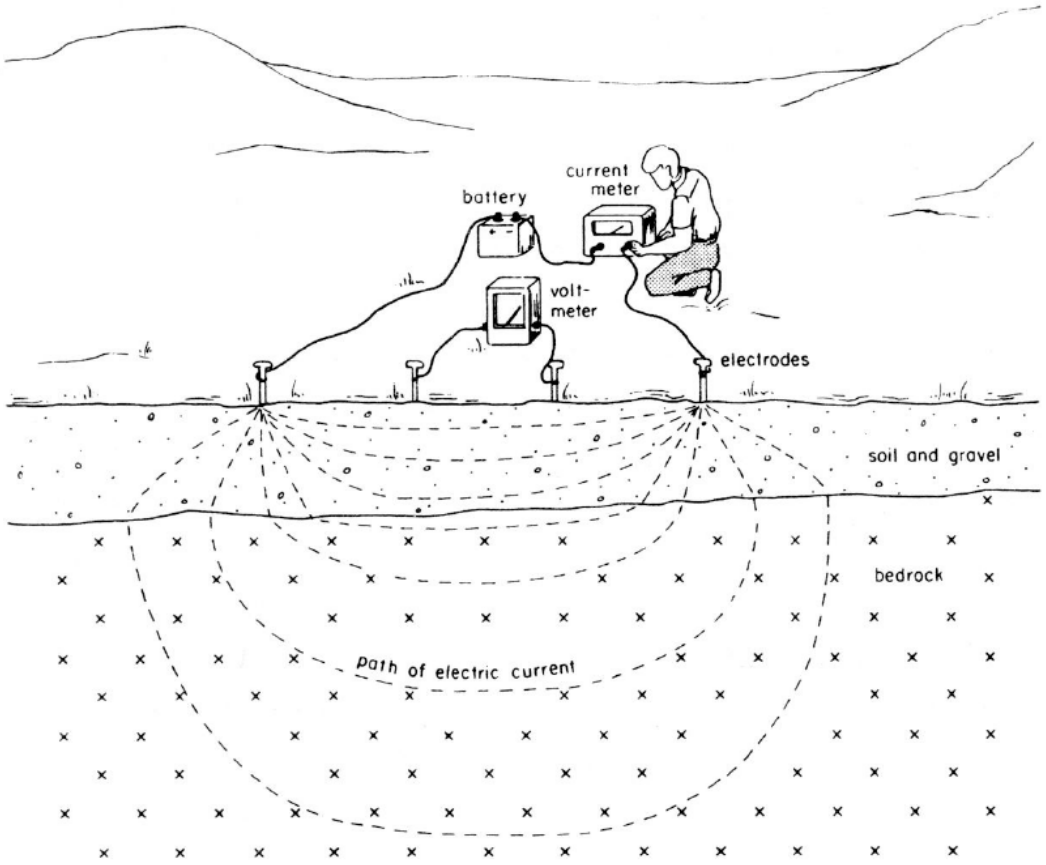

Figure 4: simple four electrode field setup (from Robinson and Coruh, 1988).

Conrad Schlumberger (Schlumberger, 1920) in Europe and Frank Wenner in the USA conducted the original resistivity field experiments (Kunetz, 1966). Since their pioneering efforts, numerous field procedures and improvements and have been introduced, such as:

- vertical electric sounding (Barker, 1981)
- resistivity profiling or traversing (Telford *et al*., 1990)
- 2D and 3D tomography (Loke and Barker, 1996)
- Cross-hole (Zhou and Greenhalgh, 2002), bore-hole to surface tomography

Resistivity sounding seeks to determine the vertical variation of resistivity with depth. It entails keeping the centre of the electrode array fixed (sounding position) and repeating the measurements for varying separations of the electrodes. As a general rule, the depth of current penetration increases with electrode separation (Gish and Rooney, 1925). By contrast, resistivity profiling provides an indication of how resistivity varies in a horizontal direction. This is done by keeping the electrode separations constant while varying the location of the spread. The array is moved along a line or a series of profiles in the form of a map. Depth of penetration remains approximately constant with this method, so it can be used to delineate lateral changes such as faults, dykes, gravel lenses and ore deposits. By combining sounding and profiling techniques it becomes possible to obtain data across a 2D subsurface slice that represents both vertical and horizontal apparent resistivity variations.

Field equipment has greatly advanced since the 1980's. This is due to the development of multi-electrode digital acquisition systems (Barker, 1989; Dahlin, 1989) which were inspired by:

- the intensive fieldwork and prohibitive survey time involved using only 4-electrode arrays for 2D or 3D surveys
- improvements in computer control and automated switching
- the strong trend towards tomographic inversion in other geophysical methods, which prompted the need for large redundant data sets (akin to practices in seismic exploration)

Multi-electrode acquisition systems involve using multi-core cables with much larger numbers of electrodes (up to several hundred) for a survey layout. A central computer (using multiplexed or distributed systems) controls the automatic switching through different combinations of measurements between the electrodes. These early systems have been extended (Stummer, 2002; Blome, 2009; 2011; Wilkinson *et al.*, 2010; Zhe *et al.*, 2007) to systems that record across multiple channels in parallel strategies with real-time data displays.

1.4 Anisotropy

Anisotropy of a physical property of a material refers to the directional dependence of the measurements. In geoelectrics, this means that conductivity and hence the measured voltage (or apparent resistivity) is now a function of the direction of the impressed electric field. Therefore the resistivity of the ground varies not only spatially, but with direction. Current can flow easier in certain directions than others. This preference can be due to the intrinsic crystallographic internal structure of the material or to macroscopic effects such as layering (pseudo-anisotropy). Electrical anisotropy in geophysics and has been recognised for a long time (e.g., Maillet, 1947; Keller and Frischknect, 1966). It is well documented that many rock fabrics (or earth materials) can exhibit anisotropy in other physical properties; for example: magnetic (Owens and Bamford, 1976), seismic (Thomsen, 1986), thermal, and dielectric. The cause of the directional dependence depends greatly on the scale, and as explained above it can be macro or microscopic in nature. Electrical anisotropy is widespread and often encountered in the field.

To mathematically describe an anisotropic Earth, it is not sufficient to treat the resistivity ρ as a simple scalar, but as a second rank tensor $\boldsymbol{\rho}$, which can be written in matrix form as:

$$\boldsymbol{\rho} = \begin{pmatrix} \rho_{xx} & \rho_{xy} & \rho_{xz} \\ \rho_{xy} & \rho_{yy} & \rho_{yz} \\ \rho_{xz} & \rho_{yz} & \rho_{zz} \end{pmatrix} \tag{9a}$$

where indices (x,y,z) signify the Cartesian measurement frame. Chapter 2 gives a complete mathematical description of the anisotropic resistivity tensor and how it may be visualized. Ohm's law for current flow in anisotropic media assumes the form:

$$E_i = \rho_{ij} J_j \qquad j = 1,2,3 \tag{9b}$$

where E is the electric field J is the current density and summation through repeated subscript j is understood.

1.4.1 Micro-anisotropy

Micro-anisotropy describes directional dependence at the particle, mineral or crystal scale. Materials such as shales, slate and clay usually have distinct, intrinsic lineation or platy fabric due to the phillosilicate sheet structure which forms the source of micro–anisotropy. It is not uncommon to encounter anisotropy in sedimentary strata; many solid particles have flat or elongated shapes that settle so that they are oriented parallel to the plane of deposition. This results in a pore structure that allows electric current to flow more easily parallel to the bedding plane than perpendicular to it.

Mendelson and Cohen (1982) and Rey and Jongmans (2007) examined the effect of particulate (or grain) shape on the electrical properties of sedimentary rock, in particular through Archie's law (Archie, 1942). It was found that the presence of highly oblate (disk shaped or anisotropic distribution) grains can raise or lower the cementation factor depending on the alignment of the grains and tortuosity of the current paths. For anisotropic grains the resistivity is described by a tensor with principal values that satisfy a generalized form of the well known Archie's law:

$$\rho_j^o = a_j \phi \rho_j^w \phi^{-m} \qquad (10)$$

whereρ_j^o is the jth principal value of the resistivity tensor and $a_j \phi$ can be expanded as a power series in ϕ(porosity) with a constant leading term.

1.4.2 Macro-anisotropy

Macro-anisotropy is also referred to as structural anisotropy or pseudo-anisotropy and occurs at a macroscopic scale. There are two main groupings:

1) A series of layers or bands of dissimilar isotropic materials behave as a single (bulk), equivalent anisotropic unit. The basis of this type of anisotropy is that the electrode spacing (measurement length) is greater than the thickness of alternating bands of isotropic material. Alternating bands are usually formed in depositional processes such as alternating sand – shale laminae and alternating fine and coarse micro-layering. An example of this type of anisotropy is shown inFigure 5, where alternating layers of sandstone, clay and marl materials are clearly exposed along coastal cliffs around the town of Torquay in Victoria, Australia. This type of macro-anisotropy has been reported in reservoir environments. Klein and Martin (1997) explored the petrophysics of electrically anisotropic reservoirs and found that anisotropy depends greatly on the fluid saturation type.

2) Weathering, fracturing, jointing and cleaving (Skinner and Heinson, 2004) enable conduction along preferential electrical (and hydraulic) flow paths. In most hard rocks, fractures occur in sets with more or less well-defined preferred orientations (Skjernaa and Jorgensen, 1993). An example of this is shown in Figure 6. Anisotropy is often observed in karstic geologies (Hart and Rudman, 1997).

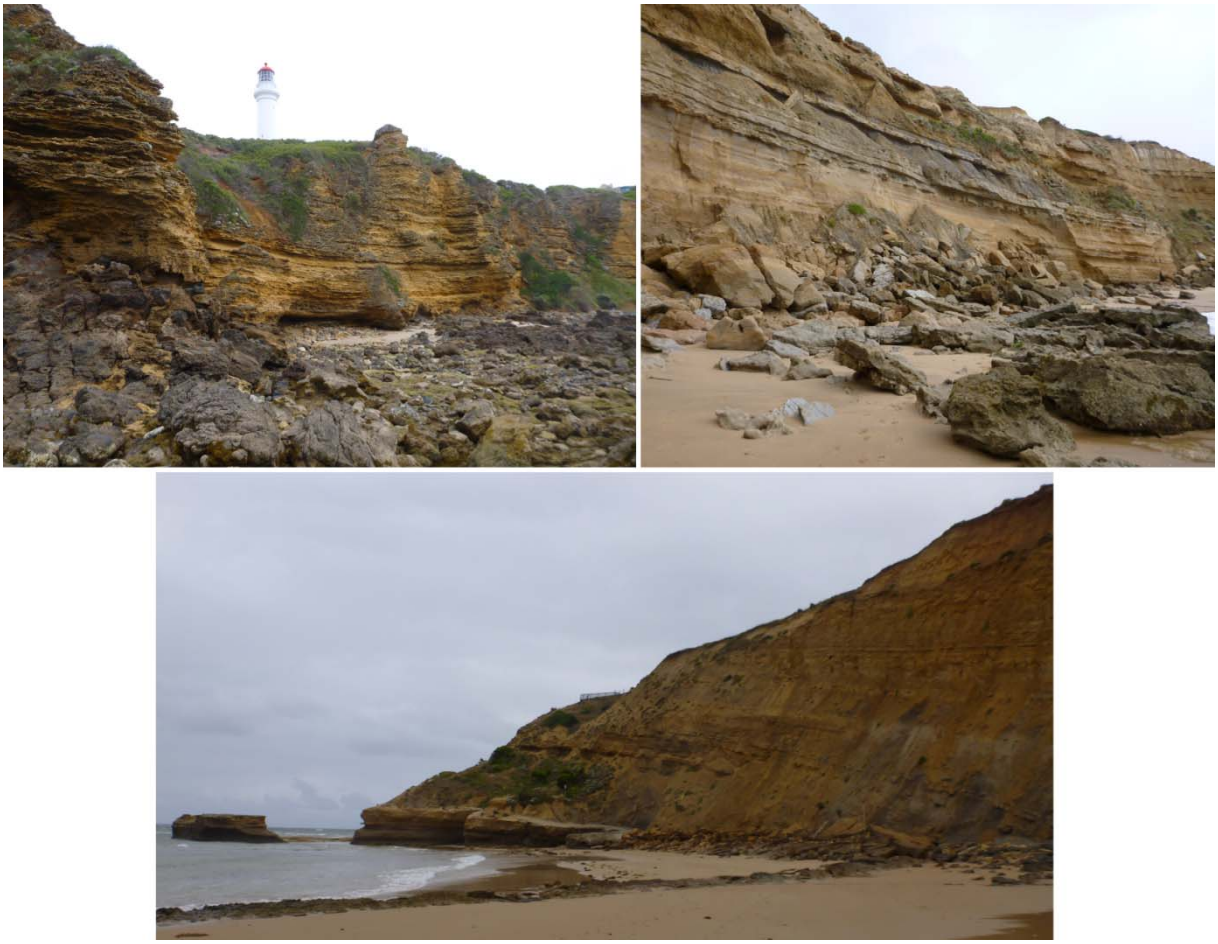

Figure 5: examples of bulk anisotropic media with alternating layers of clay, sandstone and marl material in a sedimentary geology. Photos were taken along the coastline of Torquay, Victoria Australia.

Figure 6: examples of preferential fracture orientations in a rock quarry bench. (Photos care of T. O'Shaunessy, GHD Pty Ltd, Melbourne).

1.4.3 Tilted Transversely Isotropic Media

The widely used tilted transversely isotropic (TTI) model comes from a simplification in which resistivity is constant (isotropic) within a specific plane (i.e., the plane of stratification or fracture plane), but different in all other directions outside that plane. Many geological settings are well described by this simplification. The model is defined by two principal resistivities (longitudinal: ρ_L and transverse: ρ_T) whose directions are orthogonal and an angle θ_0 defining the orientation (axis of symmetry) of the transverse direction.

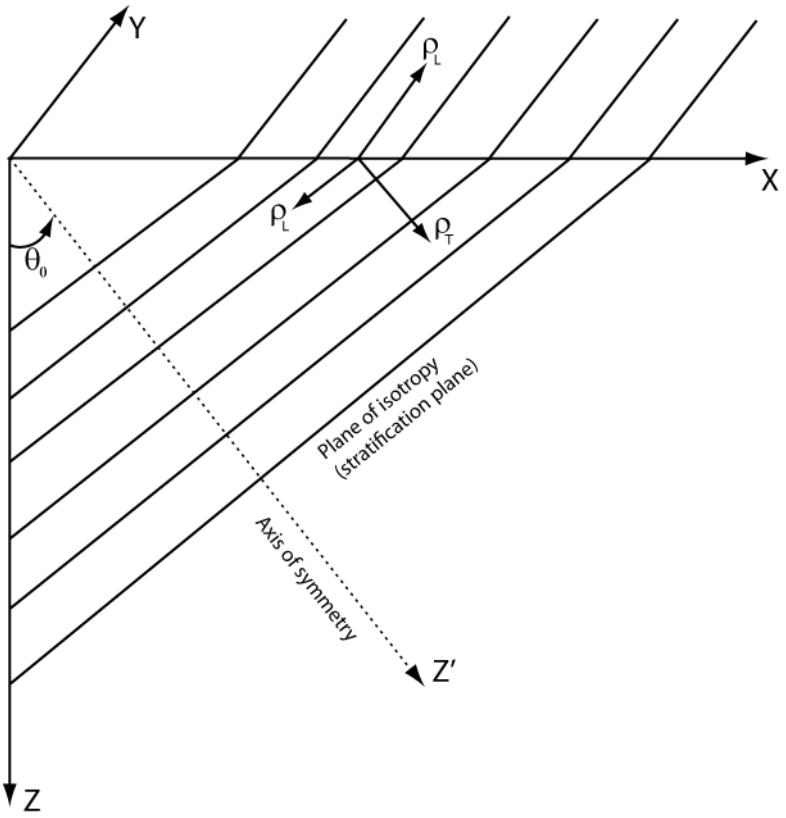

Figure 7: 2D tilted transversely isotropic medium

Resistivity values are generally larger when measured perpendicular to the plane of isotropy (ρ_T) compared to values parallel to the plane (ρ_L). Two important quantities are used to describe TTI media: the average resistivity (geometric mean) ρ_m and the coefficient of anisotropy λ. These two quantities may be expressed in terms of the principal resistivities:

$$\rho_m = \sqrt{\rho_L \rho_T} \tag{11}$$

$$\lambda = \sqrt{\rho_T / \rho_T} \tag{12}$$

Parkhomenko (1967) and Keller and Frishcknecht (1966) provide lists of the coefficients of anisotropy for commonly encountered media. Shale and sandstone interbeds have values in the range of 1.05 – 1.15, while interbedded anhydrite and shale have reported values of 4.0 – 7.5. Even alluvium can have anisotropy coefficients of 1.02 – 1.1. Igneous and metamorphic rocks can also have significant anisotropy (Hill, 1972; Asten, 1974). TTI media are described in detail in Chapter 2.

1.4.4 Principle of Equivalence and the Paradox of Anisotropy

TTI anisotropy in the subsurface can give rise to ambiguous and unexpected measurements of apparent resistivity. Incorrect interpretations arise if isotropy is assumed.

Surface measurements made on a TTI medium having a vertical axis of symmetry (VTI case) such as in horizontally layered sand-shale sequences are invariant, as shown in Figure 8. If such anisotropy exists it is undetectable at the surface. Depth estimates made for this situation will be in error by a factor of λ. This follows from the *Principle of Equivalence*, which states that for surface measurements a single anisotropic layer of thickness h and resistivities ρ_L and ρ_T is indistinguishable from an isotropic layer of thickness λh and resistivity ρ_m (Keller and Frischknecht, 1966). Figure 8 displays an example of equivalence in which surface measurement of apparent resistivity made on an anisotropic VTI medium (left diagram) would result in an identical reading if made on the isotropic medium (right diagram).

It is important to note that a sequence of thin isotropic layers can in reality appear as a single macro-anisotropic layer. The effective longitudinal resistivity of the sequence is obtained by considering it to behave like a parallel resistor network, in which current can distribute itself through the layers and each layer can be replaced by the resistor $R_i = \rho_i . 1/h_i . = \rho_i/h_i = 1/s_i$, where s is conductance (inverse of resistance). The equivalent total resistance is therefore given by:

$$R_{eq} = 1/\sum s_i = \rho_L . l/A = \rho_L . 1/\sum h_i \quad (13)$$

yielding an effective longitudinal resistivity:

$$\rho_L = \sum h_i \,/\sum s_i, \text{ where } s_i = h_i/\rho_i \quad (14)$$

Now consider flow in the transverse direction through the layer stack, which behaves like a series resistor network in which each layer can be replaced by its resistance $R_i = \rho_i l/A = \rho_i h_i = t_i$. The total equivalent resistance is:

$$R_{eq} = \sum t_i = \rho_T . l/A = \rho_T . \sum h_i \quad (15)$$

yielding an effective transverse resistivity:

$$\rho_T = \sum t \,/\sum h_i, \text{ where } t_i = \rho_i h_i \quad (16)$$

For example, a sequence of 20 layers each 2 metres thick, alternating in resistivity from 5 to 100 Ohm – m, has the following effective parameters: ρ_L= 9.52 Ω m; ρ_T= 52.5 Ω m; $\rho_m = \sqrt{\rho_L \rho_T}$ = 22.36 Ω m; $\lambda = \sqrt{\rho_T/\rho_L}$ = 2.35; h = 92.8 m. It follows that errors in interpreted depths can be appreciable; the true depth in this example is 40 metres, while the apparent depth is 92.8 m.

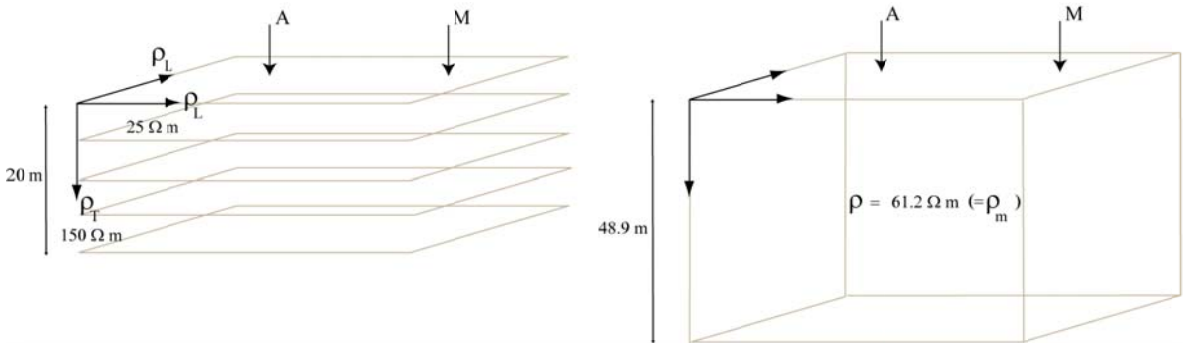

Figure 8: illustration of the principle of equivalence. Measurements made on the surface are indistinguishable between the two cases (anisotropic on the left, isotropic on the right).

Let us now turn to the situation where the axis of symmetry of the TI medium is close to horizontal (the HTI case –see Figure 9b and 9c). Surface measurements made in different directions yield different apparent resistivities ρ_a.One might reasonably expect that measurements of apparent resistivity made parallel to the strike of the more conductive plane (as in Figure 9c) would be lower than measurements made perpendicular to the strike orientation (as in Figure 9b). However, the apparent resistivity measurement is counter intuitive in practice: measurements made parallel to the strike are equal to the mean resistivity ($\rho_a = \rho_m$), while measurements made perpendicular to the strike are equal to the longitudinal resistivity ($\rho_a = \rho_L$), not the transverse resistivity (ρ_T) as one would expect. This is referred to as the *Paradox of Anisotropy* (Maillet, 1947; Keller and Frischknecht, 1966; Bhattacharya and Patra, 1968). The origin of the paradox is the fact that apparent resistivity assumes uniform current density in all directions. Because current density is highest along the strike direction, the apparent resistivity measurement is highest. Likewise the apparent resistivity measurement is lowest when the current density is at a minimum perpendicular to strike.

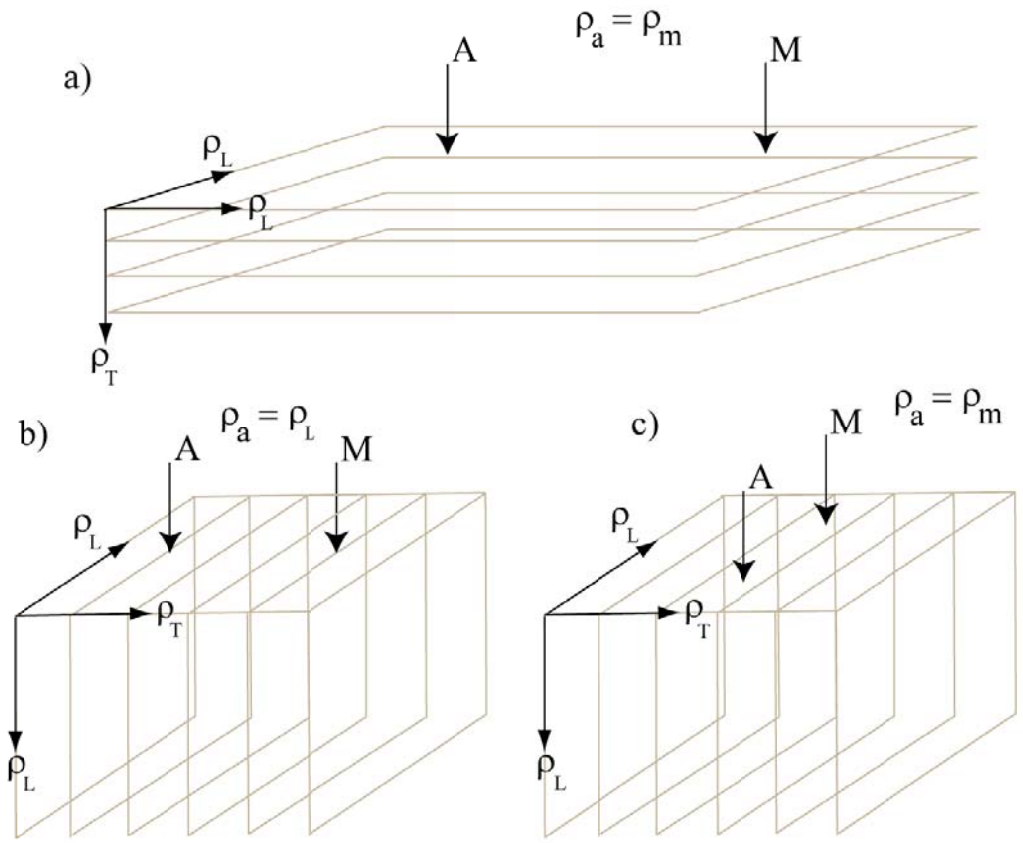

Figure 9: illustration of the Paradox of Anisotropy with measurements for a HTI medium made parallel and perpendicular to the strike of the plane of isotropy.

The Principle of Equivalence and the Paradox of Anisotropy are well illustrated by the example of resistivity measurements made on polar ice (Fujino and Suzuki, 1963). The origin of anisotropy in an ice pack comes from formation processes. Conductive brine is present which freezes in a preferentially vertical orientation (Ingham *et al*., 2008). This results in a near horizontal axis of symmetry of the TI medium. Many attempts at determining sea ice thickness through resistivity soundings have consistently underestimated the ice thickness (Buckley *et al*., 1986; Thyssen *et al*., 1974; Timco, 1979) due to its anisotropic nature. A similar scenario could also be caused by vertical fracturing or steeply dipping beds.

1.4.5 Detecting Anisotropy

The literature regarding the detection of electrical anisotropy can be split into two main categories:

1) Azimuthal resistivity surveys (Taylor and Fleming, 1998; Ritzi and Andolsek, 1992; Busby, 2000).

2) Square array techniques (Habberjam and Watkins, 1967; Habberjam, 1972 and 1975; Matias and Habberjam, 1986, Tsokas *et al*., 1997).

Azimuthal resistivity surveys use a linear array of electrodes to measure apparent resistivity in a variety of directions (e.g., intervals of ten degrees) with a common fixed centre point. Data obtained is usually then presented in a polar co-ordinate plot where in the presence of anisotropy an apparent anisotropy ellipse is observed. Watson and Barker (1999) highlight the problem of differentiating lateral effects and anisotropy from azimuthal surveys and the possibility of misinterpretation. They offer an alternative field technique called the Wenner offset array to differentiate anisotropy, dipping layers and lateral effects.

Square array techniques pioneered by Habberjam and further developed by others involve making three measurements for each survey point (centre of the square): two along the orthogonal sides of the square and one along the diagonal. The square array offers greater sensitivity to anisotropy over standard co-linear arrays. Also fewer electrodes need to be moved per measurement offering higher practicality for the square array over crossed co-linear arrays.

The Principle of Equivalence and the Paradox of Anisotropy that afflict surface measurements have far less effect when the source and receiver electrodes are placed beneath the surface. Anisotropy can be more readily detected using cross-hole and borehole to surface techniques than with simple surface measurements, especially when the axis of symmetry is sub-vertical. The emerging trend is for tensor measurements, in which the impressed electric field (from the current electrodes) is sequentially applied in two orthogonal directions, and the voltage measurements made on two orthogonal sets of potential electrodes.

1.5 Electrical Resistivity Imaging (ERI)

Modern electrical resistivity imaging techniques, also referred to as electrical resistivity tomography (ERT), have followed advances in other geophysical fields such as seismic and potential field methods. ERI utilises geophysical modelling and inversion theory, multi-channel, multi electrode acquisition systems and now widely available data processing software to obtain 2D and 3D tomographic images of the Earth's resistivity distribution.

Modern instruments (Stummer, 2003; Zhe, 2006; Blome, 2009, Wilkinson *et al.*, 2010; Blome *et al.*, 2011) are computer controlled multi-electrode systems capable of switching current electrodes throughout a linear 1D or areal 2D array while making potential measurements in parallel across a number of channels. Massive data sets can be collected efficiently using relatively few electrodes.

1.5.1 Forward Modelling

Once a data set is collected in the field a reconstruction process turns the apparent resistivity data into an image of 2D or 3D bulk (true) resistivity variations. An important part of the reconstruction process is to solve the forward problem which involves deriving a theoretical response (synthetic data) for a suite of input parameters (electrode configurations and the initial or current resistivity distribution) to compare with the observed data. Because the forward modelling must be carried out multiple times for the various model updates, it is crucial to have an accurate and fast solver available. For the resistivity problem this means solving the differential equation that governs the flow of electrical current in the ground, viz., the Poisson equation:

$$\vec{\nabla} \cdot \left(\sigma \vec{\nabla} U\right) = I\delta(\vec{r} - \overrightarrow{r_S}), \qquad \vec{r}, \overrightarrow{r_S} \in \Omega \tag{17}$$

where σ is the conductivity (isotropic or anisotropic, which varies as a function of position), U is the potential, $\overrightarrow{r_S} = (x_s, y_s, z_s)$ is the location of the current electrode in Ω. The governing equation can be solved analytically or approximately using numerical approaches. Analytic solutions may be used for special cases but most often in practical work numerical methods are employed.

Numerical solutions for DC forward modelling include finite difference (Dey and Morrison, 1979), finite element (Zhou and Greenhalgh, 1999), boundary element (Hvozdara and Kaikkonen, 1998), spectral element (Patera, 1984), wavelet theory (Plattner, 2011) and the Gaussian quadrature grid (GQG) method (M. Greenhalgh, 2008).

A number of developments have evolved resistivity modelling into its current state. Computer based interpretation tools started with 1D modelling (Ghosh, 1971) using fast convolution techniques and were extended to 2D methods using finite difference (FD) operators. Problems are encountered with the FD method for electrode singularity and incorporation of arbitrary topography. These difficulties were overcome with the more flexible finite element method (FEM) (Coggon, 1971; Pridmore *et al*., 1981; Zhou and Greenhalgh, 2001; Gunther, 2006). The FEM is able to use complicated meshes to incorporate complex models along with arbitrary topographic features. The introduction of singularity removal (Lowry *et al*., 1989; Blome, 2009) and improved boundary conditions (Zhang *et al*., 1995) have greatly increased numerical accuracy.

Recently, DC resistivity numerical methods have been developed that incorporate anisotropy (Yin and Wiedelt, 1999; Herwanger *et al*., 2004; Pain *et al*., 2003; Li and Spitzer, 2005; Pervago *et al*., 2006; Kim *et al.*, 2006; Zhou *et al*., 2009). This is in addition to a body of literature describing analytic solutions for simple anisotropic models. For example, Bhattacharya and Patra (1968) give an analytic solution for the potential on the surface of a uniform TTI medium. This work has been significantly extended. A thorough review of this literature is given in the introduction to Chapter 2.

1.5.2 Inverse Modelling

Electrical inversion is the practice of reconstructing the resistivity distribution of the subsurface from the collected DC apparent resistivity data. This is a difficult task because: i) the measurement process has associated errors, ii) the inverse problem does not have a unique solution; an infinite number of different resistivity models can provide virtually the same voltage response, iii) there is often more free model parameters than independent data points, making the problem ill-posed. Inversion theory (Tarantola, 1978; Menke, 1989) deals with these challenges by implementation of inversion regularization schemes (constraints, damping, smoothing) and incorporation of data errors by weighting or other means. The levels and type of model parameterization and regularization applied in inversion are subjective and need to be chosen by the user. If too much regularization is applied then the reconstructed model may not reflect the true subsurface, whereas if too little is applied the inversion may become unstable and not converge to a minimum in the data misfit.

Early attempts at resistivity inversion were based on 1D models using sounding data alone. The first 2D tomography attempts were reported by Inman (1975) and Tripp *et al*. (1984). These early works were extended to 3D with an inversion scheme for pole-pole data developed by Park and Van (1991). Non-linear conjugate gradients methods (Ellis and Oldenburg, 1994) and Newton-type schemes (e.g., Li and Oldenburg, 1999) are both commonly used approaches today.

The two key components that are at the heart of almost all inversion schemes are: forward modelling, and sensitivity calculations. The forward solver or operator ($\boldsymbol{F}$) predicts a synthetic data set ($\mathbf{d}^{\mathrm{pred}}$) for a given model parameter vector ($\boldsymbol{m}$):

$$\mathbf{d}^{\mathrm{pred}} = \boldsymbol{F}(\boldsymbol{m}) \tag{18}$$

The resistivity problem is non-linear because the forward operator depends on the model $\boldsymbol{m}$ and cannot be described by a simple matrix-vector multiplication as is possible for some other geophysical methods (i.e. gravity, seismic travel time tomography in low contrast media).

The goal of the inversion process is to find an approximation of the true subsurface model ($\boldsymbol{m}^{est}$) that best fits the set of observed field data ($\mathbf{d}_{\mathrm{obs}}$):

$$\boldsymbol{m}^{\mathrm{est}} = \boldsymbol{F}^{-1}(\mathbf{d}_{\mathrm{obs}}) \tag{19}$$

Usually the problem is solved iteratively by locally linearizing the forward operator around an initial guess for the model vector ($\boldsymbol{m}_0$). Therefore, at each inversion iteration *k*, a new model $\boldsymbol{m}_{k+1} = \boldsymbol{m}_k + \Delta\boldsymbol{m}$ can be calculated based on the previous iteration model parameter vector and the update vector. A Taylor approximation of first order yields:

$$\mathbf{d}^{\mathrm{pred}} = \boldsymbol{F}(\boldsymbol{m}_k + \Delta\boldsymbol{m}) = \boldsymbol{F}(\boldsymbol{m}_k) + \frac{\partial \boldsymbol{F}(\boldsymbol{m}_k)}{\partial \boldsymbol{m}} \Delta\boldsymbol{m} + \ldots \approx \boldsymbol{F}(\boldsymbol{m}_k) + \boldsymbol{J}\Delta\boldsymbol{m} \tag{20}$$

where the Jacobian matrix $\boldsymbol{J}$contains the sensitivities which give the relation between a perturbation in the field measured quantity (voltage or apparent resistivity) in response to a perturbation in the medium properties (true resistivity). It changes with each electrode configuration and subsurface cell. The Fréchet derivatives which form the elements of the $\boldsymbol{J}$ matrix are

$$\boldsymbol{J}_{\mathrm{ij}}(\boldsymbol{m}_{\mathrm{k}}) = \frac{\partial \mathrm{F_i}(\boldsymbol{m}_{\mathrm{k}})}{\partial \boldsymbol{m}_{\mathrm{j}}} \tag{21}$$

The focus of the inversion is to minimise the difference between the measured and predicted data (the residuals):

$$\mathbf{d}_{\text{obs}} - \boldsymbol{F}(\boldsymbol{m}_{\text{k}}) = J\Delta m \tag{22}$$

Hence, the inverse problem now can be formulated as an optimisation (minimisation) problem of an objective function (ϕ) that is usually defined as a combination of data residual ϕ_d and model residual ϕ_m:

$$\min(\phi) = \min(\phi_d + \gamma\phi_m) \tag{23}$$

where γ is the damping factor that determines the trade off between the data fit and the a-priori knowledge. Using an L_p-norm, the data and model residuals can be defined as:

$$\phi_d^p(\boldsymbol{m}) = \sum_{i=1}^{N} \left|\frac{d_i - F_i(\boldsymbol{m})}{\varepsilon_i}\right|^p = \|\boldsymbol{C_D^{-1}}(\mathbf{d}_{\text{obs}} - \boldsymbol{F}(\boldsymbol{m}))\|_p^p \tag{24}$$

$$\phi_m^p(\boldsymbol{m}) = \|\boldsymbol{C_M^{-1}}\boldsymbol{m}\|_p^p \tag{25}$$

where p is the norm factor and $\boldsymbol{C_D^{-1}}$, $\boldsymbol{C_M^{-1}}$ are the inverse data and model covariance matrices, respectively.

The inverse of the data covariance matrix uses the measured or assumed errors in the set of data measurements to apply an importance weight (or reliability factor) to each datum residual. The inverse of the model covariance matrix provides means to eliminate some of the ambiguity of the inversion problem; this is termed regularisation. Commonly employed methods include placing structural constraints on the model parameters (i.e. upper and lower bounds) and penalising spatial variations (roughness) between model parameters, also known as smoothing (Constable *et al.*, 1987).

Choosing the level of damping (γ) applied to an inversion significantly effects the end product as it controls the balance between data fit and a-priori knowledge (inferences from geology, borehole logs etc). Schemes for selection of damping factors (Vogel, 2002; Farquharson and Oldenburg, 2004) have been reported in literature such as the L-curve method (Hansen and O'Leary, 1993) which is based upon the relationship between γ and the misfit functions: ϕ_m^p and ϕ_d^p. The damping factor can be varied during inversion (Kemna, 2000) such as decreasing regularization with iterations to lend greater weight to minimization of the data misfit as the solution converges to the global minimum. Yi *et al.*, (2003) reported an approach named active constraint balancing in which the damping factor is set as a spatial variable for each inversion parameter and solved for explicitly in the inversion process.

The norm factor (p) is often chosen to be 1 (L_1 - norm) for data sets with non-Gaussian noise distributions where large outliers exist; this is termed "robust inversion" (Claerbout and Muir, 1973) because it is more tolerant of spurious data values. Also widely used is the least squares or L_2- norm, in which the data are assumed to have an almost Gaussian noise distribution.

The damped least squares inversion problem at each iteration k can be cast as the following minimization or optimization problem, (Greenhalgh *et al.*, 2006):

$$\min\{\left\|\boldsymbol{C_D^{-1}}(\boldsymbol{F}(\boldsymbol{m_k}) + \boldsymbol{J}\Delta\boldsymbol{m} - \boldsymbol{d_{obs}})\right\|_2^2 + \gamma^2\left\|\boldsymbol{C_M^{-1}}(\boldsymbol{m_k} + \boldsymbol{\Delta m})\right\|_2^2\} \tag{26}$$

Setting the derivative of equation (26) to zero and using a Gauss-Newton scheme (Park and Van, 1991), the final equation required to update the model parameter vector $\boldsymbol{m}_{k+1}$ can be written as:

$$\boldsymbol{m}_{k+1} = \boldsymbol{m}_k + \Delta\boldsymbol{m} = \boldsymbol{m}_k + (\boldsymbol{J}^T\boldsymbol{C}_D^{-1}\boldsymbol{J} + \boldsymbol{\gamma}^2\boldsymbol{C}_M^{-1})^{-1}\boldsymbol{J}^T\boldsymbol{C}_D^{-1}[(\mathbf{d}_{\text{obs}} - \mathbf{d}^{\text{pred}}) + \boldsymbol{J}\boldsymbol{m}_k)] \quad (27)$$

The final inversion product (estimated true resistivity model) is obtained when the misfit between the synthetic (theoretically computed response of the current model) and the real data set converges to a pre-defined acceptable level. There are various criteria for doing this.

It is important to be able to quantify the goodness of the reconstructed inversion image (Menke, 1984). This quantification allows comparison and optimization of different choices of survey layout and is also a key aid in interpretation of results. Friedel (2003) presented an inversion method in which the reconstructed image was supported with estimates of model resolution, model covariance and data importance. Model resolution ($\boldsymbol{R}$) relates the estimated model parameters ($\boldsymbol{m}^{\boldsymbol{est}}$) to the true model parameters ($\boldsymbol{m}^{\boldsymbol{true}}$): $\boldsymbol{m}^{\boldsymbol{est}} \approx \boldsymbol{R}\boldsymbol{m}^{\boldsymbol{true}}$ where $\boldsymbol{R}$ is defined as:

$$\boldsymbol{R} = (\boldsymbol{J}^T\boldsymbol{C}_D^{-1}\boldsymbol{J} + \boldsymbol{C}_M^{-1})^{-1}\boldsymbol{J}^T\boldsymbol{C}_D^{-1}\boldsymbol{J} \quad (28)$$

The diagonal elements of $\boldsymbol{R}$ indicate the resolution of each cell model parameter, with values close to zero indicating poor resolution, whereas values close to one indicate well resolved parameters. Perfect resolution is obtained when $\boldsymbol{R}$ is the identity matrix, because then $\boldsymbol{m}^{\boldsymbol{est}} = \boldsymbol{m}^{\boldsymbol{true}}$, but this is not possible in practice. For most field experiments resolution values are far less than 1 for surface arrays, especially at depth because resolution falls off with distance away from the electrodes. Central to the above formal resolution equation (28) is the Jacobian matrix, which depends not only on the choices of electrode layout and model parameterization, but also on the subsurface model itself. The Jacobian matrix changes during the inversions with the iterative model updates. It is normally the final values of $\boldsymbol{J}$ which are used in equation (28).

Recently, an important area of research has evolved whereby methods have been proposed to optimise the resolution of a survey by selecting electrode configurations that provide maximum sub-surface information. Stummer *et al*. (2004) proposed a sequential design strategy in which high information content electrode configurations were successively added to an initial data set until the desired model resolution was achieved. This initial scheme was improved by Wilkinson *et al*. (2006) who proposed other methods such as comparing the resolution matrix as each new electrode configuration was added to the data set. Loke *et al*. (2010) gives a thorough review of the different methods and also compares their computational demands. Loke *et al*. (2011) explores reducing the computing time required to employ the optimisation techniques by using parallel processors. The above techniques could be applied to 3D problems when massively parallel computing facilities are available; however, this is outside the resources of the average practitioner. Blome *et al.,* (2011) made use of parallel recording strategies to record complete data sets as proposed by Xu and Noel (1993) and Lehman (1995). It was then shown that comprehensive data sets could be reconstructed from the linearly independent complete data sets to greatly improve resolution and inversion image results. It was found that in the presence of noise, pole-bipole reconstructed data sets outperformed four point reconstructions due to propagation of errors. Reconstructing comprehensive data sets from the complete data set is akin to a conditioning of the Hessian matrix.

1.6 Anisotropic Resistivity Inversion

The literature on anisotropic resistivity inversion is sparse due to: i) the added complexity and increased number of model parameters in the forward solver for tensor anisotropic resistivity; ii) the lack of knowledge/literature investigating the relationship between measurement sensitivity and the various anisotropic parameters; iii) the equivalence principle, which states that for particular types of anisotropy, surface measurements will produce ambiguous results; iv) difficulty as to how to regularise the anisotropy in the inversion scheme.

LaBreque *et al.,* (2004) incorporated anisotropy into the finite difference modelling formulation of Dey and Morrison (1979), but assumed that the axes of the conductivity ellipsoid were aligned with the co-ordinate directions, greatly simplifying the problem. They used an Occam-style inversion scheme with an objective function including regularisation operators to control smoothness and level of anisotropy permitted. Pain *et al.,* (2003) used a Levenberg-Marquardt type iterative preconditioned conjugate gradient inverse solver and a finite element forward solver. Their major contribution was to formulate and incorporate penalty functions for anisotropy and subsurface structure within the inversion objective function. Simple synthetic models with pole-pole array data sets were used to validate the inversion routine and highlight the non-linear nature of the problem. Suites of inversions were run to select the optimal penalty functions to minimise data residuals. Herwanger *et al.,* (2004) extended the analysis by presenting a case study in which cross-hole resistivity and seismic methods were used to independently recover anisotropic model parameters. A good agreement of spatial structures with high anisotropy was found between the two techniques. Kim *et al.,* (2006) presented a case study in which cross-hole tomography was able to delineate subsurface cavities having isotropic properties and situated in a highly anisotropic biotite-gneiss background. The orientations of the anisotropy axes were assumed to be in-line with the measurement (Cartesian) frame, an often questionable assumption. Anisotropy penalty terms were added to the objective function along with spatially varying Lagrange multipliers which increased the stability and resolution in the inversion process. Unfortunately, precise details on the forward and sensitivity calculations are not provided for this case study. Yi *et al*., (2011) extend the 2D cross-hole anisotropic tomography work of Kim *et al*., (2006) to 3D tomography. A case study is presented investigating the safety of an apartment block built over an abandoned mine site using field data collected between a number of boreholes. Average resistivity and anisotropy parameter are defined akin to Herwanger *et al.,* (2004). These are displayed in image form and constitute the basis for interpretation.

1.7 Thesis Aims and the Link between Publications

The principal motivation for this thesis project was the importance of electrical anisotropy in resistivity surveying yet the paucity of literature dealing with the topic. The assumption of isotropy is almost always employed in practice. This research work seeks to provide improvements in understanding the influences of electrical anisotropy on resistivity interpretations.

Timely factors which encouraged the study include the data acquisition capabilities of modern resistivity recording systems which allow vast amounts of data to be captured efficiently in the field, and the power of modern computers having multiple processors which allow large data sets to be inverted in reasonable amounts of time.

Each chapter concentrates on different aspects of the underlying theme of electrical anisotropy within a geophysical context. The thesis is theoretical in nature and approaches each of the key aspects that form a standard geophysical inversion scheme. Chapter 2 presents a comprehensive introduction and mathematical description of anisotropic resistivity. It explains the simplifications and assumptions involved in dealing with a TTI medium. Having presented this basis, analytic formulae for electric potential, current density and Fréchet derivatives at any interior point within a 3D TTI homogeneous medium are derived. This set of formulae provides an excellent way to check the accuracy of numerical code, aid in real-time numerical design and provide fast initial model inversion of resistivity data. Chapter 3 presents explicit expressions for the Fréchet derivatives or sensitivity functions in resistivity imaging of a heterogeneous and fully anisotropic earth. Such formulations along with forward modelling capability form the basis for almost all modern inversion schemes. Chapter 4 provides an in-depth look at the effect of varying the strength and orientation of anisotropy on the sensitivity functions, and what the sensitivities look like for the different anisotropic resistivity parameters. Sensitivity patterns for various electrode arrays are also evaluated. Chapter 5 provides a comparison between the sensitivities for anisotropic and isotropic media, using the geometric mean of the longitudinal and transverse resistivities (equivalent isotropic parameter) as a basis for comparison. Alternative descriptions (i.e. parameters) for TTI media are given and used to enable comparison. In chapter 6 the thesis culminates in a series of anisotropic resistivity inversion experiments. The inversion strategy is based upon sensitivity formulations from the previous chapters. Synthetic inversion experiments for various electrode configurations and 2D anisotropic models are performed. Image reconstructions obtained using the correct anisotropic inversion code and those obtained using the false isotropic assumption (widely used in practice) are examined and compared.

Four of the thesis chapters have been published in international journals; the fifth has been accepted for publication subject to certain revisions which have now been undertaken. As such, the chapters are self contained with an appropriate literature review that frames its position in the current field of knowledge.

Chapter 2: Electric Potential and Fréchet Derivatives for a Uniform Anisotropic Medium with a Tilted Axis of Symmetry

[1,2]Greenhalgh S.A., [2]Marescot L., [1]Zhou B., [1]Greenhalgh M., [1]Wiese T.C.

1. Department of Physics, University of Adelaide, Australia
2. Institute of Geophysics, ETH Zürich, Switzerland

Pure and Applied Geophysics, 166; 673 - 699

2.1 Statement of Contribution

Electric Potential and Fréchet Derivatives for a Uniform Anisotropic Medium with a Tilted Axis of Symmetry. Pure and Applied Geophysics, 166; 673 - 699

Conceptualization

This work came to fruition after literature reviews performed by T. Wiese and M. Greenhalgh in the field of resistivity investigations in anisotropic media. All authors were responsible for this paper's conceptualization after identifying the gap in the literature.

Realization

S. Greenhalgh was responsible for the original formulation of the solution which was extended by L. Marescot, B. Zhou and T. Wiese. All authors checked the validity of the formulations and offered additions and suggestions. Cheifly T. Wiese was responsible for coding the formulation and testing the code against numerical solutions. M. Greenhalgh and L. Marescot provided valuable additions to the numerical solutions. A variety of different model parameters were tested and analysed by T. Wiese.

Documentation

All authors had significant input on the documentation. S. Greenhalgh wrote the majority of the first draft, with help and additions from all authors, especially L. Marescot. T. Wiese was responsible for figure development and presentation.

The authors hereby certify that the statement of contribution is accurate and give permission for the inclusion of the paper in the thesis:

Greenhalgh S.A., Marescot L., Zhou B., Greenhalgh M. & Wiese T.C., (2009). Electric potential and Fréchet derivatives for a uniform anisotropic medium with a tilted axis of symmetry.
Pure and Applied Geophysics, v. 166 (4), pp. 673 - 699.

Chapter 3: Explicit Expressions for the Fréchet Derivatives in 3D Anisotropic Resistivity Inversion

[1,2]Greenhalgh S.A., [1]Zhou B., [1]Greenhalgh M., [2]Marescot L., [1]Wiese T.C.

1. Department of Physics, University of Adelaide, Australia
2. Institute of Geophysics, ETH Zürich, Switzerland

Geophysics, 74; 673 - 699

3.1 Statement of Contribution

Explicit Expressions for the Fréchet Derivatives in 3D Anisotropic Resistivity Inversion. Geophysics, 74; 673 - 699

Conceptualization

This paper was jointly conceptualized by S. Greenhalgh, M. Greenhalgh, B. Zhou and T. Wiese.

Realization

The basis of the paper was a much earlier formulation for isotropic media derived and published by B. Zhou and S. Greenhalgh. This was extended by M. Greenhalgh and S. Greenhalgh, with significant input from B. Zhou, T. Wiese and L. Marescot. T. Wiese was responsible for coding the numerical formulation and testing its validity over a number of anisotropic models.

Documentation

The bulk of the paper was written by S. Greenhalgh, with large contributions from M. Greenhalgh, L. Marescot, B. Zhou and T. Wiese. All authors reviewed the formulation and the accompanying discussion. T. Wiese developed and presented the figures.

The authors hereby certify that the statement of contribution is accurate and give permission for the inclusion of the paper in the thesis:

GEOPHYSICS, VOL. 74, NO. 3 (MAY-JUNE 2009); P. F31–F43, 10 FIGS.
10.1190/1.3111114

Explicit expressions for the Fréchet derivatives in 3D anisotropic resistivity inversion

S. A. Greenhalgh[1], B. Zhou[2], M. Greenhalgh[2], L. Marescot[3], and T. Wiese[2]

ABSTRACT

We have developed explicit expressions for the Fréchet derivatives or sensitivity functions in resistivity imaging of a heterogeneous and fully anisotropic earth. The formulation involves the Green's functions and their gradients, and it is developed from a formal perturbation analysis and by means of a numerical (finite-element) method. A critical factor in the equations is the derivative of the electrical conductivity tensor with respect to the principal conductivity values and the angles defining the axes of symmetry. The Fréchet derivative expressions were derived for the 2.5D and 3D problems using constant-point and constant-block model parameterizations. Special cases such as an isotropic earth and tilted transversely isotropic (TTI) media emerge from the general solutions. Numerical examples were investigated for various sensitivities as functions of dip angle and strike of the plane of stratification in uniform TTI media.

INTRODUCTION

The inversion of electrical resistivity data to reconstruct the conductivity distribution of the subsurface requires knowledge of the Fréchet derivatives, which form the elements of the Jacobian matrix of the objective function (Menke, 1989; Lesur et al., 1999). These derivatives provide the perturbation in the field quantity (i.e., electric potential or apparent resistivity) for a given perturbation in a medium's properties (i.e., conductivity). They vary spatially throughout a medium and must be computed at each subsurface point for each electrode configuration. The Fréchet derivatives depend upon the conductivity and the survey geometry (i.e., electrode positions). They may be viewed as sensitivity functions of the data, indicating sensitivity variations with various surveying configurations. Thus, they are extremely important in optimizing experiment design and understanding resolution (Stummer et al., 2004; Maurer and Friedel, 2006).

There are various ways to compute the Fréchet derivatives in resistivity imaging. McGillivray and Oldenburg (1990) make a comparative theoretical study of several methods. Park and Van (1991) derive an implicit expression for the Fréchet derivative in the 3D problem. Smith and Vozoff (1984) and Sasaki (1994) calculate the Fréchet derivative by solving the differential equations of the finite-difference or finite-element system. Loke and Barker (1995, 1996) compute the Fréchet derivatives with a homogeneous half-space starting model and Broyden's (1965) updating procedure. Spitzer (1998) describes four methods and presents plots of the sensitivity patterns for homogeneous and simple inhomogeneous models, using common surface and crosshole electrode configurations (pole-pole, pole-dipole, etc.).

Zhou and Greenhalgh (1999) show that the most direct and effective way to compute the Fréchet derivatives is in terms of the Green's functions. They develop explicit expressions and a numerical calculation scheme for the Fréchet and second derivatives for a heterogeneous, isotropic earth using a finite-element approach. Their 2.5D and 3D formulations are for the electric potential and apparent resistivity using any electrode array. Only recently have accurate and efficient computational schemes been developed for calculating the Green's functions in an anisotropic, inhomogeneous earth (Li and Spitzer, 2005; Zhou et al., 2009).

In this paper, we extend the earlier analysis to the case of a general anisotropic, inhomogeneous medium. To the best of our knowledge, such expressions have not been given before. Anisotropy is becoming increasingly important in resistivity imaging (Pain et al., 2003; Herwanger et al., 2004), especially in areas of prominent layering, stratification, fracturing, cleavage, or other rock foliation. Anisotropy can be on a macroscopic or microscopic scale (Bhattacharya and

Manuscript received by the Editor 9 May 2008; revised manuscript received 10 September 2008; published online 10 April 2009.
[1]University of Adelaide, Department of Physics, Adelaide, Australia, and ETH-Zürich, Institute of Geophysics, Zürich, Switzerland. E-mail: stewart.greenhalgh@adelaide.edu.au, gstewart@aug.ig.erdw.ethg.ch.
[2]University of Adelaide, Department of Physics, Adelaide Australia. E-mail: bing.zhou@adelaide.edu.au; mark.greenhalgh@adelaide.edu.au; timothy.wiese@adelaide.edu.au.
[3]ETH-Swiss Federal Institute of Technology, Institute of Geophysics, Zürich, Switzerland. E-mail: laurent@aug.ig.erdw.ethz.ch.

Patra, 1968; Keller and Frishknecht, 1970). Failure to incorporate anisotropy, where it exists, into modeling and inversion can lead to large errors in resistivity interpretation (Keller and Frischknecht, 1970; Asten, 1974).

ELECTRIC POTENTIAL AND THE CONDUCTIVITY TENSOR

The governing equation for the electric potential $U(\mathbf{r})$ from a point source in 3D anisotropic, inhomogeneous media may be written as

$$D(\boldsymbol{\sigma})U = -I\delta(\mathbf{r} - \mathbf{r}_s), \quad \mathbf{r}_s \in \boldsymbol{\Omega}, \tag{1}$$

where the vector $\boldsymbol{\sigma}$ represents the model parameters consisting of the various components of the conductivity tensor at each spatial point and I is the strength of the point current source located at position vector $\mathbf{r} = \mathbf{r}_s$. The differential operator $D(\boldsymbol{\sigma})$ acting on the potential is defined by

$$D(\boldsymbol{\sigma})U = \frac{\partial}{\partial x_i}\left(\sigma_{ij}\frac{\partial U}{\partial x_j}\right). \tag{2}$$

In vector/matrix form, this is written as

$$\nabla \cdot (\boldsymbol{\sigma}\,\nabla U) = -I\delta(\mathbf{r} - \mathbf{r}_s), \tag{3}$$

where a matrix multiplication is involved inside the divergence operator between the conductivity matrix $\boldsymbol{\sigma}$ and the electric field vector $\mathbf{E} = -\nabla U$. In fact, equation 3 is the equation of continuity for current density, $\nabla \cdot \mathbf{J} = -(\partial\rho/\partial t) = -I$.

For a general anisotropic medium, there are up to six independent components of the symmetric electric conductivity tensor (Onsager, 1931). Writing it out as a 3×3 symmetric matrix in the geographic recording frame (x, y, z), we have

$$\boldsymbol{\sigma} = \sigma_{ij} = \begin{bmatrix} \sigma_{xx} & \sigma_{xy} & \sigma_{xz} \\ \sigma_{xy} & \sigma_{yy} & \sigma_{yz} \\ \sigma_{xz} & \sigma_{yz} & \sigma_{zz} \end{bmatrix}. \tag{4}$$

By means of an eigendecomposition, this matrix can be diagonalized to yield the principal values or eigenvalues $(\sigma_1, \sigma_2, \sigma_3) = (\sigma_{x'x'}, \sigma_{y'y'}, \sigma_{z'z'})$, which denote values of conductivity along the axes of the rotated coordinate frame (x', y', z'):

$$\hat{\boldsymbol{\sigma}} = \begin{pmatrix} \sigma_1 & 0 & 0 \\ 0 & \sigma_2 & 0 \\ 0 & 0 & \sigma_3 \end{pmatrix} = \begin{pmatrix} \sigma_{x'x'} & 0 & 0 \\ 0 & \sigma_{y'y'} & 0 \\ 0 & 0 & \sigma_{z'z'} \end{pmatrix}. \tag{5}$$

These axes (or eigenvectors) are the three axes of the conductivity ellipsoid and represent the natural rock frame referred to above. The semiaxis lengths are equal to the inverse square roots of the principal conductivities. In these principal directions, the vectors $\mathbf{E}$ and $\mathbf{J}$ are parallel, but for all other directions, this is not true. So for an anisotropic medium, the current direction is not perpendicular to the equipotential contours.

Let the unit (eigen) vectors be $\mathbf{e}_{x'}, \mathbf{e}_{y'}, \mathbf{e}_{z'}$. Defining the rotation matrix as

$$\mathbf{R} = \begin{pmatrix} \mathbf{e}_{x'} \\ \mathbf{e}_{y'} \\ \mathbf{e}_{z'} \end{pmatrix}, \tag{6}$$

we can compute the conductivity matrix in the geographic frame as the product of three matrices:

$$\boldsymbol{\sigma} = \mathbf{R}^{\mathrm{T}}\hat{\boldsymbol{\sigma}}\mathbf{R}. \tag{7}$$

This takes us from the natural rock frame to the recording frame.

All eigenvectors are orthogonal; so in addition to the three eigenvalues, there are just three angles that define the tensor and constitute an alternative set of six parameters to the six independent Cartesian components given by equation 4. Pain et al. (2003) work with the Eulerian angles φ, λ, ψ, which permit a rotation around the axes to align the natural frame with the geographic recording frame (see Goldstein [1959, p. 107–109] for a clear picture and explanation of the rotations and transformation matrices). The first rotation ϕ is about the vertical (z-) axis to align the new x-axis (called ξ') with the geologic strike. The second rotation by an amount λ is about the ξ' axis to correspond with the dip and brings the original z-axis into new position z'. The final rotation is about the z'-axis by the slant angle ψ to bring the new x- and y-axes (call them x' and y') into alignment with the principal directions in the plane perpendicular to the symmetry axis z'.

Let the unit vector of this symmetry axis be $\mathbf{e}_{z'} = \hat{\mathbf{z}}'$ direction (with the subscript 3 referring to the above principal values; see equation 5). It is defined by the spherical coordinate orientation angles ($\phi_0 = 90 + \varphi$, $\theta_0 = \lambda$), as shown in Figure 1a. This direction (longest axis of the conductivity ellipsoid) corresponds to the direction of minimum conductivity σ_3 (or maximum resistivity $\rho_3 = 1/\sigma_3$). The other two unit vectors, $\mathbf{e}_{x'}$ and $\mathbf{e}_{y'}$, for which we denote the principal conductivities by subscripts 1 and 2 (σ_1, σ_2), lie in a plane perpendicular to $\hat{\mathbf{z}}'$ (denoted by subscript 3). The $\hat{\mathbf{z}}'$-axis would, for example, be the normal to a prominent bedding or fracture plane having strike $\beta = \phi_0 \pm 90$ and dip measured from the horizontal of $\alpha = \theta_0$ (see Figure 1b). We have from simple trigonometry (see Figure 1a)

$$\mathbf{e}_{z'} = (\sin\theta_0 \cos\varphi_0, \sin\theta_0 \sin\varphi_0, \cos\theta_0). \tag{8}$$

If we now assume that eigenvector $\mathbf{e}_{x'}$ has the same azimuth as the principal axis $\mathbf{e}_{z'}$, then we can determine it by adding 90° to θ_0. The third eigenvector, $\mathbf{e}_{y'}$, is given by the cross product $\mathbf{e}_{z'} \times \mathbf{e}_{x'}$. For the more general situation referred to above, we need a third Eulerian angle ψ (or, say, the azimuth swing ε of $\mathbf{e}_{x'}$) to fix all directions in space (see Figure 1a).

Returning to the situation in which $\mathbf{e}_{z'}$ and $\mathbf{e}_{x'}$ share the same azimuth ($\theta_0 = \varepsilon$), we have

$$\mathbf{e}_{x'} = (\cos\theta_0 \cos\varphi_0, \cos\theta_0 \sin\varphi_0, -\sin\theta_0),$$

$$\mathbf{e}_{y'} = (-\sin\varphi_0, \cos\varphi_0, 0). \tag{9}$$

This reduces the number of independent components of the 3×3 conductivity matrix from six to five (three eigenvalues or principal values and just two polar angles). The justification for reducing the number of parameters by one is that it is very difficult in practice to specify the directions of the two principal axes in the plane perpendicular to z'. The dominant plane itself, which may be a fracture plane or bedding plane, could have an overprinted lineation (e.g.,

cleating or cleavage) or arbitrary orientation producing the three natural rock axes. But nearly all of the treatments in the literature on electrical anisotropy take the plane orthogonal to z' to be a plane of isotropy (i.e., the tilted transversely isotropic or TTI situation) with equal eigenvalues (principal conductivities) in this plane. The third angle is therefore often unimportant. Even in the most general anisotropic analysis (e.g., Pain et al., 2003), the treatment quickly reverts to the transversely isotropic (TI) case.

Preserving for the moment all three distinct eigenvalues but just two angles for the dominant axis of symmetry, the conductivity tensor $\boldsymbol{\sigma}$ in the 3D case now has components (by substituting equations 8 and 9 into equation 7):

$$\begin{pmatrix} \sigma_{xx} \\ \sigma_{xy} \\ \sigma_{xz} \\ \sigma_{yy} \\ \sigma_{yz} \\ \sigma_{zz} \end{pmatrix} = \begin{pmatrix} \sigma_1 \cos^2\theta_0 \cos^2\varphi_0 + \sigma_2 \sin^2\varphi_0 + \sigma_3 \sin^2\theta_0 \cos^2\varphi_0 \\ 0.5(\sigma_1 \cos^2\theta_0 \sin 2\varphi_0 - \sigma_2 \sin 2\varphi_0 + \sigma_3 \sin^2\theta_0 \sin 2\varphi_0) \\ 0.5(-\sigma_1 + \sigma_3)\cos\varphi_0 \sin 2\theta_0 \\ \sigma_1 \cos^2\theta_0 \sin^2\varphi_0 + \sigma_2 \cos^2\varphi_0 + \sigma_3 \sin^2\theta_0 \sin^2\varphi_0 \\ 0.5(-\sigma_1 + \sigma_3)\sin\varphi_0 \sin 2\theta_0 \\ \sigma_1 \sin^2\theta_0 + \sigma_3 \cos^2\theta_0 \end{pmatrix}. \quad (10)$$

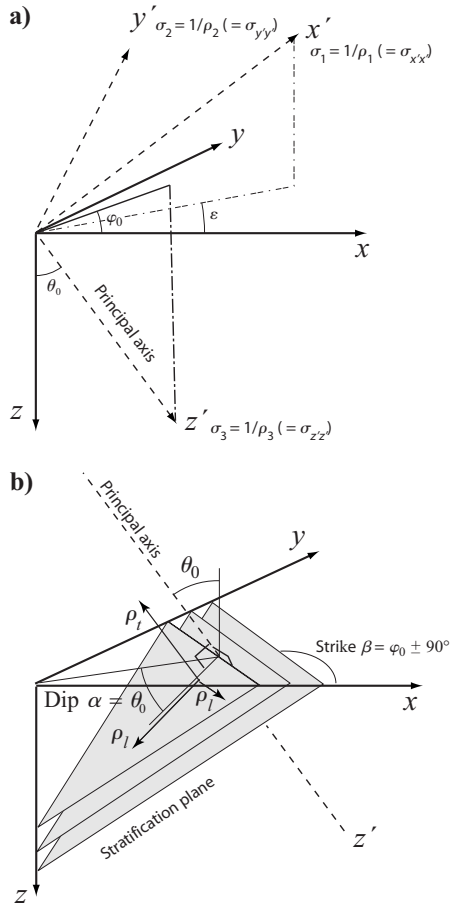

Figure 1. (a) Geographic recording frame (x , y , z) and the rotated or natural rock frame (x' , y' , z') that defines the principal conductivity directions. The symmetry axis is in the z'-direction (or σ_3-direction), specified by polar angles ϕ_0 , θ_0. This is the minimum conductivity (maximum resistivity) direction. If the azimuth of the x'-axis ε is equal to that of the z' axis ϕ_0, then the number of independent components of the conductivity tensor reduces from six to five [three principal values (σ_1 , σ_2 , σ_3) and two polar angles (ϕ_0 , θ_0)]. (b) Special case of TTI media showing plane of stratification (foliation) having strike $\beta = \varphi_0 \pm 90°$ and dip from horizontal $\alpha = \theta_0$. The longitudinal conductivity in the plane of stratification is σ_l, and the transverse conductivity in the direction of the symmetry axis (normal to the plane of stratification) is σ_t. The longitudinal and transverse resistivities are $\rho_l = 1/\sigma_l$ and $\rho_t = 1/\sigma_t$.

The term 2.5D modeling refers to a situation in which medium properties vary in only two dimensions (x-z) but the source is still a point source. The field (electric potential) therefore depends on all three coordinates (x , y , z). This differs from 2D modeling, in which the model and potential are only functions of the coordinates x and z. In 2D modeling, it is implicit that the source be a line source, extended to infinity in the strike (y-) direction.

It is common in 2.5D isotropic modeling to work with Fourier-transformed potentials by transforming with respect to the y-direction, the direction in which the model does not change. This is done for a variety of wavenumber values, and for each wavenumber we solve a 2D problem. The spatial-domain solution is obtained by inverse transforming with respect to wavenumber. The potential is an even function with respect to the y-axis; therefore, a Fourier cosine transform and inverse Fourier cosine transform are used. In the anisotropic situation, the potential is no longer symmetric about the central x-z-plane (along the y-axis) when the azimuth of the axis of symmetry is not 0°. In such situations, the advantages of solving a 2.5D as opposed to a full 3D problem are lost. Furthermore, unless the y-axis coincides with the natural rock axis y', the process of taking the Fourier transform of the original Poisson equation is messy and introduces multiple cross terms in the dyadic product:

$$\nabla^{2D} \cdot (\boldsymbol{\sigma} \nabla^{2D} \tilde{U}) - k_y^2 \sigma_{yy} \tilde{U} + ik_y \left\{ \tilde{U} \left(\frac{\partial \sigma_{xy}}{\partial x} + \frac{\partial \sigma_{yz}}{\partial z} \right) + 2\sigma_{xy} \frac{\partial \tilde{U}}{\partial x} + 2\sigma_{yz} \frac{\partial \tilde{U}}{\partial z} \right\} = -\frac{I}{2} \cdot \delta(r - r_s). \quad (11a)$$

Here, the tilde over U implies the Fourier-transformed potential, k_y is the wavenumber (or transform variable), $\boldsymbol{\sigma}(x , z)$ is the conductivity tensor, and the gradient operator with the superscript 2D implies only the x- and z-components are to be taken.

Therefore, we only advocate 2.5D modeling in the special case when one of the principal axes of the conductivity ellipsoid is in the strike or $y = y\prime$ direction. Under these circumstances, $\sigma_{xy} = \sigma_{yz} = 0$ in equation 11a, so performing a spatial cosine Fourier transform of equation 1 with respect to the y-coordinate yields the simple 2.5D Helmholtz equation:

$$\nabla \cdot (\boldsymbol{\sigma} \nabla \tilde{U}) - \sigma_2 k_y^2 \tilde{U} = -\frac{I}{2}\delta(x - x_s)\delta(z - z_s). \quad (11b)$$

We set $\sigma_2 = \sigma_{yy}$ as the principal conductivity (or eigenvalue of the matrix) corresponding to a symmetry axis in the y-direction. The only other nonzero values of the conductivity tensor $\boldsymbol{\sigma}$ (matrix) that appear on the left side of equation 11a and 11b and that multiply with $\nabla \tilde{U}$ are

$$\begin{aligned} \sigma_{xx} &= \sigma_1 \cos^2\theta_0 + \sigma_3 \sin^2\theta_0, \\ \sigma_{zz} &= \sigma_1 \sin^2\theta_0 + \sigma_3 \cos^2\theta_0, \\ \sigma_{xz} &= \sigma_{zx} = (\sigma_3 - \sigma_1)\sin\theta_0 \cos\theta_0. \end{aligned} \quad (12)$$

These values are obtained by letting $\phi_0 = 0$ in equation 10.

The remaining two eigenvalues σ_1 and σ_3 are the principal conductivity values corresponding to the two principal directions in the x–z-plane, and θ_0 is the angle that the principal direction (eigenvector $\mathbf{e}_{z'}$) makes with the z-axis. If σ_1 corresponds to the longitudinal conductivity σ_l and σ_3 corresponds to the transverse conductivity σ_t, then $\sigma_2 (= \sigma_1)$ will also be a longitudinal conductivity and the coefficient of anisotropy defined by $\lambda = \sqrt{\sigma_l/\sigma_t} \geq 1$.

For the 3D TTI case shown in Figure 1b, a model of considerable geologic importance, just four parameters describe the anisotropy: the longitudinal and transverse resistivities ρ_l and ρ_t, respectively, and the strike β and dip α of the plane of stratification/foliation. For any direction within this plane, the conductivity is constant ($\sigma = \sigma_l = 1/\rho_l$).

The trace of the original matrix (equation 3) is equal to the sum of the eigenvalues in the 3D and 2.5D cases, using the entries of equations 10 and 12:

$$\sigma_{xx} + \sigma_{yy} + \sigma_{zz} = \sigma_1 + \sigma_2 + \sigma_3. \quad (13)$$

PERTURBATION ANALYSIS

Instead of potential U, we introduce the Green's function $G = U/I$. Equations 1, 11a, and 11b take the form

$$D(\boldsymbol{\sigma})G_s = -\frac{1}{c}\delta(r - r_s), \quad (14)$$

where $G_s = \tilde{G}_s(r)$ or $G_s = G_s(r)$ for the 2.5D or 3D case, respectively, for which $c = 2$ or $c = 1$, respectively. The tilde above G denotes spatial Fourier transform with respect to the strike or y-direction. The differential operator is defined by

$$D(\boldsymbol{\sigma})G_s = \begin{cases} \nabla \cdot (\boldsymbol{\sigma} \nabla \tilde{G}_s) - k_y^2 \sigma_{yy} \tilde{G}_s, & r \in \Omega(x, z); \\ \nabla \cdot (\boldsymbol{\sigma} \nabla G_s), & r \in \Omega(x, y, z). \end{cases} \quad (15)$$

From this definition, one can easily show the operator $D(\boldsymbol{\sigma})$ is linear:

$$D(\boldsymbol{\sigma}_A + \lambda \boldsymbol{\sigma}_B) = D(\boldsymbol{\sigma}_A) + \lambda D(\boldsymbol{\sigma}_B) \quad \forall\, \lambda \in R. \quad (16)$$

It is also self-adjoint for the integration (Carey and Oden, 1983; Zhou and Greenhalgh, 1999):

$$\int_\Omega W(r)D(\boldsymbol{\sigma})G_s(r)d\Omega = \int_\Omega G_s(r)D(\boldsymbol{\sigma})W(r)d\Omega \quad (17)$$

$$\forall W(r) \in C^1(\Omega).$$

For any small perturbation $\delta\boldsymbol{\sigma}$ in the medium properties, we have

$$D(\boldsymbol{\sigma} + \delta\boldsymbol{\sigma})(G_s + \delta G_s) = -\frac{1}{c}\delta(r - r_s). \quad (18)$$

Applying the linear property and equation 14, we obtain

$$D(\boldsymbol{\sigma})\delta G_s = -D(\delta\boldsymbol{\sigma})G_s - D(\delta\boldsymbol{\sigma})\delta G_s. \quad (19)$$

To solve equation 19, we use the conjugate Green's function by placing an adjoint source at the receiver (potential electrode) position, defined by

$$D(\boldsymbol{\sigma})G_p = -\frac{1}{c}\delta(r - r_p), \quad r, r_p \in \Omega. \quad (20)$$

Multiplying δG_s with equation 20 and calculating the integration over the domain in terms of the self-adjoint property (equation 17), we have

$$\begin{aligned} \delta G_s(r_p) &= -c\int_\Omega G_p(r)D(\boldsymbol{\sigma})\delta G_s(r)d\Omega \\ &= c\int_\Omega G_p(r)D(\delta\boldsymbol{\sigma})G_s(r)d\Omega + o(\|\delta\boldsymbol{\sigma}\|^2). \end{aligned} \quad (21)$$

Substituting equation 15 for 21, integrating by parts, and ignoring the higher-order terms, we obtain the linear relationship between the change (perturbation) of the Green's function and the perturbation in the medium properties $\delta\boldsymbol{\sigma}$ for the 2.5D case:

$$\begin{aligned} \delta\tilde{G}_s(r_p) &= -2\int_\Omega [\delta\boldsymbol{\sigma} \nabla \tilde{G}_s(r) \cdot \nabla \tilde{G}_p(r) \\ &\quad + k_y^2 \delta\sigma_{yy}\tilde{G}_s(r)\tilde{G}_p(r)]d\Omega \\ &= -2\int_\Omega \left[\delta\sigma_{xx}\frac{\partial\tilde{G}_s}{\partial x}\frac{\partial\tilde{G}_p}{\partial x} + \delta\sigma_{xz}\left(\frac{\partial\tilde{G}_s}{\partial z}\frac{\partial\tilde{G}_p}{\partial x}\right.\right. \\ &\quad \left. + \frac{\partial\tilde{G}_s}{\partial x}\frac{\partial\tilde{G}_p}{\partial z}\right) + \delta\sigma_{zz}\frac{\partial\tilde{G}_s}{\partial z}\frac{\partial\tilde{G}_p}{\partial z} \\ &\quad \left. + k_y^2\delta\sigma_{yy}\tilde{G}_s(r)\tilde{G}_p(r)\right]d\Omega. \end{aligned} \quad (22)$$

For the 3D situation, we have

$$\delta G_s(r_p) = -\int_\Omega [\delta\boldsymbol{\sigma}\nabla G_s(r)\cdot\nabla G_p(r)]d\Omega$$
$$= -\int_\Omega \left[\delta\sigma_{xx}\frac{\partial G_s}{\partial x}\frac{\partial G_p}{\partial x} + \delta\sigma_{xy}\left(\frac{\partial G_s}{\partial y}\frac{\partial G_p}{\partial x} + \frac{\partial G_s}{\partial x}\frac{\partial G_p}{\partial y}\right) + \delta\sigma_{xz}\left(\frac{\partial G_s}{\partial z}\frac{\partial G_p}{\partial x} + \frac{\partial G_s}{\partial x}\frac{\partial G_p}{\partial z}\right) + \delta\sigma_{yy}\frac{\partial G_s}{\partial y}\frac{\partial G_p}{\partial y} + \delta\sigma_{yz}\left(\frac{\partial G_s}{\partial z}\frac{\partial G_p}{\partial y} + \frac{\partial G_s}{\partial y}\frac{\partial G_p}{\partial z}\right) + \delta\sigma_{zz}\frac{\partial G_s}{\partial z}\frac{\partial G_p}{\partial z}\right]d\Omega. \quad (23)$$

Here, we assume that at the boundary of Ω no perturbation occurs in the conductivity ($\delta\boldsymbol{\sigma} = \mathbf{0}$).

FRÉCHET DERIVATIVES

According to equations 22 and 23 and by applying a model discretization scheme — either constant point $\delta\boldsymbol{\sigma}(r) = \delta\boldsymbol{\sigma}_k\delta(r - r_k)$, $r \in \Omega_k$, or constant block $\delta\boldsymbol{\sigma}(r) = \delta\boldsymbol{\sigma}_k$, $r \in \Omega_k$, where Ω_k are small subdomains composing Ω — we obtain the following results for the Fréchet derivatives. For the constant-point approximation 2.5D case,

$$\frac{\partial G_s(r_p)}{\partial(\sigma_{\alpha\beta})_k} = -\begin{cases} 2F_c^{-1}[k_y^2\tilde{G}_s(r_k)\tilde{G}_p(r_k)], & (\alpha=\beta=y) \\ c_{\alpha\beta}F_c^{-1}\left(\frac{\partial\tilde{G}_s}{\partial\alpha}\frac{\partial\tilde{G}_p}{\partial\beta} + \frac{\partial\tilde{G}_p}{\partial\alpha}\frac{\partial\tilde{G}_s}{\partial\beta}\right)_{r_k}, & (\alpha,\beta=x,z) \end{cases}. \quad (24)$$

For the constant-point approximation 3D case,

$$\frac{\partial G_s(r_p)}{\partial(\sigma_{\alpha\beta})_k} = -c_{\alpha\beta}\left(\frac{\partial G_s}{\partial\alpha}\frac{\partial G_p}{\partial\beta} + \frac{\partial G_p}{\partial\alpha}\frac{\partial G_s}{\partial\beta}\right)_{r_k}, \quad (25)$$

$$(\alpha,\beta = x,y,z).$$

For the constant-block approximation 2.5D case,

$$\frac{\partial G_s(r_p)}{\partial(\sigma_{\alpha\beta})_k} = -\begin{cases} 2w_lF_c^{-1}[k_y^2(\tilde{G}_s\tilde{G}_p)_{r_l}], & (\alpha=\beta=y,\ r_l\in\Omega_k) \\ c_{\alpha\beta}w_lF_c^{-1}\left(\frac{\partial\tilde{G}_s}{\partial\alpha}\frac{\partial\tilde{G}_p}{\partial\beta} + \frac{\partial\tilde{G}_p}{\partial\alpha}\frac{\partial\tilde{G}_s}{\partial\beta}\right)_{r_l}, & (\alpha,\beta=x,z;\ r_l\in\Omega_k) \end{cases}. \quad (26)$$

For the constant-block approximation 3D case,

$$\frac{\partial G_s(r_p)}{\partial(\sigma_{\alpha\beta})_k} = -c_{\alpha\beta}w_l\left(\frac{\partial G_s}{\partial\alpha}\frac{\partial G_p}{\partial\beta} + \frac{\partial G_p}{\partial\alpha}\frac{\partial G_s}{\partial\beta}\right)_{r_l}, \quad (27)$$

$$(\alpha,\beta = x,y,z,\ r_l\in\Omega_k),$$

where $c_{\alpha\beta} = 1$ if $\alpha = \beta$ and $c_{\alpha\beta} = 2$ if $\alpha \neq \beta$. The symbol F_c^{-1} denotes inverse Fourier cosine transformation with respect to wavenumber k_y. The quantity w_l is the product of the Gaussian weights in the various coordinate directions involved in a Gaussian quadrature approach to performing the volume integration.

The derivative formulas 24–27 may be used directly for anisotropic resistivity inversion to update the parameter estimates, once the source and adjoint Green's functions have been calculated for each subsurface point. This is illustrated in Figure 2. For each subsurface point k, we can calculate the sensitivities for a given electrode configuration (source s and receiver p) in terms of the two Green's functions, $G_s(\mathbf{r_{kS}})$ and $G_p(\mathbf{r_{kP}})$. For the common four-electrode systems, the sensitivities can be computed from the pole-pole responses given above by simple superposition (algebraic addition).

NUMERICAL METHOD

Applying a numerical method such as the finite-element method (Li and Spitzer, 2005) or the Gaussian quadrature grid method (Zhou et al., 2009) to the governing equation, one has the following linear equation system:

$$\mathbf{M}(\boldsymbol{\sigma})\mathbf{G}_s = \mathbf{b}_s, \quad (28)$$

where $\mathbf{G}_s = \{G_{si}, i = 1,2,\ldots,N\}$ is the vector whose components are the values of the Green's function at all nodes, $\mathbf{b}_s = \{\delta_{is}, i = 1,2,\ldots,N\}$ is the source vector whose components are zero except for the one ($\delta_{ss} = 1$) at the node coinciding with the source location, and $\mathbf{M}(\boldsymbol{\sigma})$ is an $N \times N$ symmetric matrix, which is calculated by

$$M_{ij}(\boldsymbol{\sigma}) = \begin{cases} 2\int_{\Omega_k}[\boldsymbol{\sigma}\nabla l_i(r)\cdot\nabla l_j(r) + k_y^2\sigma_{yy}l_i(r)l_j(r)]d\Omega, & r\in\Omega_k(x,z) \\ \int_{\Omega_k}[\boldsymbol{\sigma}\nabla l_i(r)\cdot\nabla l_j(r)]d\Omega, & r\in\Omega_k(x,y,z) \end{cases} \quad (29)$$

in terms of the Variational Principle and subdomain or element inte-

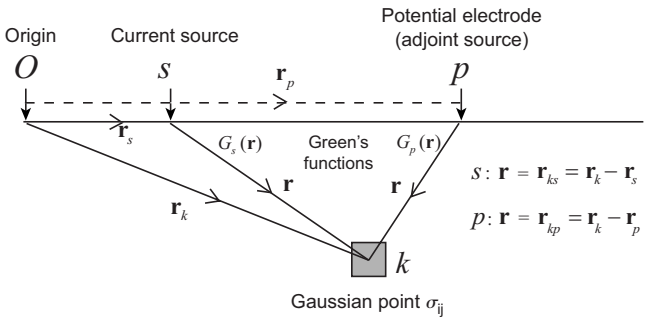

Figure 2. Schematic of Frechet derivatives (or sensitivities) at subsurface point k for a true current source at point s and an adjoint source at potential electrode position p. The Green's functions from both sources and/or their gradients are required in the formulation.

gration. Here, $l_i(r)$ are the Lagrange interpolants or shape functions.

Differentiating equation 28 with respect to $(\sigma_{\alpha\beta})_k$, we have

$$\mathbf{M}(\boldsymbol{\sigma})\frac{\partial \mathbf{G}_s}{\partial(\sigma_{\alpha\beta})_k} = -\frac{\partial \mathbf{M}(\boldsymbol{\sigma})}{\partial(\sigma_{\alpha\beta})_k}\mathbf{G}_s. \tag{30}$$

To solve equation 30, we apply equation 28 to multiple source vectors $\mathbf{I} = (\mathbf{b}_{s_1}, \mathbf{b}_{s_2}, \ldots, \mathbf{b}_{s_N})$ and the corresponding Green's function matrix $\mathbf{G}_{N\times N} = (\mathbf{G}_{s_1}, \mathbf{G}_{s_2}, \ldots, \mathbf{G}_{s_N})$. We have the identity

$$\mathbf{M}(\boldsymbol{\sigma})\mathbf{G}_{N\times N} = \mathbf{I}. \tag{31}$$

Multiplying the vector $\mathbf{b}_p^T\mathbf{G}_{N\times N}^T = \mathbf{G}_p^T$ with equation 29 and applying the symmetry property of $\mathbf{M}(\boldsymbol{\sigma})$ and equation 31, we obtain the derivatives

$$\frac{\partial G_s(r_p)}{\partial(\sigma_{\alpha\beta})_k} = -\mathbf{G}_p^T\frac{\boldsymbol{\partial}\mathbf{M}(\boldsymbol{\sigma})}{\boldsymbol{\partial}(\sigma_{\alpha\beta})_k}\mathbf{G}_s. \tag{32}$$

Substituting equation 29 for 32 and noting that most components of the matrix $\partial\mathbf{M}(\boldsymbol{\sigma})/\partial(\sigma_{\alpha\beta})_k$ are zero except for the kth subdomain Ω_k that has conductivity tensor $\boldsymbol{\sigma}_k$, equation 32 becomes, for the 2.5D and 3D cases, respectively,

$$\begin{aligned}\frac{\partial G_s(r_p)}{\partial(\sigma_{\alpha\beta})_k} &= -F_c^{-1}\left\{2\int_{\Omega_k}\left[\frac{\partial\boldsymbol{\sigma}_k}{\partial(\sigma_{\alpha\beta})_k}\nabla\left[\sum_i l_i(r)\tilde{G}_{pi}\right]\right.\right.\\ &\quad\left.\cdot\,\nabla\left[\sum_j l_j(r)\tilde{G}_{sj}\right] + k_y^2\frac{\partial\sigma_{yy}}{\partial(\sigma_{\alpha\beta})_k}\left[\sum_i l_i(r)\tilde{G}_{pi}\right]\right.\\ &\quad\left.\left.\times\left[\sum_j l_j(r)\tilde{G}_{sj}\right]d\Omega\right\}\right.\\ &= -F_c^{-1}\left\{2\int_{\Omega_k}\left[\frac{\partial\boldsymbol{\sigma}_k}{\partial(\sigma_{\alpha\beta})_k}\nabla\tilde{G}_p(r)\cdot\nabla\tilde{G}_s\right.\right.\\ &\quad\left.\left.+\,k_y^2\frac{\partial\sigma_{yy}}{\partial(\sigma_{\alpha\beta})_k}\tilde{G}_s\tilde{G}_p\right]d\Omega\right\},\end{aligned} \tag{33}$$

$$\begin{aligned}\frac{\partial G_s(r_p)}{\partial(\sigma_{\alpha\beta})_k} &= -\int_{\Omega_k}\left[\frac{\partial\boldsymbol{\sigma}_k}{\partial(\sigma_{\alpha\beta})_k}\nabla\left[\sum_i l_i(r)G_{pi}\right]\right.\\ &\quad\left.\cdot\,\nabla\left[\sum_j l_j(r)G_{sj}\right]\right]d\Omega\\ &= -\int_{\Omega_k}\left[\frac{\partial\boldsymbol{\sigma}_k}{\partial(\sigma_{\alpha\beta})_k}\nabla\tilde{G}_p(r)\cdot\nabla\tilde{G}_s\right]d\Omega.\end{aligned} \tag{34}$$

Applying the constant-point $\delta\boldsymbol{\sigma}(r) = \delta\boldsymbol{\sigma}_k\delta(r-r_k)$, $r\in\Omega_k$, or constant-block $\delta\boldsymbol{\sigma}(r) = \delta\boldsymbol{\sigma}_k$, $r\in\Omega_k$, model parameterization schemes to equations 33 and 34, we find they give the same results as equations 24–27. This means the perturbation method and the numerical method are equivalent, although the former is derived by applying the self-adjoint differential operator to the perturbation analysis and the latter is based on the linear equation of the model discretization. Both apply for DC resistivity anisotropic inversion.

SENSITIVITIES IN TERMS OF PRINCIPAL CONDUCTIVITY VALUES AND DIRECTIONS

Instead of working with the components of the conductivity tensor in the geographic frame, we now consider the derivatives with respect to the principal values (and orientation angles of the symmetry axis) in the natural rock frame, which are the physically meaningful quantities. Let the model parameters be represented by $m_\nu = (\sigma_1, \sigma_2, \sigma_3, \theta_0, \phi_0)$. Accordingly, the perturbation of the conductivity tensor can be expressed by $\delta\boldsymbol{\sigma} = (\partial\boldsymbol{\sigma}/\partial m_\nu)\delta m_\nu$. Equations 22 and 23 become

$$\begin{aligned}\delta\tilde{G}_s(r_p) &= -2\int_\Omega\left\{\left[\frac{\partial\boldsymbol{\sigma}}{\partial m_\nu}\nabla\tilde{G}_s(r)\right]\cdot\nabla\tilde{G}_p(r)\right.\\ &\quad\left.+\,k_y^2\frac{\partial\sigma_{yy}}{\partial m_\nu}\tilde{G}_s(r)\tilde{G}_p(r)\right\}\delta m_\nu d\Omega\end{aligned} \tag{35}$$

and

$$\delta G_s(r_p) = -\int_\Omega\left\{\left[\frac{\partial\boldsymbol{\sigma}}{\partial m_\nu}\nabla G_s(r)\right]\cdot\nabla G_p(r)\right\}\delta m_\nu d\Omega. \tag{36}$$

Applying a discretization scheme — either constant point $\delta m_\nu(r) = \delta m_\nu\delta(r-r_k)$, $r\in\Omega_k$, or constant block $\delta m_\nu(r) = \delta m_\nu$, $r\in\Omega_k$, where Ω_k are small subdomains composing Ω — we have for the 2.5D constant-point approximation case

$$\begin{aligned}\frac{\partial G_s(r_p)}{\partial m_{\boldsymbol{\nu}}} &= -F_c^{-1}\left\{\left[\frac{\partial\boldsymbol{\sigma}}{\partial m_{\boldsymbol{\nu}}}\nabla\tilde{G}_s(r)\right]\cdot\nabla\tilde{G}_p(r)\right.\\ &\quad\left.+\,k_y^2\frac{\partial\sigma_{yy}}{\partial m_{\boldsymbol{\nu}}}\tilde{G}_s(r)\tilde{G}_p(r)\right\},\end{aligned} \tag{37}$$

$$m_{\boldsymbol{\nu}}\in(\sigma_{x'x'}, \sigma_{y'y'}, \sigma_{z'z'}, \theta_0).$$

For the 3D constant-point approximation case,

$$\frac{\partial G_s(r_p)}{\partial m_{\boldsymbol{\nu}}} = -\left[\frac{\partial\boldsymbol{\sigma}}{\partial m_{\boldsymbol{\nu}}}\nabla G_s(r)\right]\cdot\nabla G_p(r)\}, \tag{38}$$

$$m_{\boldsymbol{\nu}}\in(\sigma_{x'x'}, \sigma_{y'y'}, \sigma_{z'z'}, \theta_0).$$

For the 2.5D constant-block approximation case,

$$\begin{aligned}\frac{\partial G_s(r_p)}{\partial m_{\boldsymbol{\nu}}} &= -w_{\boldsymbol{\alpha}}F_c^{-1}\left\{\left[\frac{\partial\boldsymbol{\sigma}}{\partial m_{\boldsymbol{\nu}}}\nabla\tilde{G}_s(r)\right]\cdot\nabla\tilde{G}_p(r)\right.\\ &\quad\left.+\,k_y^2\frac{\partial\sigma_{yy}}{\partial m_{\boldsymbol{\nu}}}\tilde{G}_s(r)\tilde{G}_p(r)\right\}_{\boldsymbol{\alpha}},\end{aligned} \tag{39}$$

$m_{\boldsymbol{\nu}}\in(\sigma_{x'x'}, \sigma_{y'y'}, \sigma_{z'z'}, \theta_0)$.For the 3D constant-block approximation case,

$$\frac{\partial G_s(r_p)}{\partial m_\nu} = -w_\alpha\left\{\left[\frac{\partial\boldsymbol{\sigma}}{\partial m_\nu}\nabla G_s(r)\right]\cdot\nabla G_p(r)\right\}_\alpha, \tag{40}$$

$$m_\nu \in (\sigma_{x'x'}\,,\,\sigma_{y'y'}\,,\,\sigma_{z'z'}\,,\,\theta_0\,,\,\varphi_0).$$

Here, $\partial\boldsymbol{\sigma}/\partial m_\nu$ can be calculated by equation 10 or 12, and w_α re the Gaussian weights. The Cartesian tensor form of equation 38, for example, is

$$\frac{\partial G_s(r_p)}{\partial(m_\nu)} = -\left\{\frac{\partial\sigma_{ij}}{\partial m_\nu}\frac{\partial G_s}{\partial x_j}\frac{\partial G_p}{\partial x_i}\right\}, \tag{41}$$

where summation is implied in equation 41 through the repetition of subscripts $i\,,\,j = x\,,\,y\,,\,z$ and $x_i\,,\,x_j = x\,,\,y\,,\,z$. Expanding out in terms of the various components, the Fréchet derivatives in terms of the principal values can be written as follows for the 3D case:

$$\begin{aligned}\frac{\partial G_s(r_p)}{\partial m_\nu} = -\Bigg\{&\frac{\partial\sigma_{xx}}{\partial m_\nu}\frac{\partial G_s}{\partial x}\frac{\partial G_p}{\partial x} + \frac{\partial\sigma_{yy}}{\partial m_\nu}\frac{\partial G_s}{\partial y}\frac{\partial G_p}{\partial y}\\ &+ \frac{\partial\sigma_{zz}}{\partial m_\nu}\frac{\partial G_s}{\partial z}\frac{\partial G_p}{\partial z} + \frac{\partial\sigma_{xy}}{\partial m_\nu}\left(\frac{\partial G_s}{\partial x}\frac{\partial G_p}{\partial y}\right.\\ &\left.+ \frac{\partial G_s}{\partial y}\frac{\partial G_p}{\partial x}\right) + \frac{\partial\sigma_{xz}}{\partial m_\nu}\left(\frac{\partial G_s}{\partial x}\frac{\partial G_p}{\partial z} + \frac{\partial G_s}{\partial z}\frac{\partial G_p}{\partial x}\right)\\ &+ \frac{\partial\sigma_{yz}}{\partial m_\nu}\left(\frac{\partial G_s}{\partial y}\frac{\partial G_p}{\partial z} + \frac{\partial G_s}{\partial z}\frac{\partial G_p}{\partial y}\right)\Bigg\},\end{aligned} \tag{42}$$

where m_ν assumes any of the values

$$\sigma_{x'x'}(=\sigma_1),\sigma_{y'y'}(=\sigma_2)\,,\,\sigma_{z'z'}(=\sigma_3)\,,\,\theta_0\,,\,\varphi_0.$$

The sensitivity functions can therefore be computed from knowledge of the Green's functions for the true source G_s (current electrode s) and the adjoint source G_p (potential electrode p), which are obtained as part of the forward modeling (see Zhou et al., 2009) and the partial derivatives of the conductivity tensor with respect to each of the model parameters. The latter can be obtained by differentiating each of the elements of equation 10; they are simple trigonometric functions.

In the 2.5D case, $\sigma_{xy} = \sigma_{yz} = 0$ and all derivatives of these quantities go to zero. Also, $\sigma_{yy} = \sigma_2$; so $\partial\sigma_{yy}/\partial\sigma_2 = 1$ and all other derivatives of σ_{yy} are zero. The remaining nonzero derivatives to consider are

$$\begin{aligned}\frac{\partial\sigma_{xx}}{\partial\sigma_1} &= \cos^2\theta_0\,, \quad \frac{\partial\sigma_{xx}}{\partial\sigma_3} = \sin^2\theta_0,\\ \frac{\partial\sigma_{xx}}{\partial\theta_0} &= (\sigma_3 - \sigma_1)\sin 2\theta_0,\\ \frac{\partial\sigma_{zz}}{\partial\sigma_1} &= \sin^2\theta_0\,, \quad \frac{\partial\sigma_{zz}}{\partial\sigma_3} = \cos^2\theta_0,\\ \frac{\partial\sigma_{zz}}{\partial\theta_0} &= (\sigma_1 - \sigma_3)\sin 2\theta_0,\\ \frac{\partial\sigma_{xz}}{\partial\sigma_1} &= -\sin\theta_0\cos\theta_0\,, \quad \frac{\partial\sigma_{xz}}{\partial\sigma_3} = \sin\theta_0\cos\theta_0,\\ \frac{\partial\sigma_{xz}}{\partial\theta_0} &= 2(\sigma_3 - \sigma_1)\cos 2\theta_0.\end{aligned} \tag{43}$$

In the case of an isotropic medium, we have

$$\sigma_{xx} = \sigma_{yy} = \sigma_{zz} = \sigma \quad \text{and} \quad \sigma_{xy} = \sigma_{xz} = \sigma_{yz} = 0. \tag{44}$$

All of the cross terms disappear in equation 42, the derivatives $\partial\sigma_{ii}/\partial m_\nu$ are all equal to one, and equation 25 reduces to the dot product of the gradients of the two Green's functions:

$$\frac{\partial G}{\partial\sigma} = -\nabla G_s\cdot\nabla G_p. \tag{45}$$

This is the same result as that obtained by Zhou and Greenhalgh (1999, p. 449) using an isotropic formulation.

UNIFORM ANISOTROPIC EARTH

The numerical calculations for the Green's functions based on equation 28 and the subsequent sensitivity analysis (equations 24–27) are entirely general for the most complex heterogeneous and anisotropic medium and also apply for buried electrodes (e.g., cross-hole surveys). Nevertheless, it is instructive to examine the results for the special case of a homogeneous anisotropic earth with a point current source $\mathbf{r_s}$ on the surface and at the origin. Such a model could be used for applying a boundary value treatment (see Zhou et al., 2009) or for validating numerical solutions.

The Green's function at some interior point $\mathbf{r} = (x\,,\,y\,,\,z)$ can be calculated analytically using the formula (Li and Uren, 1998)

$$\begin{aligned}G_s &= \frac{C}{\sqrt{\mathbf{r}^T\boldsymbol{\rho}\mathbf{r}}}\\ &= \frac{C}{\sqrt{\rho_{xx}x^2 + \rho_{yy}y^2 + \rho_{zz}z^2 + 2\rho_{xy}xy + 2\rho_{xz}xz + 2\rho_{yz}yz}},\end{aligned} \tag{46}$$

where C is a constant $= (\det\rho_{ij})^{1/2}/2\pi = (\rho_1\rho_2\rho_3)^{1/2}/2\pi$ and $\boldsymbol{\sigma}(=[\sigma_{ij}]^{-1})$ is the resistivity tensor, the inverse matrix of the conductivity matrix (or tensor). The principal resistivities $\rho_1\,,\,\rho_2\,,\,\rho_3$ are the reciprocals of the principal conductivities $\sigma_1\,,\,\sigma_2\,,\,\sigma_3$. The buried source problem is more difficult to treat and was first considered by Asten (1974). The treatment includes considering an image source displaced laterally from boundary normal. An in-depth analysis is given by Li and Uren (1998).

Equation 46 can be differentiated with respect to $(x\,,\,y\,,\,z)$ to obtain analytic expressions for the Fréchet derivatives $\partial G/\partial\rho_{ij}$ (see equation 25). In the case of a TTI medium having longitudinal resistivity $\rho_l(=\rho_1=\rho_2)$, transverse resistivity $\rho_t(=\rho_3)$, and angles of the symmetry axis $\theta_0\,,\,\phi_0$ (i.e., the transverse resistivity direction), the components of the resistivity tensor reduce to (see equation 10, but interchanging conductivity for resistivity and setting $\sigma_1 = \sigma_2$),

$$\begin{pmatrix}\rho_{xx}\\ \rho_{xy}\\ \rho_{xz}\\ \rho_{yy}\\ \rho_{yz}\\ \rho_{zz}\end{pmatrix} = \begin{pmatrix}\rho_l\cos^2\theta_0\cos^2\varphi_0 + \rho_l\sin^2\varphi_0 + \rho_t\sin^2\theta_0\cos^2\varphi_0\\ 0.5(\rho_t - \rho_l)\sin^2\theta_0\sin 2\varphi_0\\ 0.5(\rho_t - \rho_l)\cos\varphi_0\sin 2\theta_0\\ (\rho_t - \rho_l)\sin^2\theta_0\sin^2\varphi_0 + \rho_l\\ 0.5(\rho_t - \rho_l)\sin\varphi_0\sin 2\theta_0\\ \rho_l\sin^2\theta_0 + \rho_t\cos^2\theta_0\end{pmatrix}. \tag{47}$$

Using these values for the resistivity tensor components in equation 46 and also using equation 38, one can compute the Fréchet deriva-

tives in terms of the four principal values: ρ_l , ρ_t , θ_0 , ϕ_0. Note, however, that $\partial G/\partial\rho_i = -(1/\rho_i^2)(\partial G/\partial\sigma_i)$, with a reversal of sign between the sensitivities expressed in terms of conductivity and resistivity.

This treatment is for a 3D (uniform) anisotropic model because the three principal axes of the tensor can take on any orientation in 3D space. For the uniform medium 2.5D problem, there is a still point source of current, but one principal axis of the resistivity tensor now points in the y-direction; hence, the other two axes are confined to the x-z-plane. It follows that $\rho_{xy} = \rho_{yz} = 0$, $\rho_{yy} = \rho_2$, all tensor components are spatially invariant, and equation 46 becomes

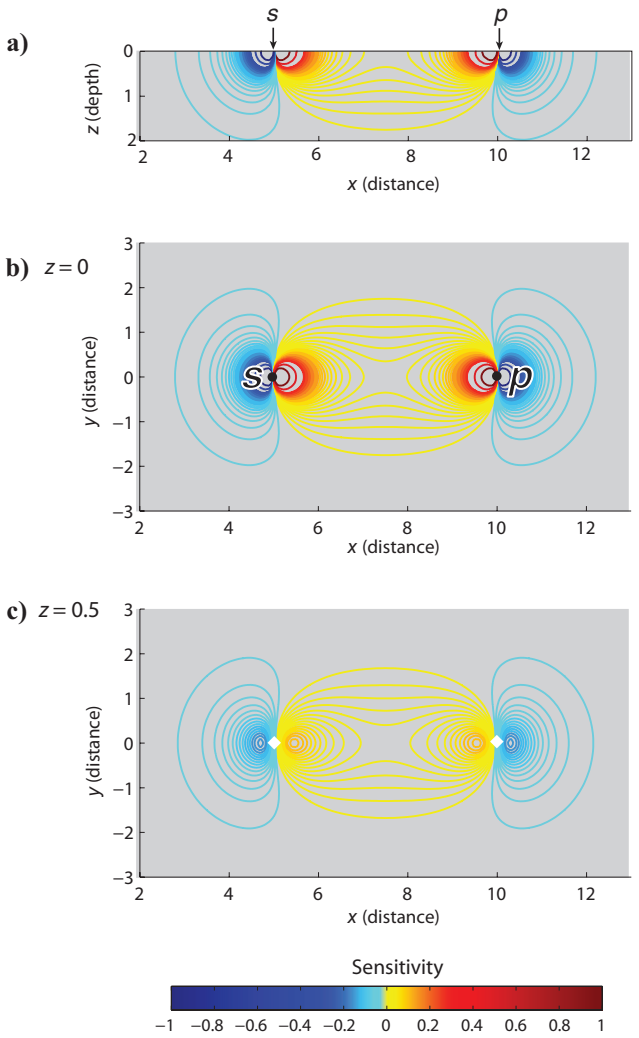

Figure 3. Fréchet derivative $dG/d\sigma$ for an isotropic model having a conductivity of 0.1 S/m. The current source is at (5,0,0) and the potential electrode is at (10,0,0). (a) The cross-sectional view at $y = 0$ and two horizontal depth slices at (b) $z = 0$ and (c) $z = 0.5$ depicting sensitivity variations in plan view are shown. For the $z = 0.5$ depth slice, the electrode positions (white diamonds) have been projected onto this plane.

$$G_s = \frac{\dfrac{C}{\sqrt{\rho_{yy}}}}{\sqrt{\dfrac{\rho_{xx}x^2 + 2\rho_{xz}xz + \rho_{zz}z^2}{\rho_{yy}} + y^2}} = \frac{C'}{\sqrt{a + y^2}}, \tag{48}$$

where

$$C' = \frac{C}{\sqrt{\rho_{yy}}} \tag{49}$$

and

$$a = \frac{1}{\rho_{yy}}(\rho_{xx}x^2 + 2\rho_{xz}xz + \rho_{zz}z^2) = \frac{1}{\rho_{yy}}(x\,,z)\begin{pmatrix}\rho_{xx} & \rho_{xz}\\ \rho_{xz} & \rho_{zz}\end{pmatrix}\begin{pmatrix}x\\ z\end{pmatrix}. \tag{50}$$

Because of the positive definite nature of the resistivity matrix $\boldsymbol{\rho}$, the quantity $a > 0$ must be positive. According to the Fourier cosine transform

$$\int_0^\infty \frac{\cos(k_y y)}{\sqrt{a + y^2}}dy = K_0(k_y\sqrt{a}), \tag{51}$$

the Fourier-transformed Green's function can be calculated in terms of the modified Bessel function of the first kind as follows:

$$\tilde{G}_s = C'K_0(k_y\sqrt{a}). \tag{52}$$

This equation can be differentiated with respect to $(x\,,z)$ to obtain the required gradient term in the expression for the Fréchet derivatives (equation 37):

$$\nabla\tilde{G}_s = \left[\frac{-K_1(k_y\sqrt{a})k_y}{2\sqrt{a}K_0(k_y\sqrt{a})}\nabla a\right]\tilde{G}_s. \tag{53}$$

Here, ∇a can be calculated from equation 50.

EXAMPLES

The main purpose of this paper is to develop a theoretical formulation for numerical calculation of the Fréchet derivatives in 3D or 2.5D anisotropic resistivity inversion. In this section, we illustrate some of the sensitivity patterns and how they depend on the anisotropic parameters. This is done for a homogeneous medium to permit easy comparison with the isotropic case and because not even the uniform medium anisotropic sensitivity functions have been considered in the past. Heterogeneous, anisotropic models will be the subject of a separate paper. The homogeneous anisotropic medium can be dealt with analytically, so there is no need to use a finite-element or similar numerical approach. Should heterogeneous models need to be considered, then one must use equation 28 as a starting point for obtaining the Green's functions. In a companion paper (Wiese et al., 2009), we give a more exhaustive treatment of the sensitivity patterns for various arrays and consider a wide range of parameter variations.

We first consider, for reference purposes, the simple case of a homogeneous, isotropic half-space. The current electrode is located at (5,0,0) and the potential electrode is located at (10,0,0). The ground conductivity is 0.1 S/m (resistivity is 10 Ω-m). Figure 3 shows the Fréchet derivatives at two depth slices, $z = 0$ and $z = 0.5$ units, and in cross section for a profile through both electrodes. Note the symmetry of the patterns and the decrease of sensitivity with depth. The sensitivities are largest in magnitude in the vicinity of the electrodes. The derivatives actually change sign around the electrodes, being positive between the electrodes and negative on either side. An increase in conductivity in a region of positive sensitivity results in a greater potential being measured, whereas a decrease in conductivity in a positive sensitivity region decreases the measured potential value. The opposite applies for the negative sensitivity regions.

Next we consider a homogeneous, anisotropic model having a tilted axis of symmetry. The longitudinal conductivity (0.1 S/m) is four times larger than the transverse conductivity (0.025 S/m), yielding a coefficient of anisotropy λ of two. Again, the current electrode is at (5,0,0) and the potential electrode is at (10,0,0). In the first set of plots, the strike of the plane of stratification is held fixed at 90° ($\phi_0 = 0°$). The dip angle θ_0 is allowed to vary from 0° (horizontal beds) to 90° (vertical plane of stratification).

Figure 4 shows a series of cross sections in the x-z-plane ($y = 0$) for the longitudinal conductivity Frechet derivative $dG/d\sigma_l$. Each plot corresponds to a different dip: 0°, 15°, 45°, 75°, and 90°. The sensitivity pattern for $\theta_0 = 0°$ is very similar to the isotropic equivalent; the contours are concentrated toward the surface and elongated along it. This is confirmed in the plan view (Figure 5), which shows the sensitivity values at the surface as a function of position. The positive contours are stretched along the line intersecting the electrodes (x-axis).

One can also see in Figure 4 that the negative sensitivity contour sections are extended greatly along the strike direction (y-axis) and show some curvature toward the opposite electrode, as a departure from the isotropic pattern. The sensitivity patterns in the x-z-plane (Figure 4) for all dips other than 0° are distinctly asymmetrical, with the contours elongated in the plane of stratification. Sensitivity is thus smallest in magnitude along lines orthogonal to the stratification. All plots exhibit shifts of negative and positive contours of sensitivity such that they follow the direction of highest conductivity (orthogonal to $\hat{z}'$). The surface display (Figure 5) shows that the sensitivity decreases markedly with increasing θ_0. For all angles, the surface sensitivity pattern is symmetrical about the line intersecting the electrodes. For the vertically dipping beds, the sensitivity values are very low in magnitude and entirely negative.

The corresponding plots for the transverse-resistivity Frechet derivatives $dG/d\sigma_t$ are given in Figures 6 and 7. For a vertical axis of symmetry ($\theta_0 = 0°$), or the so-called VTI medium) the sensitivities are entirely negative, with two regions of large negative sensitivity beneath the electrodes and elongated toward each other. The $z = 0$ depth slice (Figure 7) shows no sensitivity at the surface. This is a manifestation of the Paradox of Anisotropy, discussed by Keller and Frischknecht (1970). For dips of 15°, 45°, and 75°, the sensitivity patterns in the x-z-plane are all asymmetrical (Figure 6), the contours being elongated in a direction parallel to the dip of stratification. The steepness of the pattern increases with increasing θ_0. In comparison with the corresponding $dG/d\sigma_l$ patterns (Figure 4), there is greater sensitivity at depth. Although the contours are elongated in a direction parallel to the stratification, sensitivity is smallest in magnitude along the lines drawn through separate electrodes and parallel to the stratification. This is in marked contrast to $dG/d\sigma_l$, which exhibits greatest sensitivity in this direction. For the surface ($z = 0$) slices (Figure 7), the patterns are all symmetric about the x-axis and elongated in the strike direction. The transverse conductivity sensitivity for a dip of 90° shows a symmetric pattern that resembles the isotropic plot elongated in the vertical direction (along the plane of stratification).

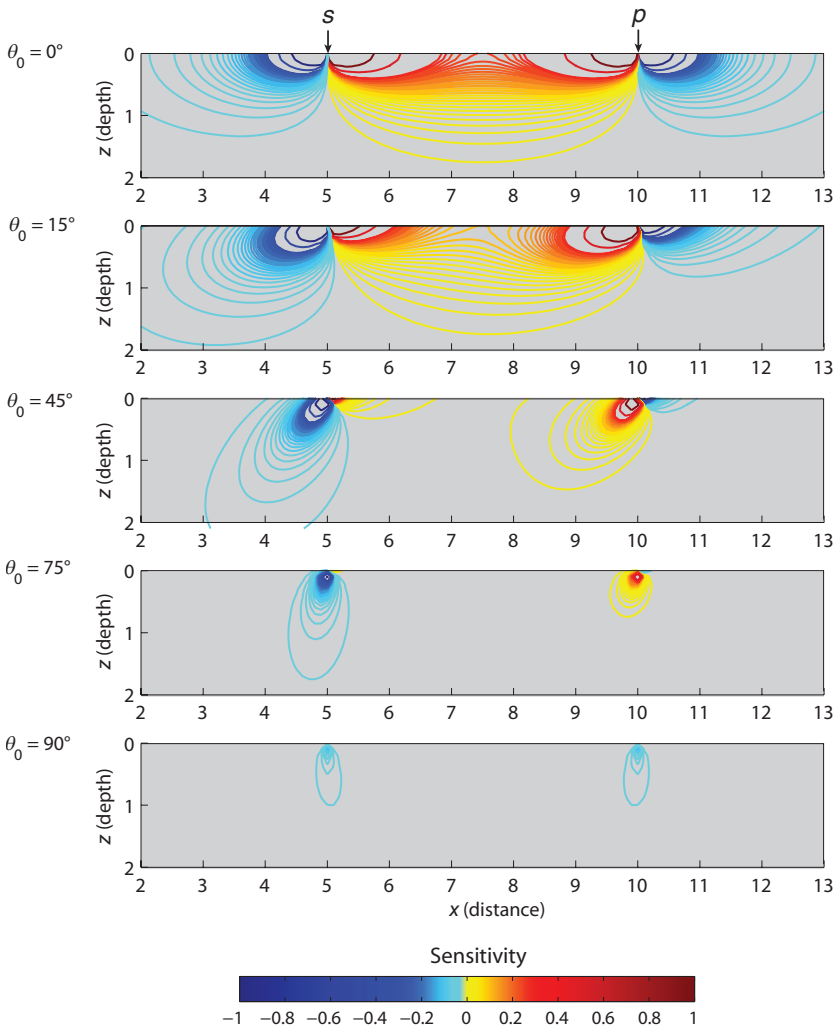

Figure 4. Longitudinal conductivity Fréchet derivative $dG/d\sigma_l$ variations in the subsurface for an anisotropic model having longitudinal conductivity of 0.1 S/m, transverse conductivity of 0.025 S/m, and strike of the symmetry axis of 0°. The various sensitivity plots are for different dips of the symmetry axis θ_0 for 0°, 15°, 45°, 75°, and 90°. The profiles are perpendicular to the strike of the plane of stratification. The electrodes are again at (5,0,0) and (10,0,0).

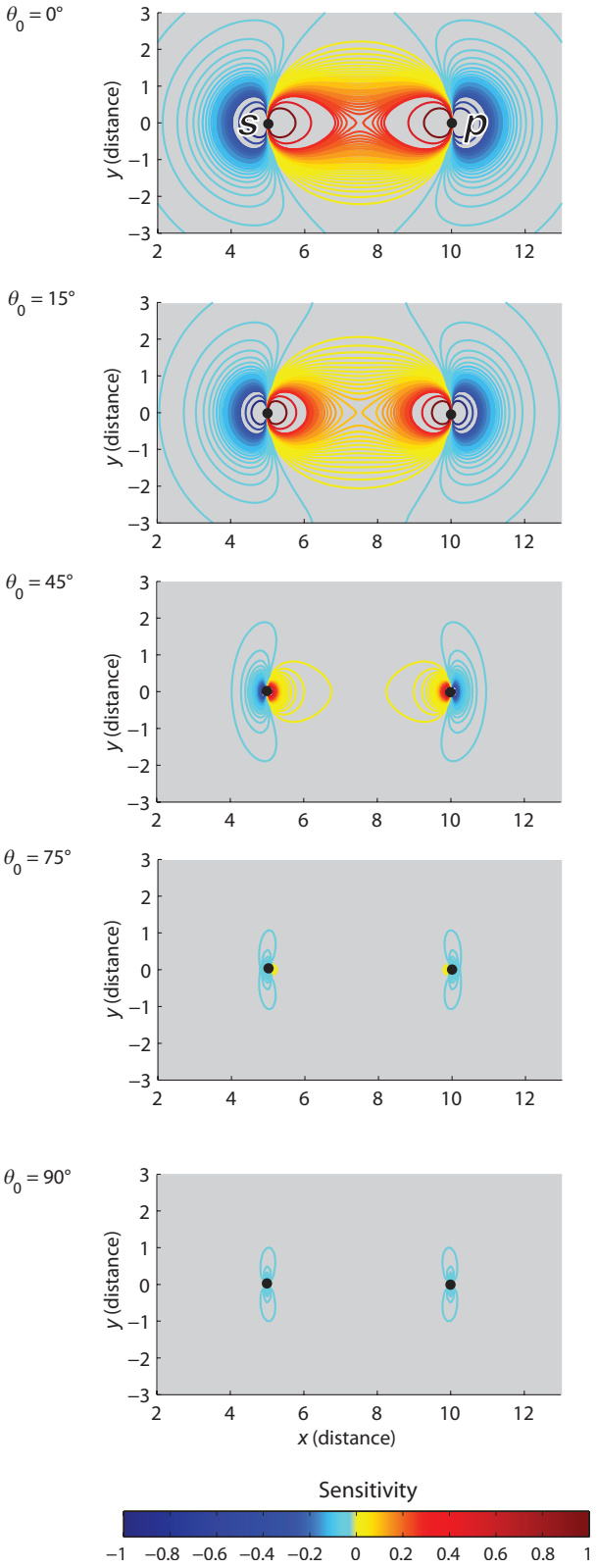

Figure 5. Fréchet derivative $dG/d\sigma_t$ plots at the surface ($z = 0$) for the same model and electrode configuration as Figure 4. Note the symmetry of the plots and the decrease in sensitivity with increasing dip.

Finally, we show the effect of azimuth of the symmetry axis on the sensitivity patterns. Figures 8–10 are plots of $dG/d\sigma_t$ for the same anisotropic structure and electrode configuration but this time for a strike of the symmetry axis of 45° (plane of stratification strike $= 45° + 90° = 135°$). From the surface slices ($z = 0$) shown in Figure 9, we can see that the x-axis symmetry is broken as a result of the bedding-plane strike no longer being 90°. If two imaginary lines are drawn through the electrodes in the strike direction ($\phi_0 + 90°$), the regions of positive and negative sensitivities do not cross boundaries defined by these lines and are largest in value orthogonal to the strike and close to the electrodes. The cross sections for the x-z-plane (Figure 8) show a progressive tilting of the sensitivity patterns as dip increases. The $\theta_0 = 0°$ plot is entirely negative and symmetrical. All other dip angles yield positive and negative sensitivities and are asymmetrical because the cross section is not perpendicular to strike. Only at a dip of $\theta_0 = 90°$ is the symmetry restored. Interestingly, the sensitivity is actually zero at all points on the surface for a

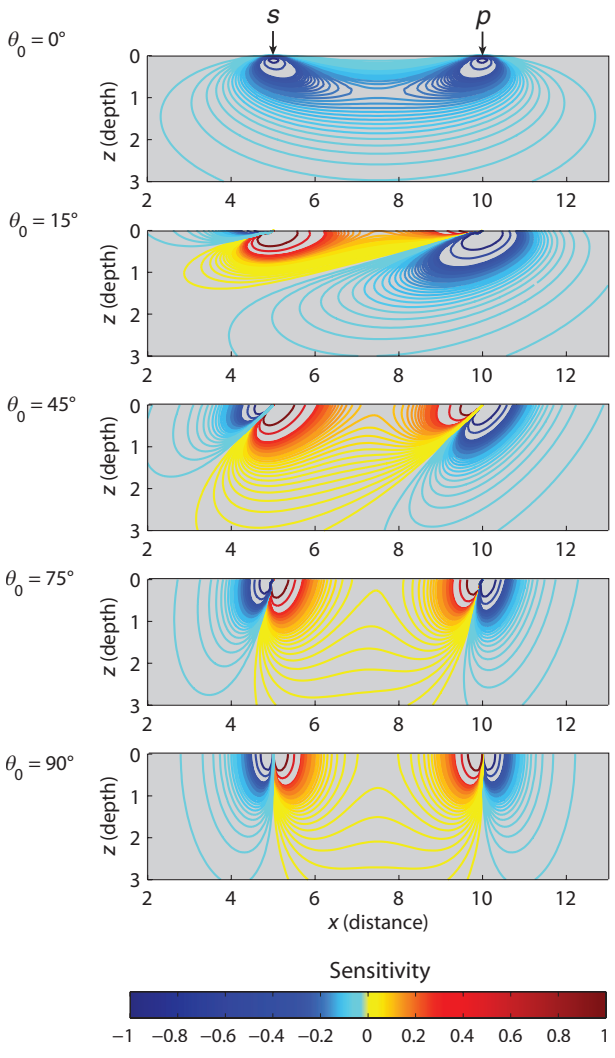

Figure 6. Transverse conductivity Fréchet derivative $dG/d\sigma_t$ variations for the same anisotropic model and electrode configuration as in Figure 4. The various sensitivity plots are for differing dips of the symmetry axis, as indicated. The profiles are perpendicular to the strike of the plane of stratification.

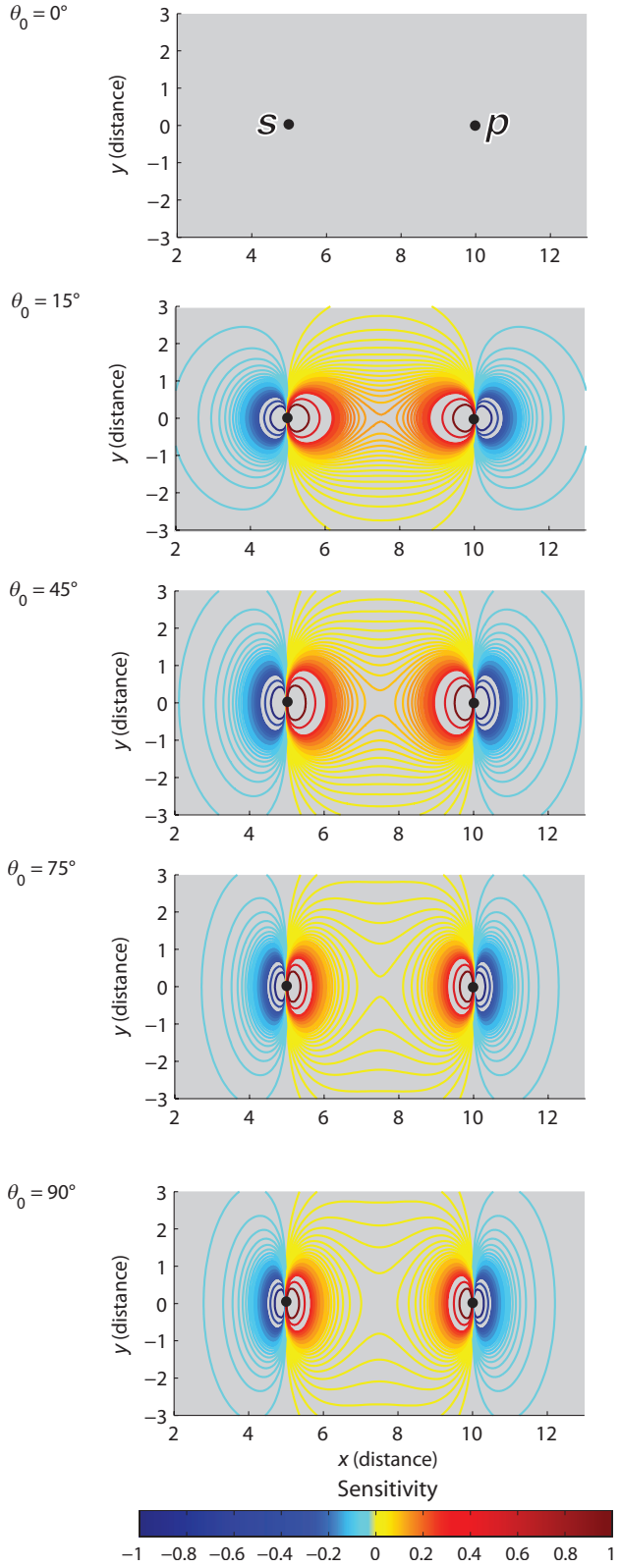

Figure 7. Fréchet derivative $dG/d\sigma_t$ plots at the surface ($z = 0$) for the same model and electrode configuration as in Figure 6. All patterns are symmetrical about the x-axis. In the case of zero dip, the sensitivity is zero.

dip of 0° (Figure 9), but for other dips the magnitude of the sensitivity is appreciable and the contours extend to modest depths.

Figure 10 shows the sensitivity variations in plan view at a depth of $z = 0.5$ units. There is considerable change in the pattern for dips over the range 0°–45°, after which the pattern looks very similar. The contours are elongated in the direction of the strike of the stratification plane (maximum conductivity direction). The large change from null sensitivity in the case of zero dip (Figure 9, surface slice) to marked sensitivity in the case of zero dip (Figure 10, depth slice $= 0.5$ units) conveys a vital point about survey design: A strong VTI anisotropy cannot be characterized unless downhole electrodes are included in a field survey. More generally, when the observation plane is perpendicular to the axis of symmetry, the anisotropy cannot be detected, so full 3D measurements are really required. Furthermore, the large change in Figure 10 from 0° dip to 15° dip indicates that an inversion scheme probably will be unstable unless both downhole and surface electrodes are used. In reality, rocks exhibit

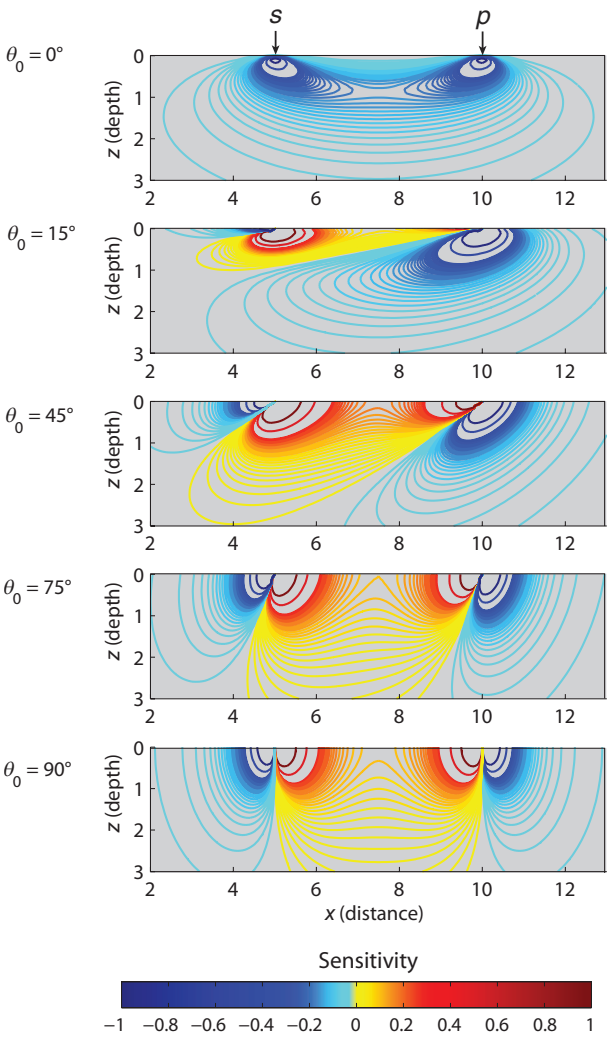

Figure 8. Sensitivity variations $dG/d\sigma_t$ for the same model as Figure 4, but the strike of the symmetry axis is now 45°, not 0°. The dip is again reflected in the asymmetry and steepening of the patterns. The contours are elongated in the direction of the plane of stratification.

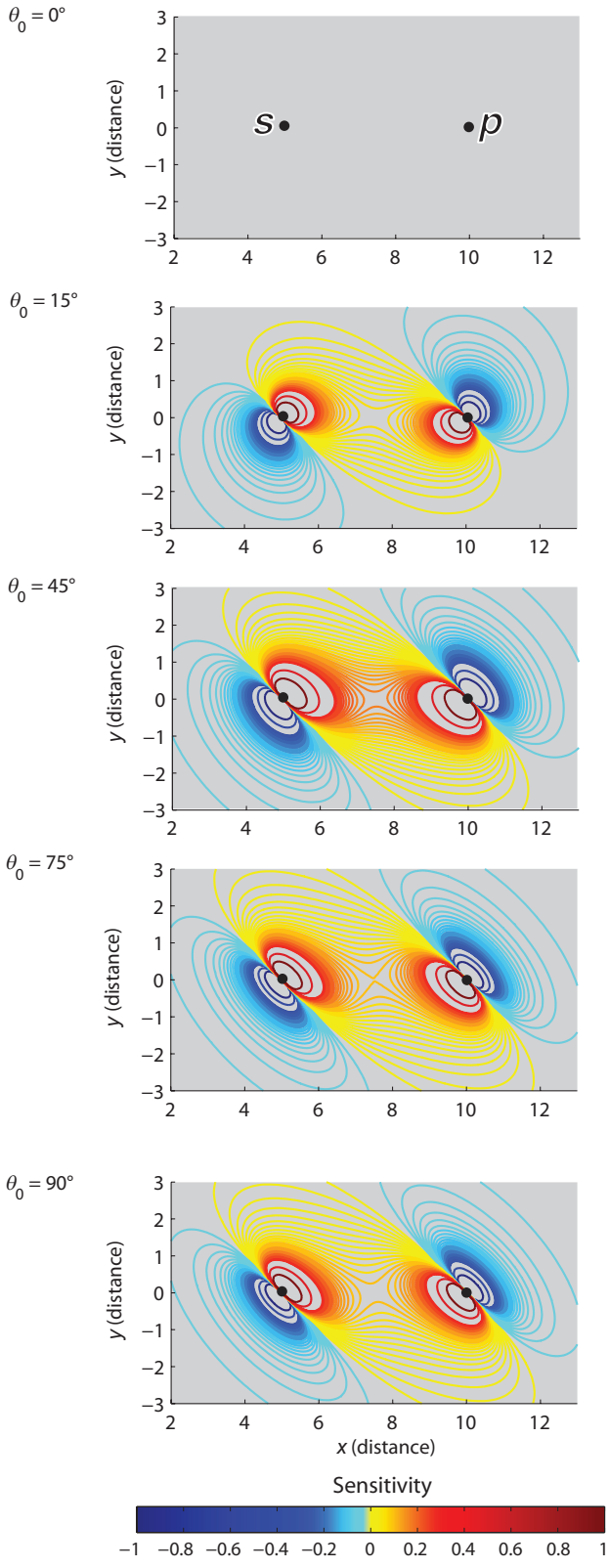

Figure 9. Companion surface sensitivity plots for Figure 8. The 45° strike is now reflected in the asymmetry about the *x*-axis and in the alignment of the patterns parallel to the strike of the plane of stratification.

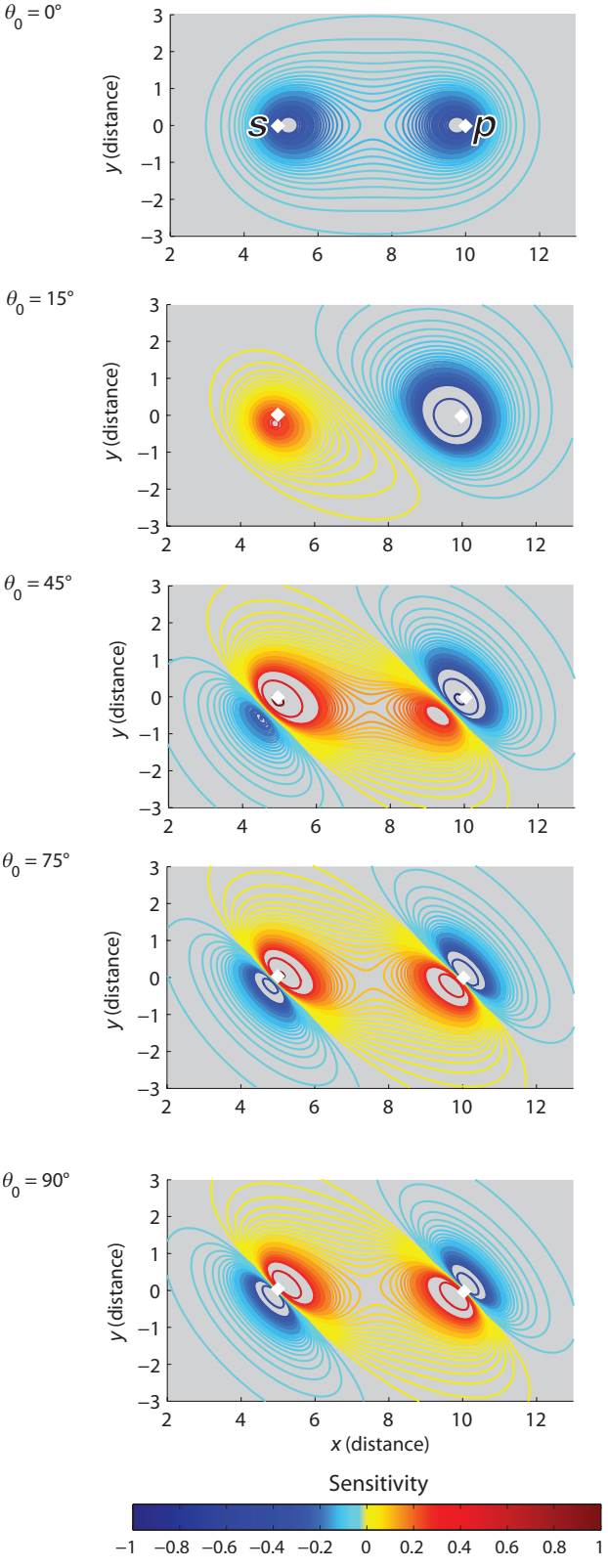

Figure 10. Depth slices at $z = 0.5$ units, showing transverse conductivity sensitivity variations in plan view for the same TTI model having 45° strike and various dips. Note the sudden changes in the pattern for dips of 0° and 45°. The projected electrode positions onto the $z = 0.5$ plane are shown as white diamonds.

variable dips for the anisotropic axis, so isolation of an effective dip may be difficult.

CONCLUSIONS

We present a general perturbation formulation for computing the Fréchet derivatives in 3D and 2.5D resistivity inversion, in which the model is heterogeneous and anisotropic. The formulation involves the Green's functions for the true current source and the adjoint source, which must be computed using a numerical method such as the finite-element method. The equations also involve the derivatives of the conductivity tensor with respect to the principal conductivity values and orientation angles of the symmetry axis. We derive analytic formulas for computing these derivatives. Examples are presented, showing the sensitivity patterns in both plan and cross-sectional view for homogeneous TI models in which the dip and strike of the symmetry axis are varied. These anisotropic sensitivity plots show some previously unreported general trends.

For the longitudinal conductivity Fréchet derivative, regions of sensitivity are located along the lines intersecting the electrodes in the direction of the stratification plane. Sensitivity decreases with distance away from this axis (and distance from the electrode). Perpendicular to this axis, there is little to no sensitivity. The trend holds for sensitivities on the surface and at depth, where it is apparent that the contours are elongated along lines perpendicular to the dip.

For the transverse resistivity Fréchet derivative, there is zero sensitivity along the lines intersecting the respective electrodes that run parallel to the stratification plane. However, the largest sensitivity regions are centered on a line intersecting the respective electrode that runs orthogonal to the stratification. The regions are elongated along the stratification plane but do not intersect the lines that run parallel from the electrodes. The examples also show significant differences in the sensitivities compared to the isotropic pattern. Therefore, failure to account for anisotropy (where it exists) in an inversion may result in false deductions about the subsurface structure.

REFERENCES

Asten, M. W., 1974, The influence of electrical anisotropy on mise-a-la-masse surveys: Geophysical Prospecting, **22**, 238–245.

Bhattacharya, P. K., and H. P. Patra, 1968, Direct current geoelectric sounding: Principles and applications: Elsevier Science Publ. Co., Inc.

Broyden, C. G., 1965, A class of methods for solving nonlinear simultaneous equations: Mathematics of Computation, **19**, 577–593.

Carey, G. F., and J. T. Oden, 1983, Finite elements: A second course, vol. II: Prentice-Hall International.

Herwanger, J. V., C. C. Pain, A. Binley, C. R. E. de Oliveira, and M. H. Worthington, 2004, Anisotropic resistivity tomography: Geophysical Journal International, **158**, 409–425.

Keller, G. V., and F. C. Frischknecht, 1970, Electrical methods in geophysical prospecting: Pergamon Press, Inc.

Lesur, V., M. Cuer, and A. Starch, 1999, 2D and 3D interpretation of electrical tomography experiments, Part 2: The inverse problem: Geophysics, **64**, 396–402.

Li, P., and N. F. Uren, 1998, Analytical solution for the electric potential due to a point source in an arbitrarily anisotropic half-space: Journal of Engineering Mathematics, **33**, 129–140.

Li, Y., and K. Spitzer, 2005, Finite element resistivity modelling for three-dimensional structures with arbitrary anisotropy: Physics of the Earth and Planetary Interiors, **150**, 15–27.

Loke, M. H., and R. D. Barker, 1995, Least-squares deconvolution of apparent resistivity pseudosections: Geophysics, **60**, 1682–1690.

——–, 1996, Rapid least squares inversion of apparent resistivity pseudosections by a quasi-Newton method: Geophysical Prospecting, **44**, 131–152.

McGillivray, P. R., and D. W. Oldenburg, 1990, Method for the calculating Fréchet derivatives for the non-linear inverse problem: A comparative study: Geophysical Prospecting, **38**, 499–524.

Maurer, H. R., and S. Friedel, 2006, Outer space sensitivities in geoelectric tomography: Geophysics, **71**, no. 3, G93–G96.

Menke, W., 1989, Geophysical data analysis: Discrete inverse theory: Academic Press Inc.

Onsager, L., 1931, Reciprocal relations in irreversible processes: Physical Review, **37**, 405–426.

Pain, C., J. Herwanger, J. Saunders, M. Worthington, and C. Oliveira, 2003, Anisotropic resistivity inversion: Inverse Problems, **19**, 1081–1111.

Park, S. K., and G. P. Van, 1991, Inversion of pole-pole data for 3-D resistivity structure beneath arrays of electrodes: Geophysics, **56**, 951–960.

Sasaki, Y., 1994, 3D resistivity inversion using the finite-element method: Geophysics, **59**, 1839–1848.

Smith, N. C., and K. Vozoff, 1984, Two-dimensional DC resistivity inversion for dipole-dipole data: IEEE Transactions on Geosciences and Remote Sensing, **GE 22**, 21–28.

Spitzer, K., 1998, The three-dimensional DC sensitivity for surface and subsurface sources: Geophysical Journal International, **134**, 736–746.

Stummer, P., H. R. Maurer, and A. G. Green, 2004, Experimental design: Electrical resistivity data sets that provide optimal subsurface information: Geophysics, **69**, 120–139.

Wiese, T., S. A. Greenhalgh, and L. Marescot, 2009, DC sensitivity patterns for tilted transversely isotropic media: Near Surface Geophysics, **7**, no. 2, 125–139.

Zhou, B., M. Greenhalgh, and S. A. Greenhalgh, 2009, 2.5D/3D electrical resistivity modelling in anisotropic media using Gaussian quadrature grids: Geophysical Journal International, **176**, 63–80.

Zhou, B., and S. A. Greenhalgh, 1999, Explicit expressions and numerical computation of the Fréchet and second derivatives in 2.5D Helmholtz equation inversion: Geophysical Prospecting, **47**, 443–468.

Chapter 4: DC Resistivity Sensitivity Patterns for Tilted Transversely Isotropic Media

[1]Wiese T.C., [1,2]Greenhalgh S.A., [2]Marescot L.

1. Department of Physics, University of Adelaide, Australia
2. Institute of Geophysics, ETH Zürich, Switzerland

Near Surface Geophysics, 7; 125 – 139.

4.1 Statement of Contribution:

DC Resistivity Sensitivity Patterns for Tilted Transversely Isotropic Media
Near Surface Geophysics, 7; 125 – 139.

Conceptualization

This paper was jointly conceptualized by T. Wiese and S. Greenhalgh.

Realization

The results were developed by T. Wiese under the direction of S. Greenhalgh and L. Marescot. Code development and testing were conducted by T. Wiese. Analysis of results was done by T. Wiese with aid from all authors.

Documentation

T. Wiese was responsible for the bulk of the writing and all figure development. S. Greenhalgh improved the text vastly with edits, along with valuable contributions from L. Marescot.

The authors hereby certify that the statement of contribution is accurate and give permission for the inclusion of the paper in the thesis:

Wiese T.C., Greenhalgh S.A. & Marescot L., (2009). DC Resistivity sensitivity patterns for tilted transversely isotropic media.
Near Surface Geophysics, v. 7 (2), pp. 125 - 139.

Chapter 5: Comparison of DC Sensitivity Patterns for Anisotropic and Isotropic Media

[1,2]Greenhalgh S.A., [1]Wiese T.C., [2]Marescot L.

1. Department of Physics, University of Adelaide, Australia
2. Institute of Geophysics, ETH Zürich, Switzerland

Journal of Applied Geophysics, 70; 103 – 112.

5.1 Statement of Contribution

Comparison of DC Sensitivity Patterns for Anisotropic and Isotropic Media
Journal of Applied Geophysics, 70; 103 – 112.

Conceptualization

This paper was jointly conceptualized by T. Wiese and S. Greenhalgh.

Realization

T. Wiese produced the results under direction and advice of S. Greenhalgh. L. Marescot, S. Greenhalgh and T. Wiese were equally involved in analysis and interpretation of results.

Documentation

S. Greenhalgh wrote the paper, with the figures being produced by T. Wiese. L. Marescot was responsible for editing and improving both text and figures significantly. T. Wiese also edited text and made additions and improvements.

The authors hereby certify that the statement of contribution is accurate and give permission for the inclusion of the paper in the thesis:

NOTE:
Statements of authorship appear in the print copy of the thesis held in the University of Adelaide Library.

Greenhalgh S.A., Wiese T.C. & Marescot L., (2010). Comparison of DC sensitivity patterns for anisotropic and isotropic media.
Journal of Applied Geophysics, v. 70 (2), pp. 103 - 112.

Chapter 6: Resistivity inversion in 2D anisotropic media: numerical experiments

[1]Wiese T.C., [1,2]Greenhalgh S.A., [1]Zhou B.

1. Department of Physics, University of Adelaide, Australia
2. Institute of Geophysics, ETH Zürich, Switzerland

Geophysical Prospecting, revised version submitted February 2012.

6.1 Statement of Contribution

Resistivity inversion in 2D anisotropic media: numerical experiments
Geophysical Prospecting, submitted July 2011.

Conceptualization

The various research investigations in this paper were conceptualised by T. Wiese with the guidance of S. Greenhalgh.

Realization

B. Zhou provided the fundamental experimental forward modelling code which was adapted and improved by T. Wiese to result in the finalised inversion software. The sensitivity and inversion routines in this software were coded by T. Wiese with the guidance of B. Zhou. Results were produced by T. Wiese and analysed by T. Wiese with assistance from all authors.

Documentation

T. Wiese was responsible for writing the draft version of the paper. This initial effort was improved vastly with edits and additions from S. Greenhalgh. All figures were produced by T. Wiese. B. Zhou edited and improved the text and also provided advice on presentation of the figures.

The authors hereby certify that the statement of contribution is accurate and give permission for the inclusion of the paper in the thesis:

RESISTIVITY INVERSION IN 2D ANISOTROPIC MEDIA: NUMERICAL EXPERIMENTS

by

[1] **Timothy Wiese,** [1,2] **Stewart Greenhalgh and** [3] **Bing Zhou**

1. Department of Physics, University of Adelaide, Australia
2. Institute of Geophysics, ETH Zurich, Switzerland
3. School of Earth and Environmental Sciences, University of Adelaide, Australia

Submitted to *Geophysical Prospecting*, 2012

ABSTRACT

Many rocks and layered/fractured sequences have a clearly expressed electrical anisotropy although it is rare in practice to incorporate anisotropy into resistivity inversion. In this contribution we present a series of 2.5D synthetic inversion experiments for various electrode configurations and 2D anisotropic models. We examine and compare the image reconstructions obtained using the correct anisotropic inversion code and those obtained using the false but widely used isotropic assumption. Superior reconstruction in terms of reduced data misfit, true anomaly shape and position, and anisotropic background parameters were obtained when the correct anisotropic assumption was employed for medium to high coefficients of anisotropy. However, for low coefficient values the isotropic assumption produced better quality results. When an erroneous isotropic inversion is performed on medium to high level anisotropic data the images are dominated by patterns of banded artefacts and high data misfits.Various pole–pole, pole–dipole and dipole–dipole data sets were investigated and evaluated for the accuracy of the inversion result, the eigenspectra analysis of the pseudo Hessian matrix and the relative resolution plots. Inversion images were compared against the true model. We also present a data selection strategy based on high sensitivity measurements which drastically reduces the number of data to be inverted but still produces comparable results to that of the comprehensive data set. Inversion was carried out using transversely isotropic model parameters described in two different co-ordinate frames for the conductivity tensor viz. Cartesian versus natural or eigenframe. The Cartesian frame provided a more stable inversion product. This can be simply explained from inspection of the eigenspectra of the pseudo-Hessian matrix for the two model descriptions.

1. INTRODUCTION

Resistivity tomography is widely used as an effective underground exploration technique in a variety of near-surface applications, including mineral search, civil engineering site investigations, groundwater hydrology, and contaminant investigations (Butler, 2005; Rubin and Hubbard 2005; Reynolds, 2009). Imaging can be conducted either from the surface or between boreholes, or a combination approach. Nearly all of the published examples assume electrical isotropy of the ground. This may seem rather surprising given the compelling field and laboratory evidence that many rocks have a clearly expressed anisotropy (Maillet, 1947; Keller and Frischknecht, 1966; Parkomenko, 1967; Bhattacharya and Patra, 1967). The cause of this directional dependence in the resistivity can be microscopic in nature, for instance determined by intrinsic material properties such as platy mineral fabric or lineation e.g., clays. Anisotropy may also occur on a macroscopic scale whereby a series of layers or bands of dissimilar isotropic materials behave as a single, equivalent anisotropic unit. Layering, fracturing, jointing or rock cleavage can all produce this type of structural anisotropy. Typical values of the coefficient of anisotropy λ (square root of the ratio of maximum to minimum resistivity - see equation 4) for shale and sandstone interbeds are in the range 1.05 -1.15. Coal typically has a value between 1.7 and 2.6 due to cleating, while inter-bedded anhydrite and shale have reported values of 4.0 – 7.5. Even alluvium can have anisotropy factors of 1.02-1.1 (Hill, 1972; Asten, 1974).

A detailed discussion on how to detect anisotropy from surface DC resistivity measurements is beyond the scope of this paper, but may be found in the article by Greenhalgh *et al.,* (2010). It includes techniques such as azimuthal resistivity surveys (Watson and Barker, 1999; Busby, 2000), square electrode arrays (Habberjam, 1975; Matias, 2002) and tensor measurements (Caldwell and Bibby, 1998; Caldwell and Brown, 2005). The diagnosis is often improved if cross-hole resistivity data is available or if electric induction logging can be carried out in boreholes (Lu, Alumbaugh and Weiss, 2002).

There are four principal reasons why anisotropy is seldom incorporated into practical DC resistivity investigations: (1) the problem of electrical equivalence, which means that it is impossible to distinguish from scalar surface electrical measurements between horizontal layering and macro-anisotropy of the medium, (2) the Paradox of Anisotropy (Keller and Frischnecht, 1966), whereby the apparent resistivity is lower in the resistive across-strike direction and higher in the conductive in-strike direction, frustrating attempts by the geophysicist to recognise the counter-intuitive effects of anisotropy, (3) the geoelectric field is static in nature and limited in resolution capability, especially with increasing distance/depth distance from the electrodes, and (4) anisotropy means an increase in the number of parameters to be recovered from the data, for what is already an often seriously under-determined inverse problem.

By contrast, anisotropy is often incorporated into diffusive (AC) field magnetotelluric investigations (Reddy and Rankin, 1971; Loewenthal and Landisman, 1973; Dekker and Hastie, 1980; Everett and Constable, 1999; Linde and Pedersen, 2004; Wannamaker, 2005; Collins, Everett and Johnston, 2006) and electromagnetic (EM) induction surveying (Le Masne and Vasseur, 1981; Yu and Edwards, 1992; Slater, 1998; Yin and Fraser, 2004). A similar Paradox of Anisotropy occurs for EM but there are procedures to resolve it (Gianzero, 1999; Wang and Fang, 2001; Weiss and Newman, 2002; Al-Garnt and Everett, 2003). A list of references on numerical modelling procedures for EM in the presence of anisotropy is given in the paper by Yin and Fraser, (2004).

The literature on DC resistivity modelling incorporating anisotropy is comparatively rather sparse. The semi-analytic forward solutions for half-spaces, vertical contacts, layered media

and prismatic bodies in an anisotropic background are reviewed by Greenhalgh *et al.,* (2009a). For general heterogeneous, anisotropic media, three approaches have been used: the finite difference method (LaBreque *et al.* 2004), the finite element method (Pain *et al*., 2003; Li and Spitzer, 2005) and the Gaussian quadrature grid method (Zhou *et al.,* 2009).

There are just a handful of published papers on anisotropic resistivity inversion. LaBreque *et al.,* (2004) incorporated anisotropy into the finite difference modelling formulation of Dey and Morrison (1979), but assumed that the axes of the conductivity ellipsoid were aligned with the co-ordinate directions, greatly simplifying the problem. They use an Occam-style inversion scheme with an objective function including regularisation operators to control the smoothness and the magnitude of anisotropy permitted. Pain *et al.,* (2003) used a Levenberg-Marquardt type iterative preconditioned conjugate gradient inverse solver and a finite element forward solver. Their major contribution was to formulate and incorporate penalty functions for anisotropy and structure within the inversion objective function. Simple synthetic models with pole-pole array data sets were used to validate the inversion routine and highlight the non-linear nature of the problem. Suites of inversions were run to select the optimal penalty functions to minimise data residuals. Herwanger *et al.,* (2004) extended the analysis by presenting a case study in which cross-hole resistivity and seismic methods were used to independently recover anisotropic model parameters. A good agreement of spatial structures with high anisotropy was found between the two techniques. The other notable inversion papers are those of Kim *et al.,* (2006) and Yi *et al.,* (2011), who present a case study in which 2D and 3D cross-hole tomography was able to delineate cavities with isotropic properties situated in a highly anisotropic biotite-gneiss subsurface. The orientations of the anisotropy axes were assumed to be in-line with the measurement (Cartesian) frame, an often questionable assumption. Anisotropy penalty terms were added to the objective function along with spatially varying Lagrange multipliers which increased stability and resolution in the inversion process. Unfortunately, precise details on the forward and sensitivity calculations are not provided for this case study in either paper.

A key component of any local search minimisation style inversion strategy is the ability to compute the Fréchet derivatives or sensitivity functions. Recently, Greenhalgh *et al.,* (2009b) presented a general adjoint method for computing the DC resistivity sensitivity kernels in 2.5D and 3D anisotropic heterogeneous media. In a companion paper (Greenhalgh *et al.,* 2009a) they give explicit expressions for the various sensitivity functions in homogeneous anisotropic media, and in other contributions (Wiese, Greenhalgh and Marescot, 2009; Greenhalgh *et al.*, 2010) the anisotropic sensitivities are computed for various electrode arrays and compared with the isotropic sensitivities, showing the dangers of making an isotropic assumption when the ground is anisotropic.

In this paper we go the next step and perform a series of 2.5D inversion experiments for point electrode sources in 2D synthetic anisotropic models. We examine image recovery for isotropic blocks (inclusions) within an anisotropic background, as well as anisotropic blocks within an isotropic background, and see what is possible under favourable 3-sided recording conditions (i.e., combination cross-hole/ borehole to surface). We also invert the synthetic data by falsely assuming medium isotropy everywhere, and contrast these distorted images with the proper anisotropic solutions. We investigate the effect of changes in the dip angle of the plane of isotropy and changes in the degree of anisotropy. Various pole–pole, pole–dipole and dipole–dipole data sets are investigated and evaluated from the accuracy of the inversion result, by eigenspectra analysis of the pseudo Hessian matrix and the relative resolution plots. We also present a data selection strategy based on high sensitivity measurements which produces inversion products comparable to that of comprehensive data sets. Reconstruction was attempted on equivalent anisotropic models with model parameters described in different co-ordinate frames (Cartesian and the principal axes or eigenframe).

2. BACKGROUND THEORY

2.1. 2D TI Media

In its most general form, electrical anisotropy is described by a symmetric, second rank conductivity tensor with 6 independent components (Greenhalgh *et al*., 2009b). In this paper we consider a more specific but prevalent class of anisotropy, that of a 2D tilted transversely isotropic (TTI) medium involving just 3 independent components of the tensor (see Figure 1a). In this model resistivity is constant for all directions within a specific plane termed the plane of isotropy (e.g. plane of stratification or foliation) but different in all other directions outside that plane. In optics, when dealing with the dielectric or refractive index tensor, this particular class of anisotropy is referred to as uniaxial and many minerals conform to it.

Here we will consider 2.5D modelling which entails a point source of current and a 2D model in which the resistivity parameters do not change in the y - or strike direction. The TTI model properties may be described with reference to either a geographic (measurement) co-ordinate frame involving the tensor elements $\rho_{XX}, \rho_{XZ}, \rho_{ZZ}$ or a principal axis frame (or eigenaxis frame) involving the components ρ_L, ρ_T, θ_0. Here ρ_L is the longitudinal resistivity, ρ_T is the transverse resistivity and θ_0 is the angle of the symmetry axis relative to the vertical i.e. the transverse (uniaxial) direction. The principal axis frame is physically meaningful since the eigenvectors are aligned with the natural rock frame. This is illustrated schematically in Figure 1b. The semi-major and minor axes of the resistivity ellipse correspond to the two eigenvectors, and their lengths *a* and *b* are related to the eigenvalues or principal values according to the relations:

$$a = \sqrt{\rho_T} \text{ and } b = \sqrt{\rho_L} \tag{1}$$

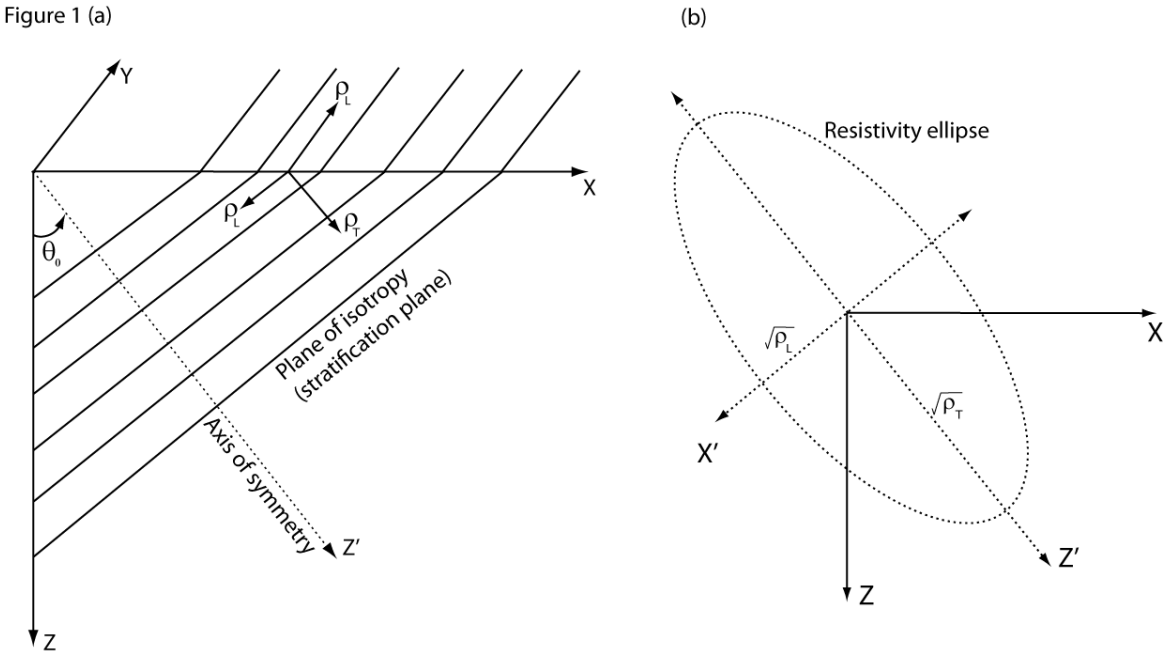

Figure 1: a) Simplified diagram of anisotropic 2D TTI media, showing axis of symmetry and principal resistivities. b) The resistivity ellipse shown in relation to the geographic co-ordinate frame (X, Z), and the principal axis frame (or natural rock frame) (X', Z'). The lengths of the semi major axes are equal to the inverse square roots of the principal resistivities (or eigenvalues of the 2x2 resistivity matrix). The directions of the principal axes are the corresponding eigenvectors.

The third eigenvector is in the y or medium- invariant direction. The two co-ordinate systems are related in terms of a rotation matrix derived in Greenhalgh *et al.*, (2009b):

$$\begin{pmatrix} \rho_{xx} \\ \rho_{yy} \\ \rho_{xz} \\ \rho_{zz} \end{pmatrix} = \begin{pmatrix} \rho_L \cos^2\theta_0 + \rho_T \sin^2\theta_0 \\ \rho_L \\ 0.5(-\rho_L + \rho_T)\sin 2\theta_0 \\ \rho_L \sin^2\theta_0 + \rho_T \cos^2\theta_0 \end{pmatrix} \tag{2}$$

The below formulae may be used to transform from $\rho_{XX}, \rho_{XZ}, \rho_{ZZ}$ to ρ_L, ρ_T, θ_0 :

$$\begin{aligned} \theta_0 &= \tan^{-1}\left(\frac{-2\rho_{xz}}{\rho_{xx} - \rho_{zz}}\right) \\ \rho_L &= \frac{\cos^2\theta_0\rho_{xx} - \sin^2\theta_0\rho_{zz}}{\cos 2\theta_0} \\ \rho_T &= \frac{-\sin^2\theta_0\rho_{xx} + \cos^2\theta_0\rho_{zz}}{\cos 2\theta_0} \end{aligned} \tag{3}$$

By rearranging the orthogonal anisotropic resistivity model parameters (ρ_L and ρ_T) we may introduce an alternative form of description for TTI media viz., the mean resistivity ρ_m and the coefficient of anisotropy λ, given by:

$$\rho_m = \sqrt{\rho_L \rho_T}\,, \qquad \lambda = \sqrt{\rho_T / \rho_L} \tag{4}$$

The (ρ_M, λ) description is particularly insightful when gauging or comparing the magnitude of electrical anisotropy (λ) in material media. The quantity ρ_m is the geometric mean of the longitudinal and transverse resistivities. It is equal to the apparent resistivity:

$$\rho_a = \frac{KU}{I} \tag{5}$$

measured on the ground surface in a direction parallel to the stratification in a VTI medium, having a vertical axis of symmetry (e.g., horizontal beds) or in the strike direction for a HTI medium having a horizontal axis of symmetry (e.g., vertically dipping beds). In equation (5) U is the potential difference, I is the current strength and K is the geometric factor for the electrode array. The Paradox of Anisotropy (Keller and Frischknecht, 1966) is that the apparent resistivity measured transverse to the layering in a HTI medium is actually equal to the longitudinal resistivity and not the transverse resistivity. In its most general form for uniaxial systems, the apparent resistivity measured in any one of the 3 principal directions will be equal to the geometric mean of the true resistivities in the other two orthogonal directions. For isotropic media, $\rho_m = \rho_L = \rho_T$, and λ= 1.

Many papers work with the conductivity tensor $\boldsymbol{\sigma}$ rather than the resistivity tensor $\boldsymbol{\rho}$. They are simple inverses of each other such that $\boldsymbol{\rho\sigma} = \mathbf{I}$, where $\mathbf{I}$ is the identity matrix. In terms of the principal values in the rotated co-ordinate frame:

$$\sigma_L = 1/\rho_L,\ \sigma_T = 1/\rho_T,\ \sigma_{yy} = \sigma_L = 1/\rho_L \tag{6}$$

The Cartesian element components $\sigma_{xx}, \sigma_{zz}, \sigma_{yy}, \sigma_{xz}$ obey identical equations to the resistivity components of equation (1) if we replace the ρ_L and ρ_T terms by the principal conductivities σ_L and σ_T, respectively.

2.2. GQG Forward Modelling

An essential requirement of any inversion scheme is a forward solver to compute the theoretical model response. For a point source of current in a 2D medium, the governing equations for this so-called 2.5D problem may be written as (Zhou *et al.,* 2009):

$$\begin{cases} \nabla \cdot (\boldsymbol{\sigma} \cdot \nabla \tilde{G}) + k_y^2 \sigma_{yy} \tilde{G} = -\dfrac{1}{2}\delta(r - r_s), & r = (x, z) \in \Omega, \\ (\boldsymbol{\sigma} \nabla \tilde{G}) \cdot \mathbf{n} + \nu \tilde{G} = 0, & r = (x, z) \in \Gamma, \end{cases} \tag{7}$$

Here $\boldsymbol{\sigma}$ is the Cartesian symmetric conductivity matrix described above, **n** is the unit normal vector to the boundary Γ, ν is a known function of the spatial coordinates and the conductivity and specifies the mixed boundary condition, r_s is the current point-source location, k_y is the wave-number or spatial Fourier transform variable corresponding to the y-direction. The quantity $\tilde{G}$ is the spatially Fourier transformed Green's function, which is equal to the impedance (or resistance) *U/I*. It is simply the voltage response for a unit current injection.

Zhou *et al.,* (2009) presented the Gaussian quadrature grid numerical scheme for 2.5D DC resistivity modelling in which the variational principle was applied to (7) to reformulate the problem in functional (Ψ) form:

$$\begin{cases} \min\{\Psi(\tilde{G})\} \\ \Psi(\tilde{G}) = \dfrac{1}{2}\displaystyle\int_{\Omega} [\nabla \tilde{G} \cdot \boldsymbol{\sigma} \cdot \nabla \tilde{G} + \sigma_{yy} k_y^2 \tilde{G}^2] d\Omega + \int_{\Gamma} \nu \tilde{G}^2 d\Gamma - \tilde{G}_s \end{cases} \tag{8}$$

Here $\tilde{G}_S$ is the value of the Green's function at the source position. The model is parameterised into sub-domains which are populated with nodes distributed at Gaussian quadrature abscissae points and are assigned weights corresponding to their positions (see Figure 2).

The abscissa number per dimension in the sub-domain is called the Gaussian quadrature order. According to Gaussian quadrature theory the accuracy of integration depends on the number of abscissae and converges to a high accuracy with increasing Gaussian order. The key step is to calculate the values of the functional at the Gaussian quadrature abscissae, which involves sampling the model parameters, the Green's function and its gradient based on the grid. The forward modelling reduces to solving a linear equation system. The main advantages of the method are its ability to deal with a complex geological model involving anisotropy and an arbitrary surface topography, whilst retaining the computational advantages of the spectral element method, yet a complex mesh generator is not needed as in the FEM (Greenhalgh, 2008).

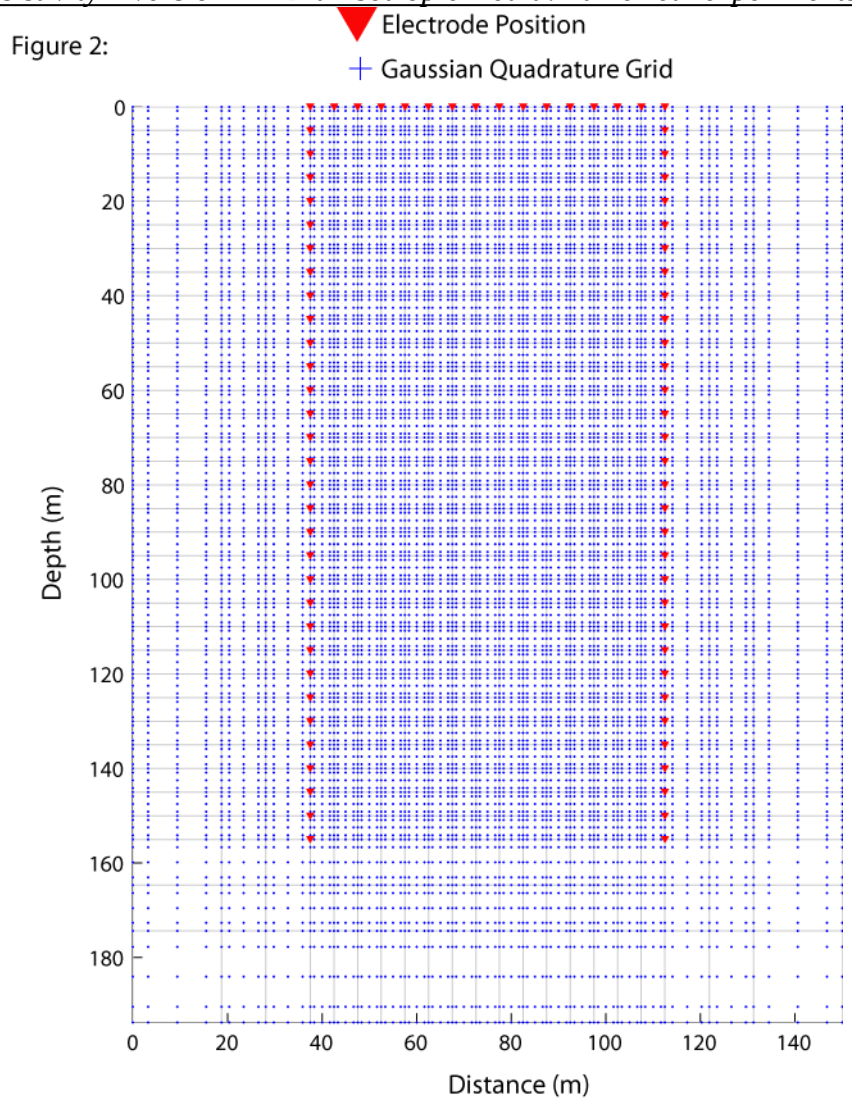

Figure 2: Blue crosses indicate the Gaussian quadrature grid of Gaussian order 5 used for forward modelling. The position of the 64 electrodes in the surface – borehole array is shown by red dots.

2.3. Fréchet Derivatives

The sensitivity (Fréchet derivative) gives the change in measured potential (or apparent resistivity) due to a perturbation of the model parameter in a particular model. It is an essential component of any local search minimisation type inversion scheme (Zhou and Green 2006). In a recent paper (Greenhalgh *et al.*, 2009b) we developed a new formulation for the anisotropic sensitivities for both the 3D and the 2.5D problems. For the latter, the result can be stated as:

$$\frac{\partial G^s(r_p)}{\partial m_\upsilon} = -F_c^{-1}\left\{\left[\nabla\tilde{G}^s(r).\frac{\partial \boldsymbol{\sigma}}{\partial m_\upsilon}\right].\nabla\tilde{G}^p(r) + k_y^2\frac{\partial \sigma_{yy}}{\partial m_\upsilon}\tilde{G}^s(r)\tilde{G}^p(r)\right\} \qquad (9)$$

This equation shows that sensitivity can be computed in terms of the source $\tilde{G}^s$ (current electrode *s*) and adjoint source $\tilde{G}^p$ (potential electrode *p*) Green's functions and their gradients, as well as the derivatives of the conductivity tensor with respect to the principal model values. Here F_c^{-1} is the inverse Fourier cosine transform with respect to wavenumber.

The model parameter m_v may assume any of the anisotropic model parameters in either the Cartesian or eigen frames, which for the 2.5D TTI problem under consideration comprises ρ_l, ρ_t, θ_0 or $\rho_{xx}, \rho_{xz}, \rho_{zz}$, (Note that $\rho_{yy} = \rho_l$). Explicit expressions for the derivative term $\partial\boldsymbol{\sigma} / \partial m_v$ may be found in Greenhalgh *et al.*, (2009b). A comprehensive study into the various anisotropic sensitivity functions in homogeneous anisotropic media for various arrays is given in Wiese *et al.,* (2009). In a companion paper (Greenhalgh *et al.,* 2010), these sensitivities are compared with those for an isotropic medium and the prominent differences in both the sign and magnitude of the sensitivities highlighted, showing the dangers of using an isotropic assumption when inverting anisotropic data.

Some authors express the isotropic sensitivities in a slightly different form than that used above (viz., $\partial G / \partial \sigma$), involving apparent resistivity ρ_a, or its logarithm $\log \rho_a$, or even in terms of resistance *R* e.g. $\partial \rho_a / \partial \rho, \partial \log(\rho_a) / \partial \log(\rho), \partial R / \partial \rho.$ Conversion from one form to another is simple using implicit differentiation and the basic linking equations:

$$U = IG, \qquad \rho_a = KU / I, \qquad \boldsymbol{\sigma} = \boldsymbol{\rho}^{-1} \tag{10}$$

The Jacobian matrix ($\mathbf{J} = \partial \mathbf{d} / \partial \mathbf{m},$ where $\mathbf{d} = U$ or ρ_a) is traditionally constructed with the rows related to the different measurement configurations and the columns corresponding to each model cell. The elements of the matrix are sensitivities, which are dependent on the electrode configuration for the data point and the location of the model cell. In geo-electrics it is well documented that sensitivity decreases with distance from the electrodes because of the DC nature of the problem. Current lines are not straight, even in a homogeneous, isotropic medium.

2.4. Inversion Approach

2.4.1. Gauss-Newton Solution

Rather than building complicated smoothing and anisotropy penalty functions into the objective function, as has been previously done (e.g. Pain *et al.*, 2004), here we concentrate on quantifying the effects of using an isotropic assumption to invert anisotropic data Comparisons between a (correct) anisotropic inversion with the isotropic reconstruction can only be done if the same inversion routine with similar regularisation is used for both. For this reason the inversion scheme is chosen to be the well understood, widely used and easily implemented Gauss-Newton approach.

Central to any linearized least squares (or Gauss-Newton/Levenberg-Marquardt) inversion scheme is the forward operator (*F)* (GQG, see section 2.2) used to calculate the synthetic or predicted data ($\mathbf{d}^{pred}$) which can be in the form of voltage or apparent resistivity for a given model (**m**):

$$\mathbf{d}^{pred} = F(\mathbf{m}) \tag{11}$$

The inverse operator (F^{-1}) then seeks an estimate of model parameters ($\boldsymbol{m}^{est}$) that best fit the observed data ($\mathbf{d}^{obs}$):

$$\mathbf{m}^{est} = F^{-1}(\mathbf{d}^{obs} - \mathbf{d}^{pred}) \tag{12}$$

The inverse operator may be written as an optimisation (minimisation) of an objective function (ϕ):

$$\min\{\phi(\mathbf{m})\} = \min\{\phi_d(\mathbf{m}) + \gamma\phi_m(\mathbf{m})\} \quad (13)$$

γ is the damping factor that determines the trade off between the data fit and the a-priori knowledge on the model. The latter can be included through structural constraints, closeness to a preferred model or smoothing. Selection of the damping factor is discussed in section 2.4.2.The quantities ϕ_d and ϕ_m are the data and model misfit functions (or norms), respectively

$$\phi_d(\mathbf{m}) = \|W_d(\mathbf{d}^{obs} - \mathbf{d}(\mathbf{m}))\|^2 \quad (14)$$

$$\phi_m = \|W_m\,(\mathbf{m} - \mathbf{m_0})\|^2 \quad (15)$$

Where $\mathbf{m}_0$ is the starting or preferred model, and W_m and W_d are the model and data weighting matrices, respectively, for which various choices are available depending on the definition of the solution (Greenhalgh *et al.*, 2006).

By calculating the derivatives of the data and model misfit functions we may derive the stationary point equation (Greenhalgh *et al.*, 2006):

$$\gamma(\mathbf{m} - \mathbf{m}_0) = \left(\frac{\partial \mathbf{d}^{pred}}{\partial \mathbf{m}}\right)^T [\mathbf{d}^{obs} - \mathbf{d}^{pred}(\mathbf{m})] \quad (16)$$

The stationary point equation may then be solved by an iteratively linearized scheme:

$$\mathbf{d}^{pred}(\mathbf{m}_{k+1}) \approx d^{pred}(\mathbf{m}_k) + \left(\frac{\partial \mathbf{d}^{pred}}{\partial \mathbf{m}}\right)_k^T [\mathbf{m}_{k+1} - \mathbf{m}_k)] \quad (17)$$

where $\left(\frac{\partial \mathbf{d}^{pred}}{\partial \mathbf{m}}\right)$ is the Jacobian matrix (***J***). The inverse operator can be written in Gauss-Newton form as:

$$\mathbf{m}_{k+1}^{est} = (\mathbf{J}^T\mathbf{J} + \gamma\mathbf{C}_m^{-1})^{-1}\mathbf{J}^T\left[\ (\mathbf{d}^{obs} - \mathbf{d}^{pred}(\mathbf{m}_k)) + \mathbf{J}\mathbf{m}_k\ \right] \quad (18)$$

Here $\mathbf{C_m^{-1}}$ is the a-priori model covariance matrix which allows regularization constraints such as smoothness (roughness), or minimum variation from some reference model. The resulting rectangular system can be solved by a conjugate gradient scheme (Greenhalgh *et al.*, 2006).

2.4.2. Program Description

The inverse problem requires that regularisation be imposed to stabilise the solution and reduce the inherent non-uniqueness. It also helps to ensure that the inversion does not fall into a local minima but rather reaches the global minimum of the objective function.

The damping factor choice specifies the trade-off between the pre-conceived ideas of the true model (a-priori knowledge) and data fit. Smoothing was included through a finite difference operator that allowed variable weighting so that smoothness could be varied in different directions (deGroot-Hedlin and Constable, 1990).

Since the experiments conducted were synthetic in nature the true model was known, making it straightforward to visually gauge the success of an inversion. A suite of inversions were carried out with various levels of damping. The inversions having the highest damping factor

and which still converged to within numerical noise levels (< 2%) were selected for presentation. This way we neither over-smooth nor introduce false detail into the image. These inversions were the most optimal reconstructions of the true model with the least amount of artefacts. The inversion stopping criteria were that the desired data misfit of < 2% was reached (which we deemed to be below numerical noise inherent in our program), the number of iterations exceeded 20 or the difference between successive iterations produced an RMS difference of less than 0.5%. Convergence was calculated as the percentage ratio of the initial data misfit over the data misfit of the j^{th} iteration. A flow chart showing the main elements of the inversion approach is given in Figure 3.

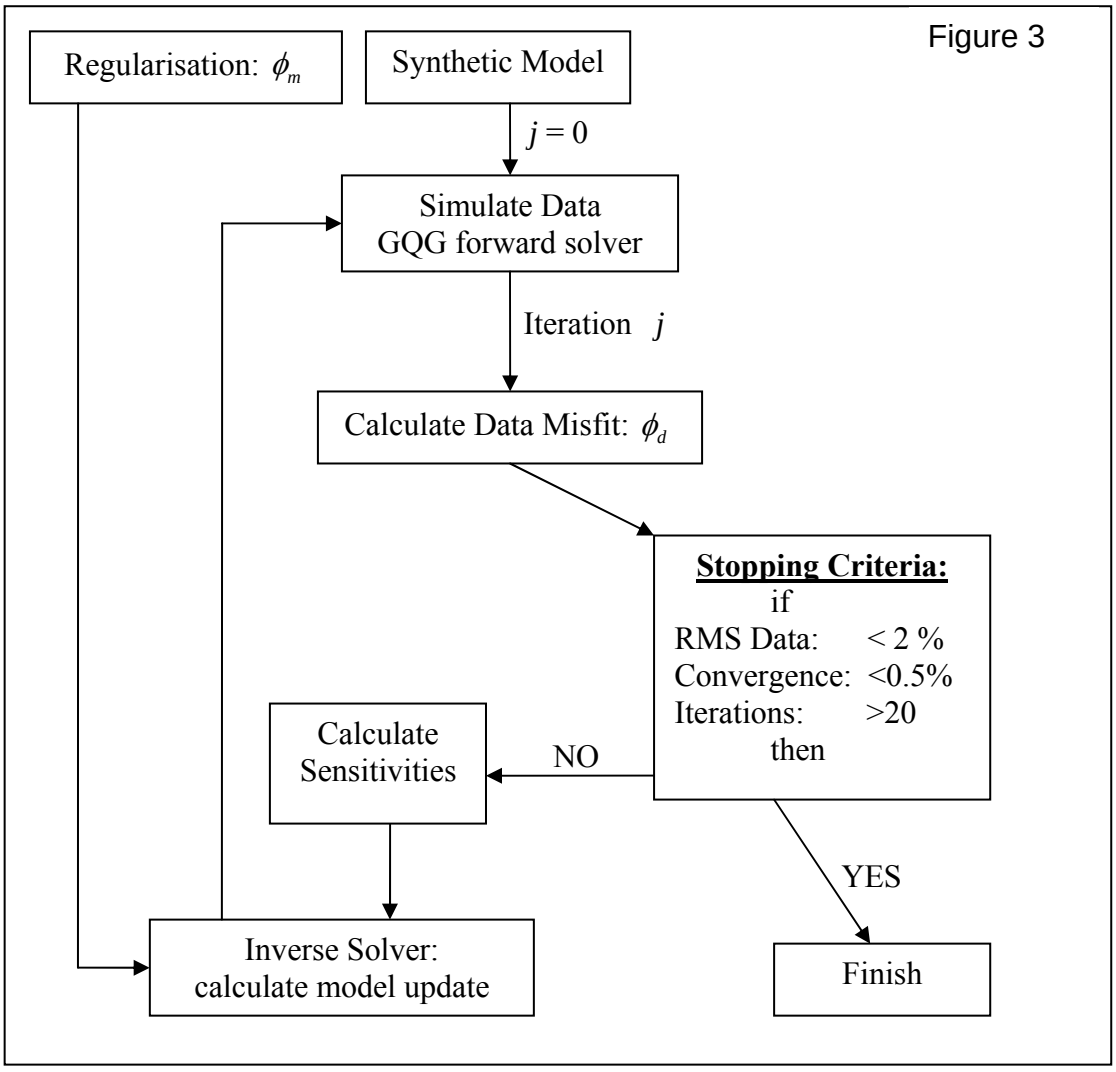

Figure 3: The inversion program flow chart shows the iterative methodology and convergence stopping criteria.

2.4.3. Information content and resolution

The optimisation of geophysical experimental design is an area of active and current research (Maurer and Boerner, 1998; Stummer, Maurer and Green, 2004; Loke, Wilkinson and Chambers, 2010; Maurer, Curtis and Boerner, 2010; Blome, Maurer and Green, 2011), but compared to numerical forward modelling and inversion theory, this field of knowledge is far less developed.

Inversion algorithms are largely based on linearized theory (Menke, 1984) and as such methods for quantifying the benefits of a particular survey exist. The quality of an inversion

result of a truly linear forward model can be appraised by examining the model resolution matrix formally defined as:

$$\mathbf{R} = (\mathbf{J}^T\mathbf{J} + \gamma\mathbf{C}_m^{-1})^{-1}\mathbf{J}^T\mathbf{J} \quad (19)$$

It relates the estimated model parameters to the true model parameters ($\mathbf{m}^{true}$) through the equation:

$$\mathbf{m}^{est} \approx \mathbf{R}\mathbf{m}^{true} \quad (20)$$

Of particular interest are the diagonal elements of ***R***. Values close to zero indicate poorly resolved model parameters, whereas values close to one indicate well resolved model parameters.

The choice of a survey layout, configuration type and selection of data governs the structure of the Jacobian **J**, which is the foundation of the approximate Hessian matrix $\mathbf{H} = \mathbf{J}^T\mathbf{J}$ .The reliability of the model update depends primarily on our ability to invert the matrix ($\mathbf{J}^T\mathbf{J} + \mathbf{C}_m^{-1}$). Without the regularization (damping and smoothing) this matrix would likely be singular. The eigenvalue spectrum of the approximate Hessian matrix is related to the null-space or unresolvable model space of a particular data set. This allows comparison of spectra from various experimental designs as a quantitative method to rate specific information content and resolving ability.

3. SYNTHETIC INVERSION EXPERIMENT METHODOLOGY

3.1. Experimental setup

The focus of the experiments was to determine the effect of the actual assumptions (anisotropy or isotropy) used in the forward solver and sensitivity calculations for the same inversion routine on a number of different anisotropic models. Therefore, most experiments were conducted with a three-sided geometry (combined crosshole and borehole-to-surface) chosen because it delivered the most optimal possibility for data collection and model coverage. Such configurations are becoming more popular in field surveying. This type of electrode placement allows one to overcome the ambiguity from the Principle of Equivalence (Keller and Frischknech, 1966) associated with pure surface measurements when the axis of symmetry is vertical.
The experimental setup consisted of 78 electrodes, 32 in each borehole and the remaining 14 positioned along the surface. The positions of electrodes are shown by triangles in Figure 2. Electrodes are placed at 5 m spacing. The two boreholes extend to a depth of 155 m and are spaced 65 m apart.

3.2 Forward and inverse parameterization

The model domain was discretized for inversion with a regular grid of rectangular model cells of size 5 x 5 metres. Inversion cell size was chosen to be the electrode spacing so as to limit the total number of model parameters because of the already increased number of parameters which must be considered when anisotropy is incorporated. There were 465 (31 by 15) inversion model cells for each parameter. The forward modelling was conducted with the same sub-domain parameterization as the inversion cells. The forward calculation used a Gaussian nodal order of five for each sub-domain along with 20 wave-numbers. This gave rise to 6,897 nodes in the forward GQG grid ($\left[(N_{X1}-1).(N_{ord}-1)+1\right].\left[(N_{Z1}-1).(N_{ord}-1)+1\right]$

where N_{X1}=31, N_{Z1}=15, N_{ord}=5). This was deemed to be a good compromise between accuracy and computational efficiency (Greenhalgh, 2008; Zhou *et al.,* 2009).

To provide a comparison with the optimal three-sided crosshole experiment, and to show what is possible with surface measurements alone in the presence of anisotropy, a surface electrode array numerical experiment was also conducted. Sixty one electrodes were placed along the surface at a spacing of 5 m. The model (inner) domain extended from x = 0 to x = 300 m and in depth to z = 60 metres. The same forward and inversion discretization was used as in the 3 sided experiments, i.e. 720 inversion cells of size 5 by 5 metres with 720 forward sub-domains and 10,845 Gaussian nodes (Gaussian nodal order of 5).

3.3. Electrode Array Types

The three most widely used measurement configurations in cross-hole or surface-to-borehole geo-electric surveying are the pole-pole, pole-dipole and dipole – dipole arrays involving 2, 3 and 4 mobile electrodes, respectively. For pole-dipole and pole-pole the remote electrodes are located at a considerable distance away from the survey area so that there is no effective contribution from the current sink. This section of the paper explains the basis and selection for the comprehensive data sets used. Secondly, we explain a method for selection of the highest sensitivity data sets obtained from calculation of the Jacobian for comprehensive data sets.

A comprehensive data set (Xu and Noel, 1993) consists of every possible non-reciprocal measurement, whereas the complete data set is composed of all linearly independent measurements. It is possible to reconstruct the comprehensive data set from the complete set (Blome, 2009; Lehmann, 1995). The pole-pole comprehensive and complete data sets are equivalent and consist of 3003 recording configurations (78*77 / 2) for a 78 electrode surface to cross-hole experiment.

Zhou and Greenhalgh (2000) conducted a thorough investigation into the sensitivity of various cross-hole electrode configurations, finding that sensitivity was improved along the midpoint region of the boreholes for configurations such as the bipole – bipole (AM-BN) in which current source (A) and sinks (B) and potential electrodes (M, N) are in different boreholes, i.e. borehole 1: A, M; borehole 2: B, N. This array also produces relatively large signals. Pole-dipole arrays were found to produce good results, however configurations such as A-MN and MN-A are susceptible to noise due to low potential readings. The same is true for the 4-point configuration AB-MN and even though it offers improved resolution, it is at the expense of noise capture, especially due to the borehole fluid effect as recently investigated by Doetsch *et al.,* (2010).

It has been commonplace for some time in other geophysical techniques (e.g. seismic) to collect vast data sets. In geoelectrics it only became feasible in recent times to record massive data sets efficiently; currently a 64 channel resistivity system exists having capacity to collect such sets (Zhe, Greenhalgh and Marescot, 2007), and a 120 channel parallel recording system has recently been described by Blome *et al.,* (2011). This, combined with advances in computer memory and parallel processing techniques, could make inversion with comprehensive data sets possible in the future. But currently the massive amount of data involved in comprehensive pole-dipole and dipole-dipole data sets for even 78 electrodes is usually prohibitive for inversion because of time and computer memory constraints. To reduce the computational burden, it is normal practice to discard data points corresponding to high geometric factors *K*, which often correspond to low signal levels and therefore likely to be contaminated by noise. To illustrate the point, by eliminating all data having geometric factors $K>500$, a comprehensive pole-dipole data set of 78 electrodes still has ~76,000 data.

This is still a large amount of data to invert. For the same number of electrodes but in a 4-point comprehensive AM-BN (bipole-bipole) configuration, eliminating data with $K > 500$) results in a set of>500,000 data points.

3.4. Selecting the High Sensitivity Configurations

From examination of the Jacobian matrix for the comprehensive data sets, there exists a large subset of data that has extremely small sensitivity magnitude. The motivation of saving computer memory and run time resources directs us to investigate the effect of discarding low sensitivity data from comprehensive data sets and working with a reduced (filtered or selected) version. Such an approach was recently advocated by Athanasiou *et al.,* (2009). In earlier optimised experimental design strategies described by Stummer *et al.,* (2002) and Wilkinson *et al.,* (2006), configurations were progressively selected in accordance with linear independence or contributing most towards improving model resolution. The latter approach entails having to sequentially compute the model resolution matrix for each electrode configuration added to the set, and is very computationally intensive. By contrast, our sensitivity selection strategy is far less demanding than that based on incremental improvements to resolution, and seems adequate for the purpose.

An initial choice must be made for the model used to calculate the Jacobian. This is an arbitrary choice and may include any a-priori knowledge. We chose an isotropic model having $\rho_L = \rho_T = 500$ Ohm m because this is the starting model given for our inversions.

The method of filtering (or selecting entries from) the Jacobian was, firstly, to split the matrix into separate model parameters: ρ_L and ρ_T. The separate matrices (of dimension number of electrode configurations times the number of model cells) were then sorted along the model cell column in order of increasing sensitivity magnitude. Data may then be selected from each model cell column subject to either the absolute magnitude of the sensitivity or the number of data to include per model cell. Non-unique (dependent) data points are eliminated. A secondary beneficial outcome of the filtering process originates from prior knowledge of resolution patterns. Regions of low resolution model cells such as at the centre section of the boreholes can be allotted increasing numbers of selected high magnitude sensitivity data. The data inclusion method we used for our selected (filtered) data set was to take progressively increasing amounts of data for model cell columns as one moved from the boreholes towards the central column of cells. This is illustrated diagrammatically in Figure 4.

With the filtering/selection strategy used, the comprehensive pole-dipole data set of 77,000 measurements is reduced to 8,036 data points. The corresponding dipole-dipole comprehensive set of 549,000 configurations is reduced to 159,000 data points.

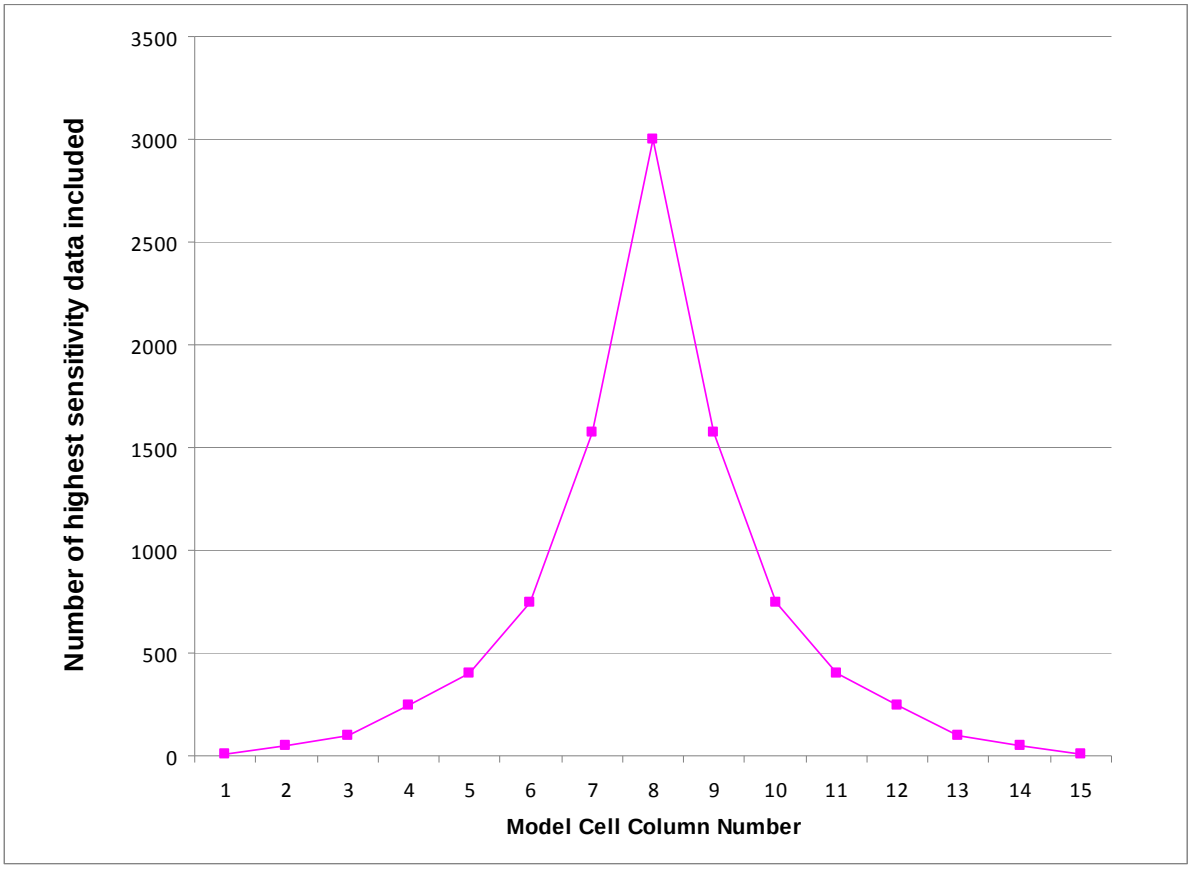

Figure 4: A representative graph of the data selection strategy that filters out ineffective low sensitivity data by sorting and selecting high sensitivity data. The x-axis represents the model cell column number (numbers 1 and 15 define the edge of the model / borehole). Increasing amounts of data are included towards the model cell column 8 which represents the lowest resolution along the central axis between the boreholes.

3.4. Types of Models

Three types of anisotropic model were investigated: firstly, an anisotropic background (TTI) having an embedded isotropic block anomaly. This type of model could simulate the geological situation of tilted shale or fractured limestone as the background rock, and an igneous inclusion or a pure water or air filled cavity causing the high resistivity anomaly. The second type of model is the reverse of the first type, involving an isotropic background with an anisotropic inclusion. This type of model could be representative of sandstone with enclosed clay or jointed ore body inclusion. The third model involves a layered anisotropic sequence that could simulate volcanic flows or metamorphic units of dissimilar dip.
The anisotropic model parameters allow for the possibility of changing the magnitude (coefficient) of anisotropy and/or the orientation of the axis of symmetry.

4. RESULTS

4.1 Anisotropic Background with an Isotropic Block Inclusion

The models used to create the synthetic data sets in this section consisted of an anisotropic background with a rectangular high resistivity isotropic target (1250 Ω m) centred between the boreholes. This section of the paper focuses on the effects of inversion reconstructions for variations in the orientation of the plane of isotropy (i.e. the θ_0 angle) and the magnitude of anisotropy (λ).

For this preliminary experiment the comprehensive pole-pole data set (3003 data points) was employed for two reasons. Firstly, this basis of measurements contains all possible linearly independent subsurface information, and secondly, the relatively small data set minimised the computational time required.

Figure 5 exhibits the inversion results for a set of true models in which the axis of symmetry angle θ_0 has three distinct values of 0, 45°, and 90°, as shown in the top, middle and bottom rows, respectively. This is physically equivalent to the orientation of the plane of isotropy (stratification or foliation) being horizontal, dipping and vertical. The coefficient of anisotropy is fixed at $\lambda = 1.22$ (ρ_L = 400 Ω m, ρ_T = 600 Ω m). The starting resistivity given for the inversion was a homogeneous and isotropic model having $\rho_L = \rho_T$ = 490 Ω m, which is equal to the geometric mean resistivity ρ_m. The isotropic nature of the starting model ensured that the anisotropic and isotropic assumption- based inversions could be made as nearly equivalent as possible, at least from the initial model viewpoint.

The left and middle columns of Figure 5 represent the inversion results for ρ_L and ρ_T produced with the correct anisotropic assumption for forward modelling and sensitivity calculations. The right hand side column gives the corresponding inversion result for the scalar resistivity ρ produced with the widely used isotropic assumption. The ρ_L and ρ_T images show accurate reconstruction of the anisotropic nature of the true background resistivity for all angles of the plane of isotropy. It can be seen that for all θ_0 values the positions of the true high resistivity isotropic embedded anomaly (outlined by the black square) are well resolved for both ρ_L and ρ_T images. An underestimate of the true high resistivity anomaly is noticeable in the ρ_L background; however, the contrast between the background and the reconstructed anomaly is equal to that of the ρ_T images. The reconstructed target anomalies were somewhat smeared over the borders of the true known geometry, although importantly they were centred in the correct position. This smearing is a product of the inversion scheme which we made with basic functionality. More complicated inversion objective functions exist that could likely improve the results, however these were not included so as to not deflect from the main objectives of the experiment.

The images obtained with the incorrect isotropic assumption (right hand column Figure 5) show a noticeable banding effect which follows a parallel orientation to the plane of isotropy for each of the different values (0, 45°, 90°). The data misfits obtained by the set of inversions using the isotropic assumption were more than eight times higher than those produced with the anisotropic assumption, which were deemed to be within the numerical noise level (1~2 %). The higher RMS values are of course a result of the banded artefacts. The source of the banding is the difference of sign in regions of the subsurface for isotropic Fréchet derivatives in anisotropic media. This has been described in Wiese *et al.,* (2009) and quantified in Greenhalgh *et al.,* (2010).

Figure 5

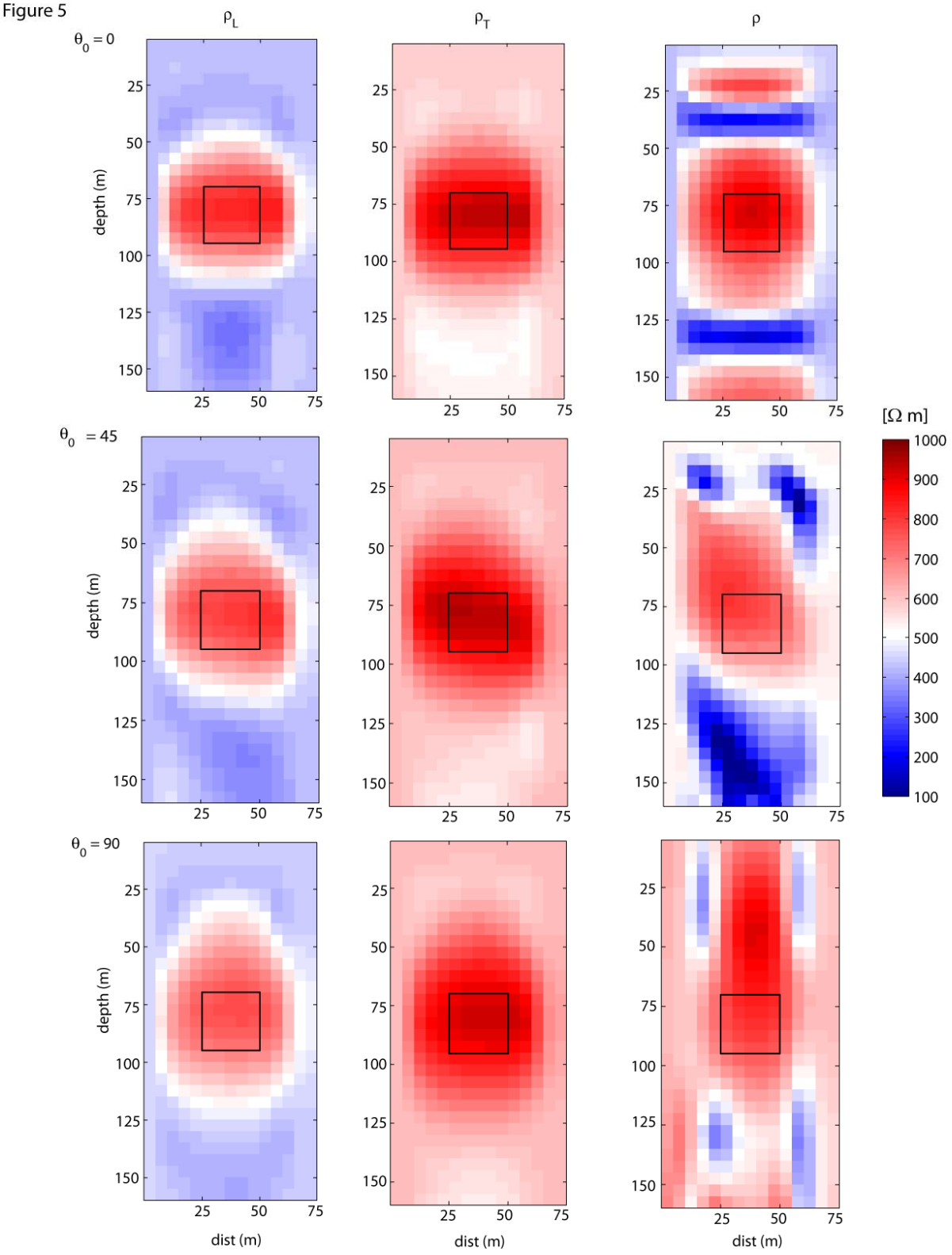

Figure 5: The comprehensive pole-pole data set inversion reconstruction of an anisotropic background model (constant λ= 1.22) with isotropic inclusion (1250 Ohm m). The left (ρ_L) and middle (ρ_T) columns are produced with the anisotropic assumption while the right column assumes isotropy (ρ). The axis of symmetry (normal to plane of isotropy) varies fromθ_0= 0, 45, 90 degrees in the top, middle and bottom rows respectively.

Figure 6

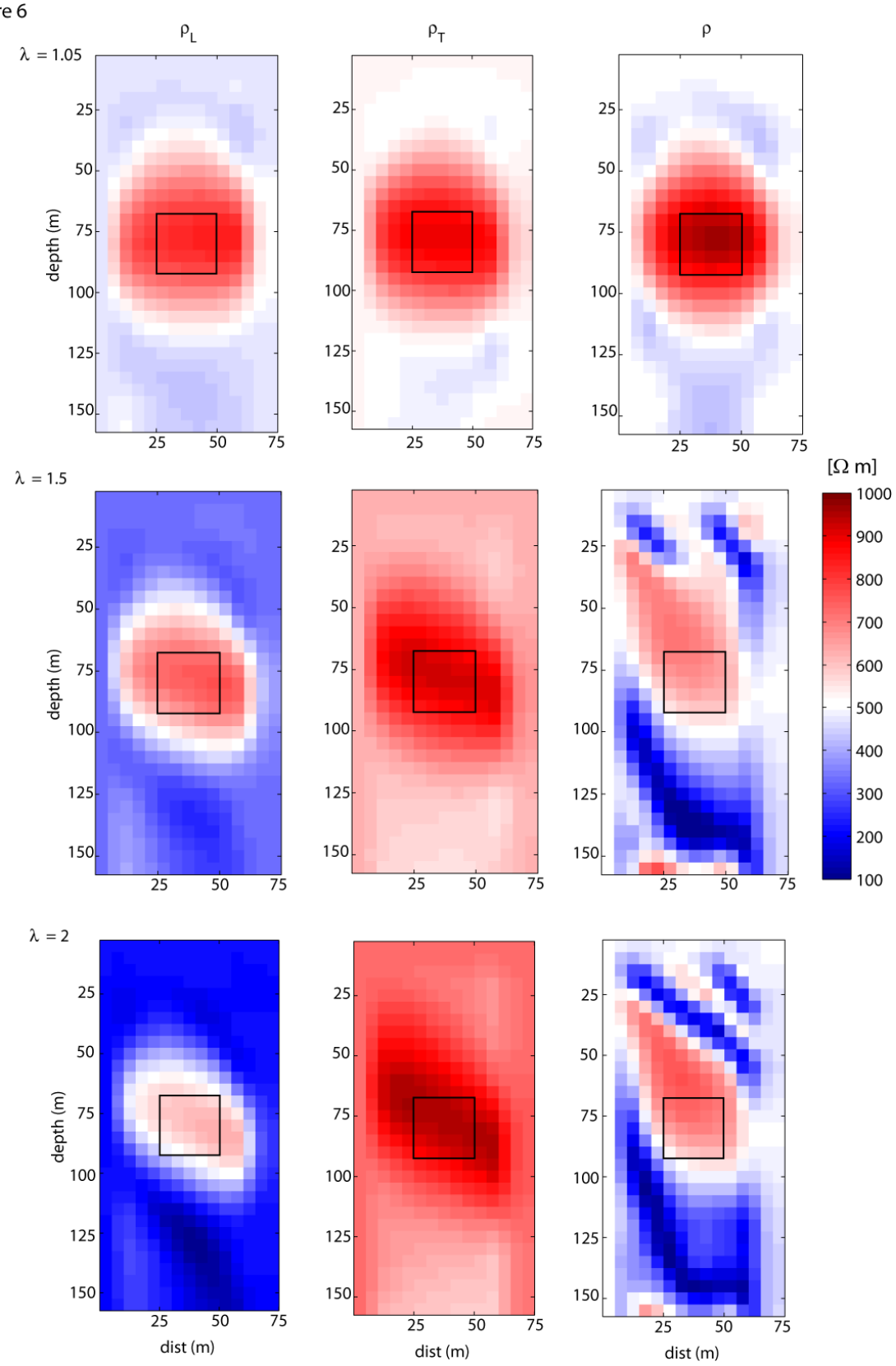

Figure 6: The comprehensive pole-pole data set reconstruction of anisotropic background model (θ_0 = 45 degrees) with isotropic inclusion (1250 Ohm m). The true model magnitude of anisotropy variesλ = 1.05, 1.5, 2 from top to bottom rows. The columns are in the same format as Figure 5.

We now present in Figure 6 the effects of the magnitude of anisotropy of the background medium for the same style of model as above. Anisotropy was varied from slight (almost isotropic) values to highly anisotropic values, where conductivity was four times larger parallel to the plane of isotropy than perpendicular to it. The true models used had $\theta_0 = 45°$, with the coefficient of anisotropy varied from $\lambda = 1.05$ (ρ_L = 475 Ω m, ρ_T = 525 Ω m), $\lambda = 1.5$ (ρ_L = 300 Ω m, ρ_T = 700 Ω m) and $\lambda = 2$ (ρ_L = 200 Ω m, ρ_T = 800 Ω m) in the top, middle and bottom rows, respectively. The isotropic anomaly conductivity value is 1250 Ω m. The inversion results presented in Figure 6 are in the same format as in Figure 5 i.e., ρ_L and ρ_T in the left and middle columns with ρ in the right column. The starting model used for the inversions was again the homogeneous isotropic resistivity equal to the geometric mean of the true anisotropic values of the background.

The reconstructions performed under the anisotropic assumption are accurate in resolving the true background resistivities. The increasing anisotropy (i.e. difference between ρ_L and ρ_T) is especially apparent in the intensifying colour values (both red and blue) from the top to bottom rows of the Figure. The high resistivity anomaly is centred over the true position (outlined in black) for all magnitudes of anisotropy. However, the reconstructed anomaly in the ρ_L image decreases in resistivity with increasing λ, whereas the opposite trend occurs for ρ_T. The ratio between the background and the anomaly resistivity is comparable for both ρ_L and ρ_T resistivities for the intermediate and high λ values. The effect of the angle of the symmetry axis ($\theta_0 = 45°$) is apparent, since the reconstructions undertaken with the incorrect isotropic assumption show the target to be elongated along this orientation for large values of anisotropy. The high resistivity target was harder to image for the high λ value (bottom row) because the ρ_T background increased to such an extent that the difference between the background resistivity and that of the anomaly became much less significant.

The image obtained using an isotropic inversion algorithm shows superior recovery of the isotropic block for slight anisotropy (top row) to that obtained with an anisotropic inversion, specifically in terms of the resistivity structure resolved compared to the true model. However, for increasing magnitudes of anisotropy (middle and bottom rows), spurious low resistivity artefacts become apparent. A region of high resistivity is resolved but it is greatly stretched in the direction parallel to the plane of isotropy. The banded artefacts also parallel this orientation. The data misfits for these inversions increased with the magnitude of anisotropy (> 7 times the numerical noise), apart from the almost isotropic model in which the isotropic inversion converged to the numerical noise levels of 1 to 2 %. All the inversions undertaken with the correct anisotropic assumption converged to within numerical noise levels of 1 to 2 %.

We next investigate a similar type of anisotropic background model but this time with two embedded isotropic targets, one high resistivity (1250 Ωm), the other low resistivity (50 Ωm), and using a purely surface electrode array involving 61 electrodes. The pole-dipole comprehensive set (large geometry factor data filtered out) of 12,511 electrode configurations was employed for the reconstruction. The true models used had an axis of symmetry of θ_0 = 45°, with the coefficient of anisotropy for the background varied from $\lambda = 1.1$ (ρ_L = 450 Ωm, ρ_T = 550 Ω m), $\lambda = 1.4$ (ρ_L = 325 Ω m, ρ_T = 675 Ω m) and $\lambda = 2$ (ρ_L = 200 Ω m, ρ_T = 800 Ω m), corresponding to the top, middle and bottom rows of Figure 7, respectively. The inversion results are given in the same format as before, with the reconstructed ρ_L and ρ_T values shown in the left and middle columns of Figure 7, and the isotropic inversion result for ρ given in the right column. Inversions were again started with isotropic resistivities equal to the geometric mean of the true values.

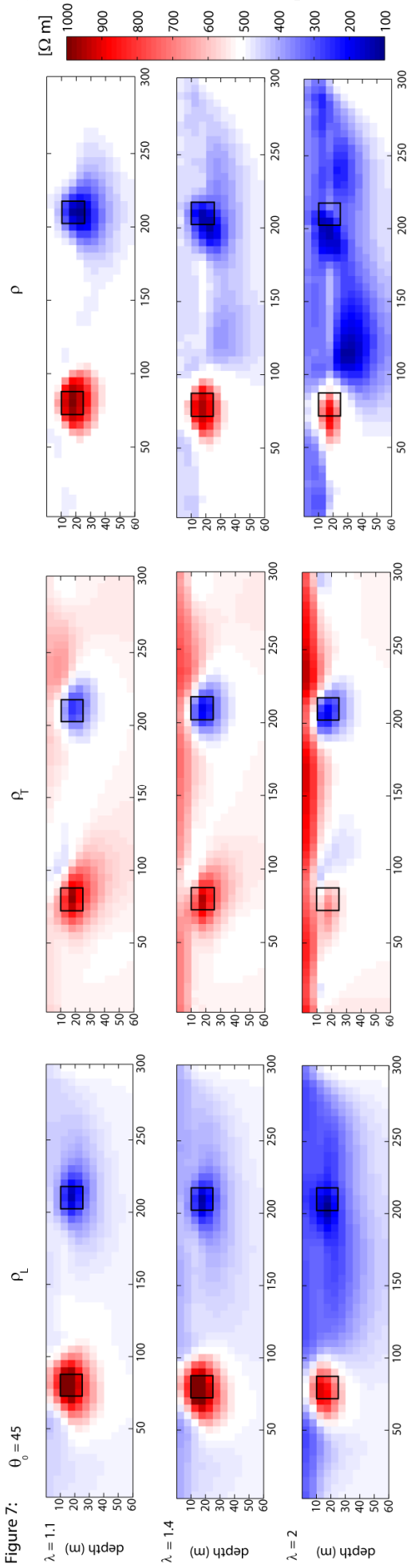

Figure 7: Inversion reconstruction of a surface electrode array experiment. The pole-dipole comprehensive data set reconstructed a true anisotropic background model ($\theta_0 = 45$ degrees) with high (1250 Ohm m) and low (50 Ohm m) isotropic inclusions. The true model magnitude of anisotropy varies $\lambda = 1.1, 1.4, 2$ from top to bottom rows. The columns represent ρ_L, ρ_T and ρ.

The reconstructions carried out with the anisotropic assumption are accurate, and able to resolve the increasing anisotropy which is apparent from the changing colours from the top to bottom rows. Both high and low resistivity anomalies are centred over their true positions (outlined in black) for all magnitudes of anisotropy. However, the reconstructed high resistivity target in the ρ_L image decreases in resistivity magnitude noticeably at $\lambda = 2$. In the ρ_T images, the high resistivity target becomes poorly resolved as λ increases. The resolving power of the ρ_T parameter drops with depth far more significantly than ρ_L (see Wiese *et al*. 2009).

The image obtained with the incorrect isotropic assumption (isotropic inversion code) shows superior recovery of the isotropic blocks for the slight anisotropy case (top row) compared to that using an anisotropic inversion, specifically in terms of the level of target resistivity resolved. However, for the model with a high level of anisotropy (bottom row), spurious low resistivity artefacts become apparent in the isotropic image. The data misfits with the isotropic inversion are not as high as in the 3-sided experiments (Figures 5 and 6), but the same trend of increasing data RMS with increasing levels of anisotropy was again observed.

4.2. Isotropic Background with an Anisotropic Block Inclusion

In this section we present inversion results for an anisotropic target (block) in an isotropic background. The target is located midway between the boreholes and has square geometry; its electrical properties are $\rho_L = 250\ \Omega$ m, $\rho_T = 750\ \Omega$ m ($\lambda = 1.7$) with $\theta_0 = 45$. The isotropic background is $\rho_L = \rho_T = 500\ \Omega$ m. Inversion results from a range of different electrode configurations and data sets are presented and compared. All inversions were started with an isotropic assumption $\rho = \rho_L = \rho_T = 500\ \Omega$ m.
Figure 8 shows the inversion results for the pole – pole comprehensive (top row), the pole – dipole selected (middle row) and pole - dipole comprehensive (bottom row) data sets. The left and middle columns correspond to anisotropic reconstruction ρ_L and ρ_T parameters and the right to the isotropic ρ.

The pole-pole anisotropic inversion updated the ρ_L and ρ_T model parameters in the correct direction, with the spatial reconstruction giving the target anomaly at the true position (outlined by the black square). Resolution is more limited towards the centre of the boreholes, especially for ρ_T. The corresponding isotropic inversion produced artificial banding which is oriented in a direction parallel to the plane of isotropy. The pole-dipole comprehensive data, when inverted, resolved the anisotropic anomaly in terms of spatial sharpness and yielded resistivities closer to the true values than in the pole-pole case. Although the resistivity scale of the pole-dipole filtered data set inversion was slightly inferior to the comprehensive set, the reconstruction was very efficient by comparison, with similar results achieved using considerably less data and computer resources. The isotropic assumption inversions had data misfits more than ten times larger than the numerical noise limits inherent in the forward modelling scheme. The cause of the large misfits was the trend of artificial banding patterns of alternating high and low resistivity that lay parallel to the orientation of the plane of isotropy.

In Figure 9 we show inversion results for the pole-dipole comprehensive data set using the same model as in Figure 8, but the axis of symmetry of the target is varied thru $\theta_0 = 0$, 45, 90° from the top to the bottom row. An alternative form of presentation is used for the anisotropic parameters this time, with ρ_m and λ shown in the left and right hand columns,

Figure 8

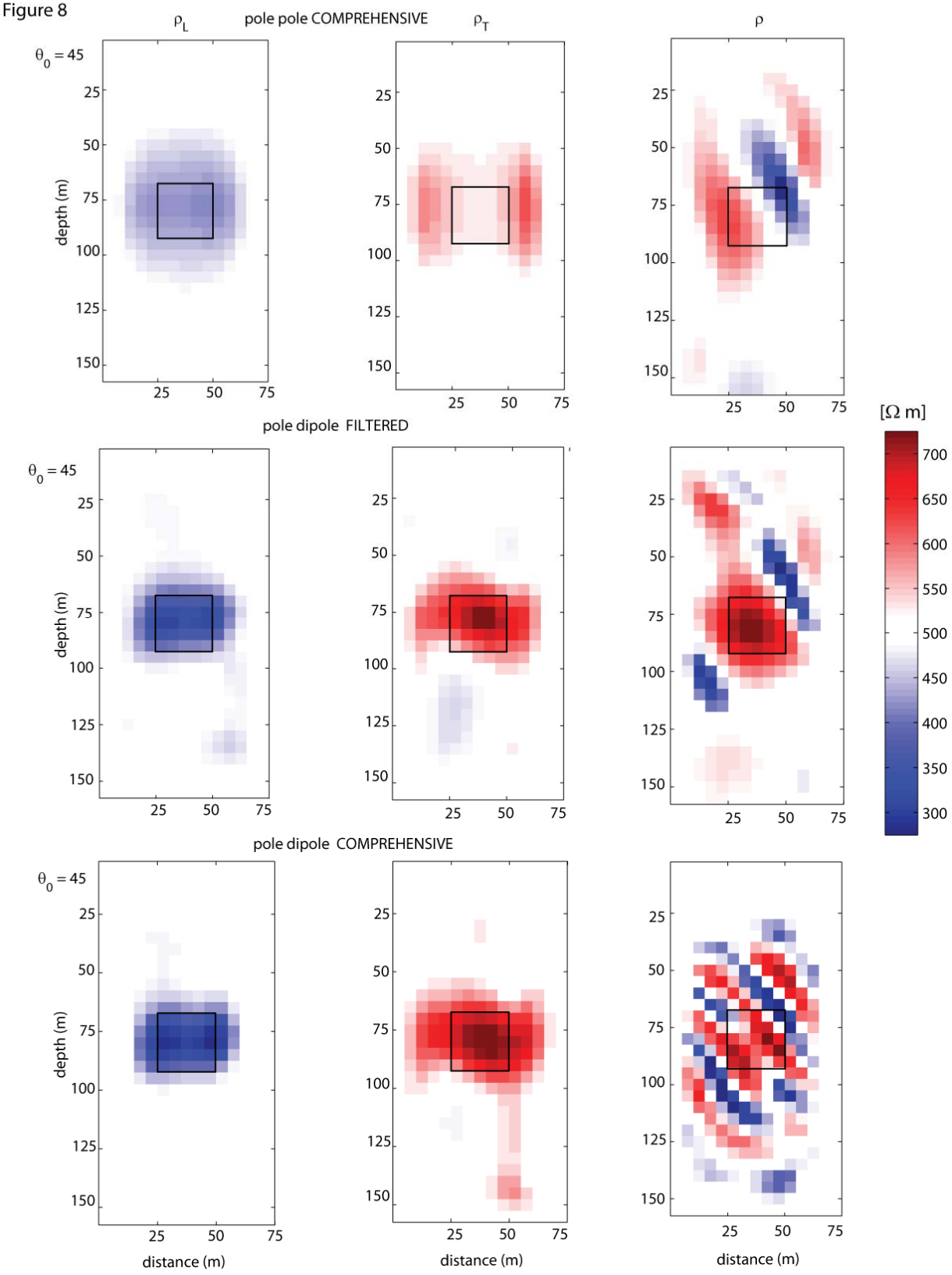

Figure 8: The pole-pole comprehensive (top), pole – dipole selected (middle) and pole dipole comprehensive (bottom row) inversion images for a model consisting of an isotropic background (500 Ohm m) with an anisotropic inclusion ($\lambda = 1.7$) and $\theta_0 = 45$ degrees.

Figure 9

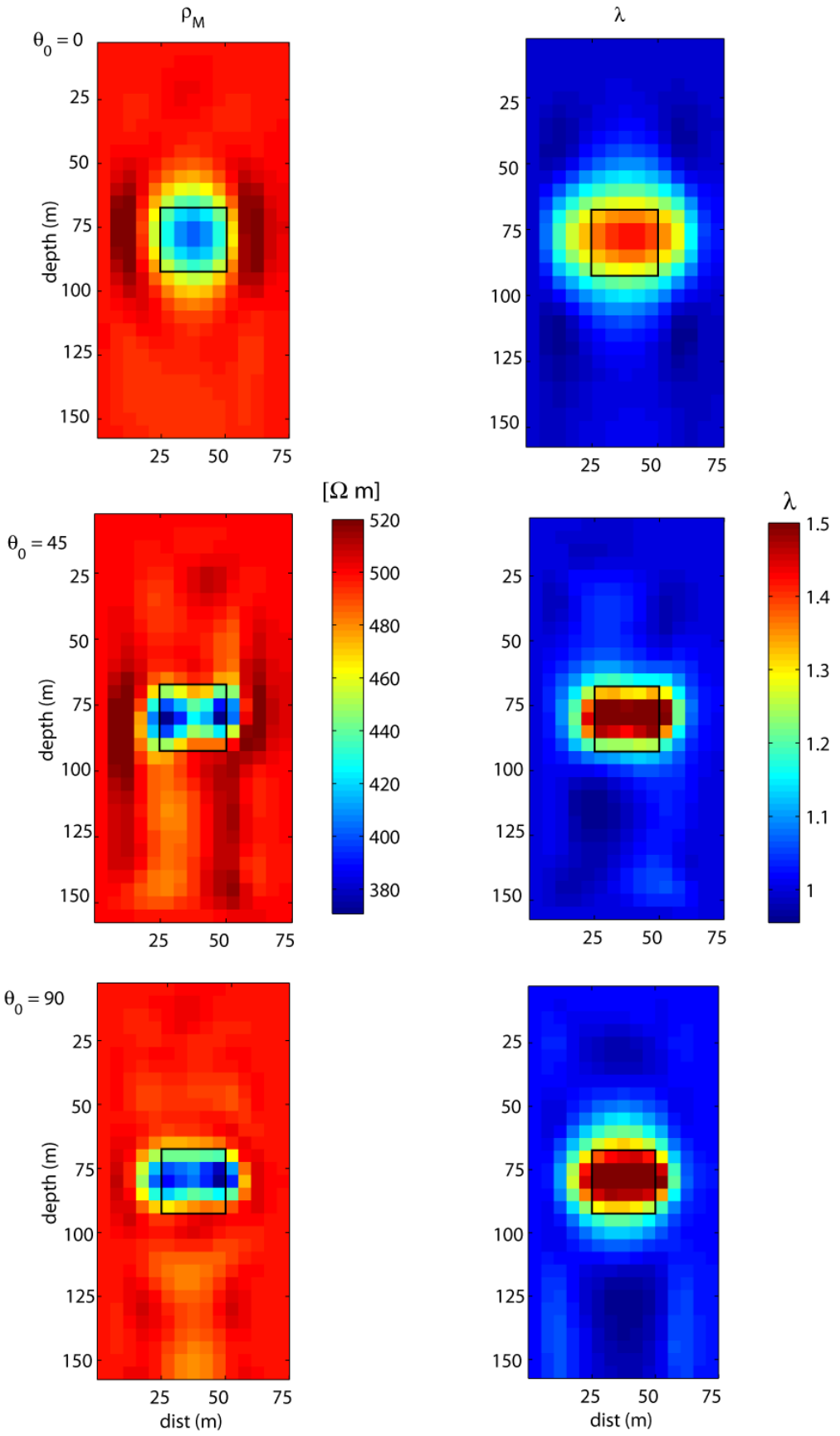

Figure 9: Alternative representation of the anisotropic model parameters produced by inversion using the pole – dipole comprehensive set. The mean resistivity (ρ_m) and the coefficient of anisotropy (λ) are displayed in the left and right columns respectively. The true model is the same as Figure 8 except the rows correspond to differing axis of symmetry angles: θ_0 = 0, 45, 90 degrees from top to bottom.

respectively. The λ plot is particularly revealing, indicating the correct true isotropic background ($\lambda \approx 1$). The anisotropic anomaly region is accurately represented with reddish colours, slightly underestimating the true value of $\lambda = 1.7$. The ρ_m images are hard to use for direct interpretation because it is a derived rather than physical quantity, and the anomaly region is dominated by the lower resistivity of ρ_L and ρ_m. This type of representation nevertheless has interpretative value, as demonstrated in Kim *et al.,* (2006), who were able to successfully delineate cavities by identifying regions of isotropy amongst an anisotropic background. The isotropic regions were cavities filled with either water or air.

To further quantify the goodness of the different data sets, we show in Figure 10 the normalised eigenvalue spectra calculated based on the true model. Firstly, it is notable that the spectra for ρ_L and ρ_T generally follow the same pattern except for low indices for the pole-pole data set. There is a distinct magnitude difference between the pole-pole and pole-dipole dominant eigenvalues, with the pole-dipole sets being larger by more than five orders of magnitude. The pole-dipole filtered and comprehensive sets are distinguishable with the comprehensive having higher normalized eigenvalues and assuming a gentler slope with increasing index. The slopes of the spectra from the 200^{th} eigenvalue onwards are close to parallel but the pole-dipole comprehensive curve is offset two orders of magnitude higher than the pole-pole data set and has the smallest null space of the three sets. Here the null-space can be thought of as the un-resolvable model parameters and therefore gives a good comparison between information content of the different data sets.

Figure 11 displays the diagonal elements of the formal model resolution matrix, R_{ii} (see equation 17) plotted at the respective model cells. The model used for this calculation was the anisotropic block model used throughout this section. The left hand columns of Figure 11 display the resolution for pole – pole (top) and pole – dipole comprehensive (middle) and the pole – dipole selective data sets for both ρ_L and ρ_T model parameters. For both ρ_L and ρ_T parameter highest resolution is seen closest to the electrodes for all data sets. The resolution values differ only slightly between ρ_L and ρ_T.

A direct comparison of the resolving power for each data set is presented in the right hand columns of Figure 11. The top panel shows the model resolution ratio of the pole – pole with respect to the pole – dipole comprehensive set, the bottom panel shows the pole – dipole selected data set with respect to the pole – dipole comprehensive set. The top ratio plot clearly show the superiority of the pole - dipole comprehensive set over the pole – pole set, with ratios below 20 % in the majority of model cells. The selective (filtered) pole – dipole set shows high ratios greater than 70 % of the pole – dipole comprehensive set for the central model region, which illustrates the merits of selecting data based on sensitivity considerations.

Figure 10

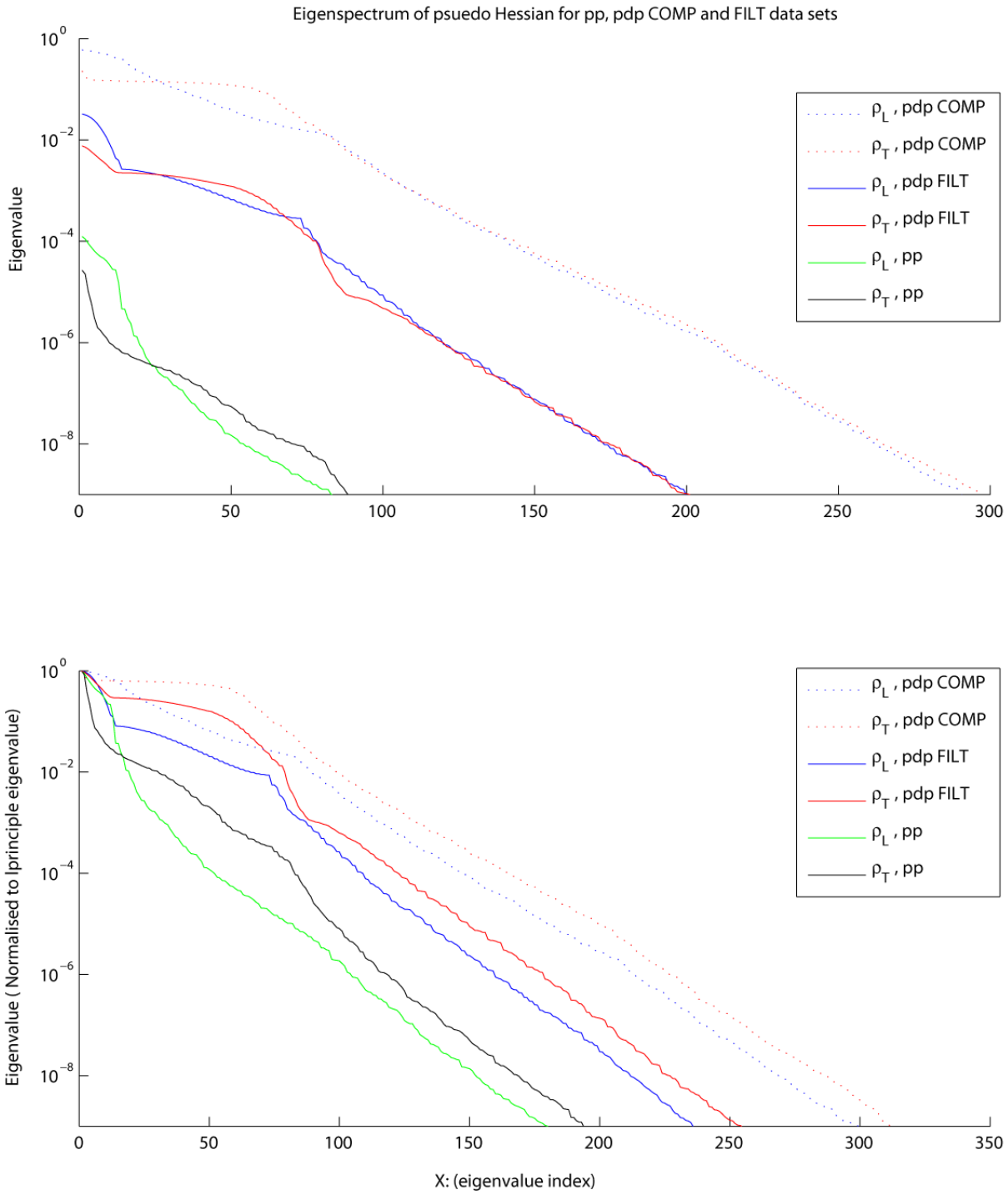

Figure 10: Raw (top) and normalised (bottom) Eigenspectra of the pseudo Hessian matrix ($J^T J$) for the pole – pole comprehensive (pp), pole – dipole selected (pdp SELECT) and pole – dipole comprehensive (pdp COMP) data sets. The calculation was based on the same model as in Figure 8.

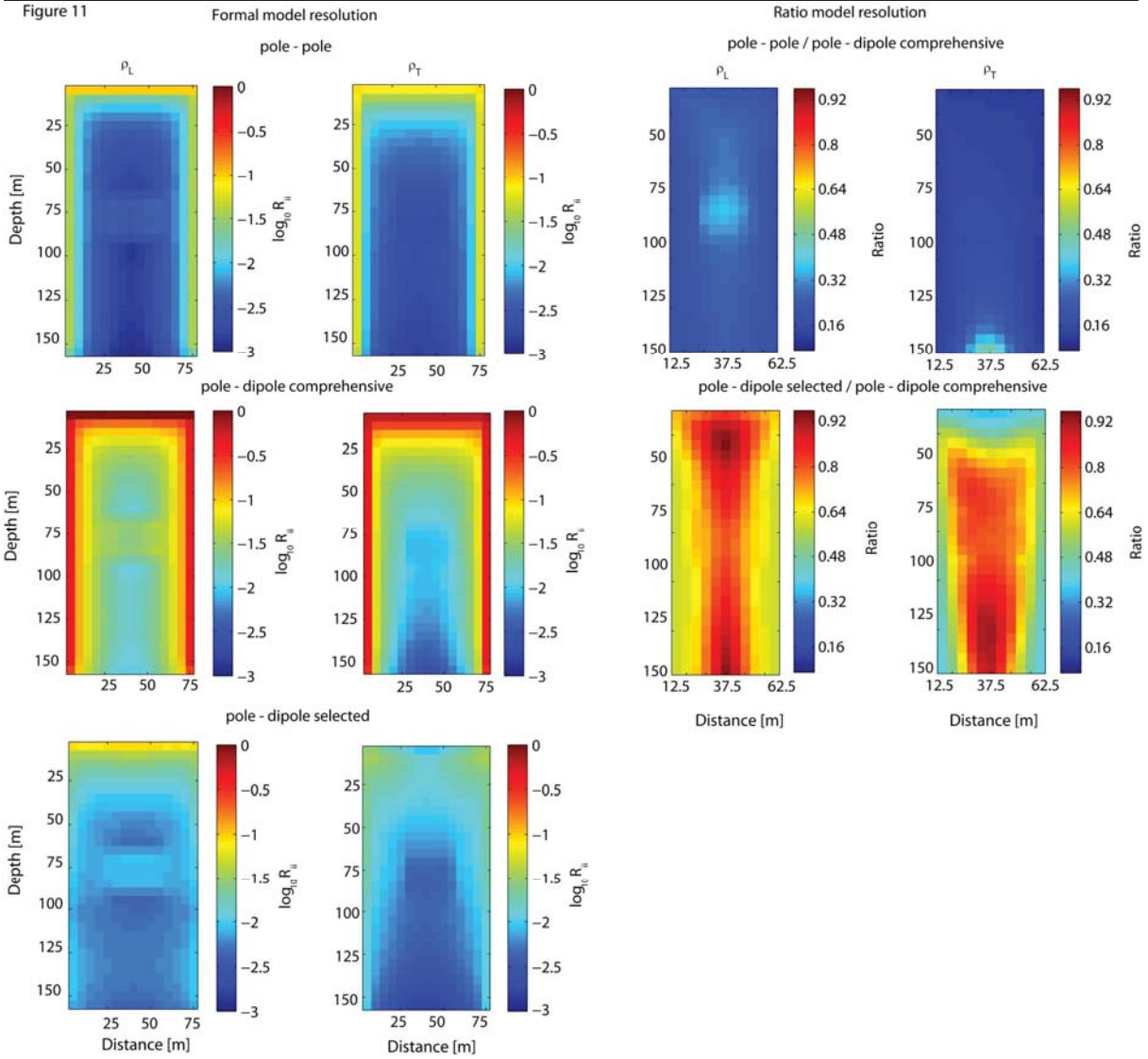

Figure 11: The formal model resolution (R_{ii}) is displayed in the two left most columns for the pole – pole (top row), pole –dipole comprehensive (middle row) and selective pole – dipole data sets (bottom row). The calculation was based on the same model as in Figure 8. The two right most columns display the ratio of the formal model resolution for the pole – pole (top row) and the pole – dipole selective (bottom row) with respect to the optimal pole – dipole comprehensive resolution.

4.3. Three Parameter Inversion

In the previous sections we focused on resistivity inversion incorporating anisotropy, and the erroneous results obtained using an incorrect isotropic inversion scheme. The anisotropic inversions were established for the two parameters ρ_L and ρ_T, with a fixed but arbitrary θ_0 angle defining the orientation of the symmetry axis. This method of constraint, by decreasing the number of model parameters to be solved for, effectively stabilizes the inversion without specifically penalizing anisotropy. In this section we broaden the inversion to obtain all three parameters at each cell for a 2D TTI model. Previous studies (e.g., LaBreque *et al.,* 2004; Herwanger *et al.,* 2004; Kim *et al.,* 2006; Li *et al.,* 2011) have all ignored the angle of anisotropy by assuming the principal resistivitiy directions coincide with the co-ordinate frame. The implication of including the extra model parameter (the orientation of the axis of symmetry) is to increase the non-uniqueness and non-linearity of the inversion problem. In section 2.1, two equivalent descriptions for the three anisotropic model parameters were given, the Cartesian and the principal axis (eigen) frame.

As an instructive preliminary investigation to assess the preferred model description to use in the inversion, we computed the eigenvalue spectra of the pseudo Hessian matrix for the two different formulations: ρ_L, ρ_T, θ_0 and $\rho_{XX}, \rho_{XZ}, \rho_{ZZ}$. These are shown in the top and bottom panels, respectively, of Figure 12. The eigenspectra were calculated for a homogeneous anisotropic model with λ = 1.4 and θ_0 = 45 degrees. The spectra are extremely similar, with the exception of the newly introduced parameters: θ_0, ρ_{XZ}. The spectra related to θ_0 are five orders of magnitude higher than ρ_L, ρ_T and the Cartesian parameters $\rho_{XX}, \rho_{XZ}, \rho_{ZZ}$. The sensitivities for the θ_0 angle are also orders of magnitude larger than the anisotropic resistivity model parameters. The source of the amplitude difference in the sensitivity and the eigenvalues most probably stems from the different units of the eigenframe model parameters θ_0 (degrees) versus ρ_L, ρ_T (Ω m). Such large differences in sensitivity magnitude can destabilise an inversion (see later). This difference is not encountered in the Cartesian frame, because all parameters have similar sensitivity magnitude. However, the ρ_{XZ} parameter is less physically meaningful than the θ_0 angle.

The ρ_L, ρ_T, θ_0 model employed to produce the first set of synthetic data for the three parameter inversion experiment is shown in Figure 13 (a). The model is a four-layered TTI medium, where each layer has a different coefficient of anisotropy and axis of symmetry (or dip of the plane of isotropy).The ρ_L, ρ_T (or alternatively: ρ_{XX}, ρ_{ZZ}) parameters control the degree of anisotropy, which for this experiment is λ = 1.4 in the top and bottom layers and λ = 2.4 in the middle layer. The θ_0, ρ_{XZ} parameters control the orientation of the TTI axis of symmetry, which varies in the four layers (from the top to bottom layer the values are θ_0 = 45, 37.5, 0, -45 degrees respectively).

Inversions of synthetic data from the same model were carried out using two different approaches. Firstly, the natural rock frame model parameters ρ_L, ρ_T, θ_0 were used directly. Secondly, the ρ_L, ρ_T, θ_0 values were initially converted into the Cartesian domain values $\rho_{XX}, \rho_{XZ}, \rho_{ZZ}$ with forward calculations, sensitivity calculations and inversion model updates made with respect to the Cartesian model parameters. On completion of the inversion procedure, the Cartesian output values for the final images were transformed back into the ρ_L, ρ_T, θ_0 parameter form for display. An equivalent slightly anisotropic starting model was given for both inversions (e.g., ρ_L= 260 Ω m and ρ_T= 300 Ω m, θ_0 = 0°). Larger smoothing parameters were applied to both inversions to counteract the increased non-uniqueness of the inverse problem.

One attraction of working with the Cartesian frame is that all three parameters have the same units and comparable sensitivities. This is not the case for the eigenframe, because the dip angle parameter has different dimensions and far greater sensitivity values, as mentioned above. The effects of this will be evident later.

Figure 12

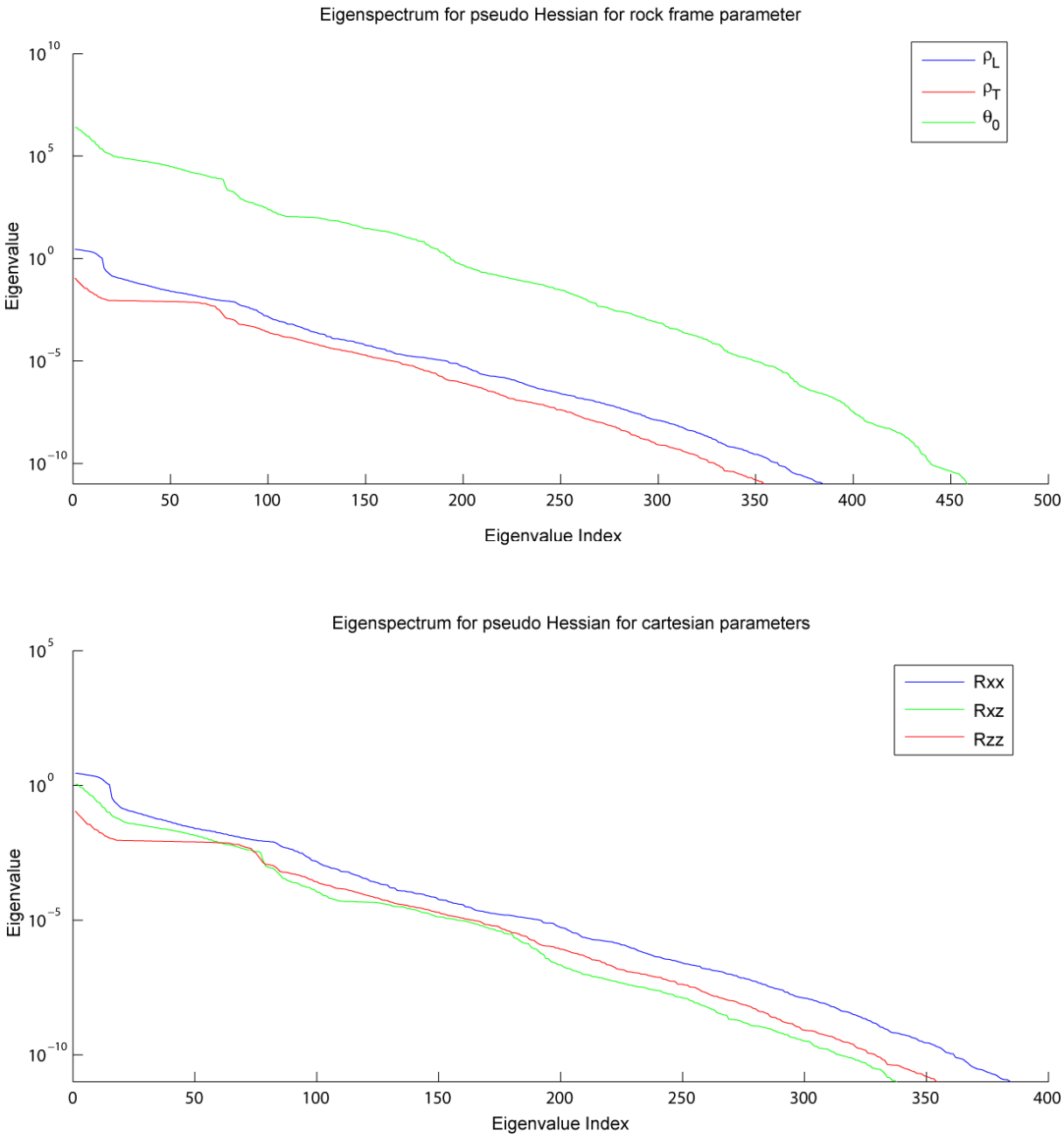

Figure 12: Three parameter eigenspectra comparison between eigen (or rock) frame (top) and Cartesian (bottom) parameters for an anisotropic block model with $\lambda = 1.4$ and $\theta_0 = 45$ degrees. Note the orders of magnitude difference between the eigenframe parameters, whereas the Cartesian parameters are all of similar order.

Figure 13 (b) shows the inversion results for the pole-dipole comprehensive data set carried out in the ρ_L, ρ_T, θ_0 domain, whereas Figure 13 (c) displays the corresponding results for the inversion performed in the $\rho_{XX}, \rho_{XZ}, \rho_{ZZ}$ domain then converted to ρ_L, ρ_T, θ_0 for presentation. Comparison of the reconstructions shows superior results for the inversion carried out in the Cartesian domain. The Cartesian frame inversion was successful in delineating all layer boundaries and resolving the correct orientations of the resistivity ellipses of the true model. The large difference in magnitude of sensitivity between the model parameters de-stabilizes the linearized inversion carried out in the ρ_L, ρ_T, θ_0 domain. Resistivity artefacts are observed in the ρ_L and ρ_T reconstructions.

Figure 13

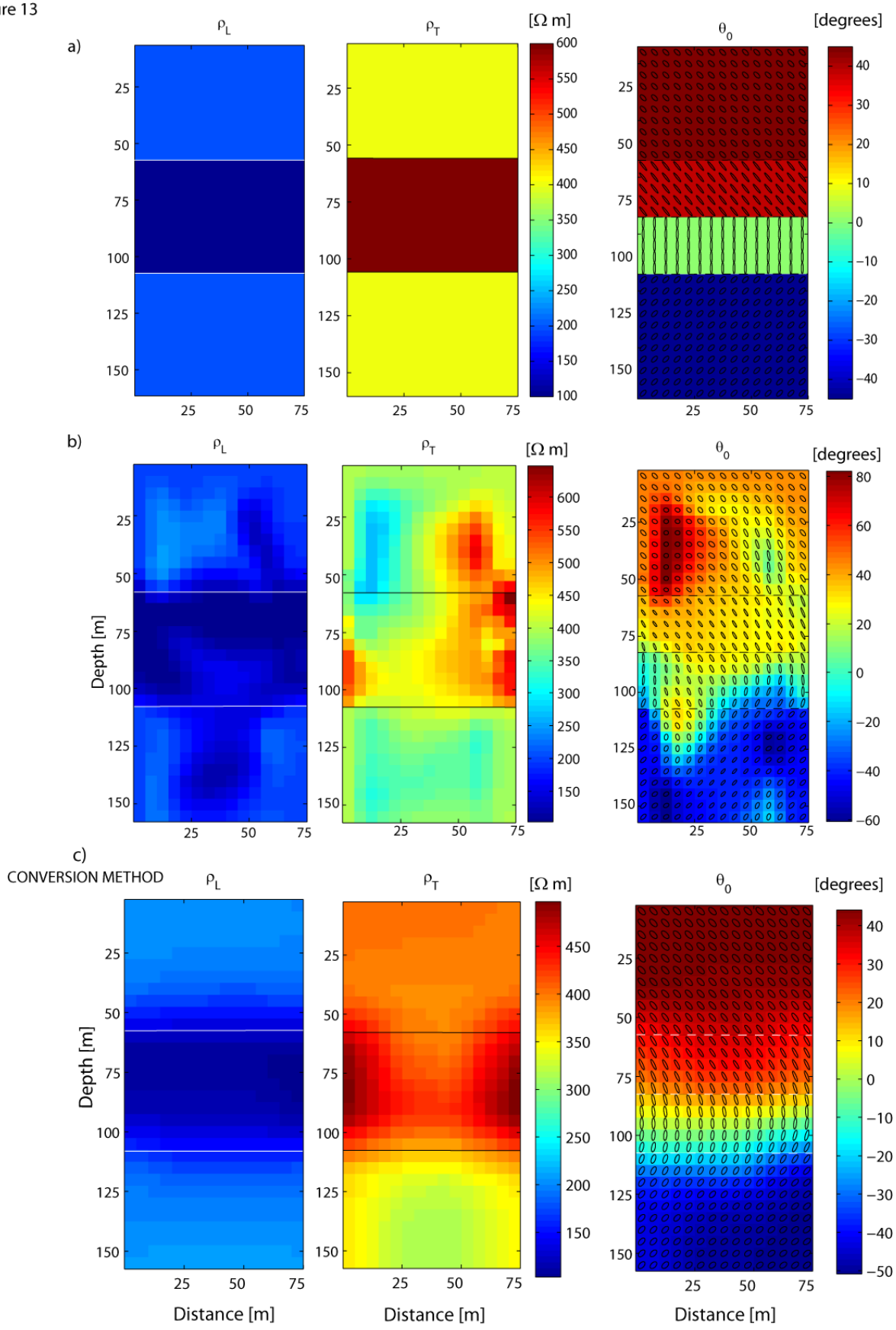

Figure 13: Three parameter inversion for a layered TTI media:
a) the true four layered synthetic model
b) inversion result conducted in the eigen (or rock) frame
c) inversion result conducted in the Cartesian co-ordinate frame and converted for presentation

They are especially noticeable in the ρ_T model parameter, where a section of low resistivity is observed at depths between 5 and 10 metres close to the left hand side borehole. This region indicates that the inversion update has actually been in the wrong direction. The other noteworthy point is the large scale difference between the Cartesian and eigenframe inversions, especially for the θ_0 and ρ_{XZ} parameters (see Figure 12). Values for θ_0 are updated to magnitudes as high as 80 degrees, though it is important to point out the region in which the high angle values occur corresponds to a region of relative isotropy. For an isotropic model the θ_0 angle has no real meaning because any angle will still satisfy isotropy. The data misfit converges to 12% for the ρ_L, ρ_T, θ_0 inversion, compared to 2.25% for the inversion in the $\rho_{XX}, \rho_{XZ}, \rho_{ZZ}$ domain.

Figure 14 shows an inversion reconstruction for a second model consisting of a single anisotropic block in an otherwise isotropic background of 500 Ωm. The anisotropic targets both have ρ_L= 300 Ω and ρ_T= 700 Ω m, with the target having an axis of symmetry defined by θ_0 = + 45 degrees. The coefficient of anisotropy was not extreme at λ =~1.5, so as to keep the non-linearity of the inversion to manageable levels. The inversion was carried out in the Cartesian frame as this produced the more accurate results in the previous experiment. After convergence, the model parameters were converted to the eigenframe for presentation. An isotropic starting model of $\rho_{XX} = \rho_{ZZ}$ = 500 Ωm and ρ_{XZ} = 0 Ω m was employed. The reconstruction of the true targets in terms of resistivity values (ρ_L and ρ_T) and true location is accurate for both cases. Slight smearing effects are observed especially for the ρ_T parameter beneath the target away from the increased sensitivity of the surface electrodes.

Figure 14

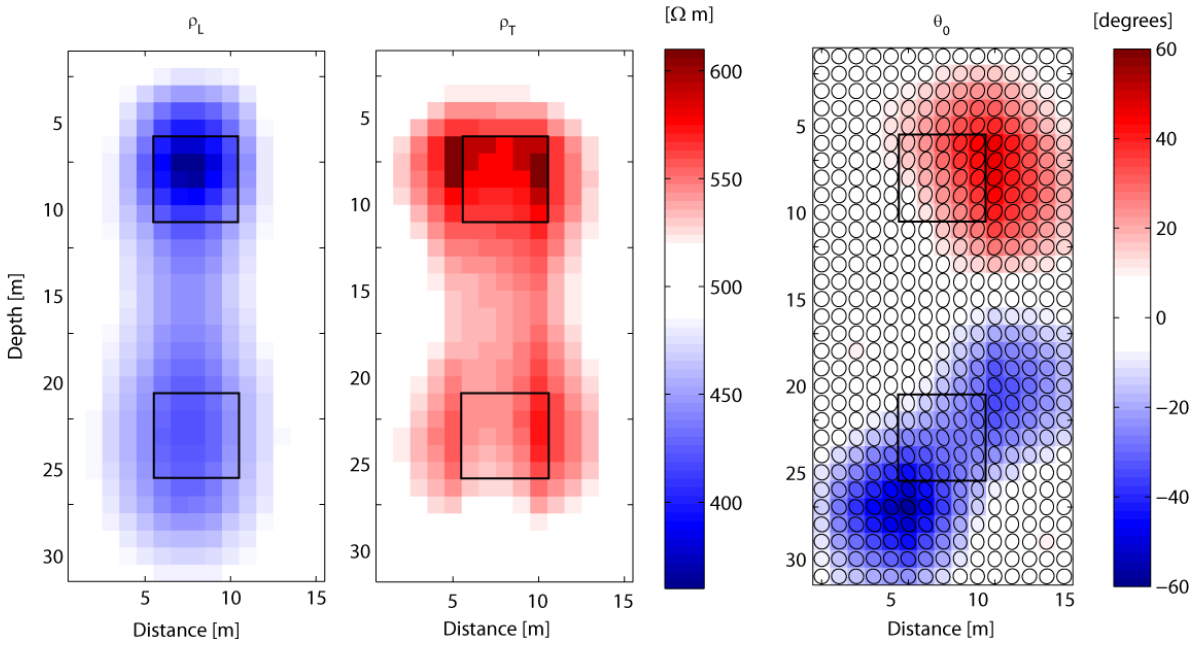

Figure 14: Three parameter inversion of anisotropic block in isotropic background. The block position is outlined in black. The true model parameters were: ρ_L= 300 Ωm and ρ_T= 700 Ω m, with the target having an axis of symmetry defined by θ_0 = + 45 degrees. The inversion was carried out in the Cartesian co-ordinate frame and transformed back into the eigen (or rock) frame.

The θ_0 reconstruction showed relatively poor spatial resolution of the target. The target angle itself was well resolved, with angles of up to 35 degrees recovered. Considerable smearing of the true axis of symmetry angle is apparent along an axis of symmetry direction of - 45 degrees.

Erroneous artificial angles in the form of negative values occur in the isotropic regions outside the true position of the target. These regions are positioned along the 45 degree axis of symmetry line from the centre of the true target with the top right hand artefact showing above -10 degree angles. Despite these artefacts the inversion converged to a data misfit of below 2 %. This example is important because it illustrates the problems associated with non-uniqueness when inverting for the third model parameter: ρ_{XZ} or θ_0.

5. CONCLUSIONS

We have conducted 2.5D resistivity inversion experiments in tilted transversely isotropic (TI) media. The synthetic data were computed for the true anisotropic models but the inversion scheme used forward solvers and sensitivity calculations for either the correct anisotropic assumption (two or three parameters at each cell defining the conductivity tensor) or the incorrect isotropic assumption (single conductivity value for each cell). This enabled direct comparison of the effect of the assumption (anisotropic vs isotropic) on the image constructions.

Synthetic models included isotropic targets embedded in a TI anisotropic background, as well as TI anisotropic blocks within an isotropic background, and in which the magnitude of anisotropy and the dip angle of the axis of symmetry were varied. These models were investigated through a series of experiments with varying orientation and magnitude of anisotropy. Superior reconstructions in terms of RMS data misfit, the true anomaly shape and position, and the anisotropic background parameters were achieved when the correct anisotropic assumption was employed. When the false (but widely practised) isotropic assumption was used the tomograms were dominated by patterns of banded artefacts. For increasing levels of anisotropy, the isotropic reconstructions became increasingly poor, with high data misfits. For weakly anisotropic media, isotropic inversions performed adequately, especially for surface electrode arrays

Various pole–pole, pole–dipole and dipole–dipole crosshole data sets were investigated by examining the accuracy of the inversion result, the eigenspectra spectrum of the pseudo Hessian matrix and the relative resolution plots. The pole-dipole comprehensive data set produced the best reconstructions. However, we found that a data selection scheme based on using only the high sensitivity measurements produced tomograms of comparable quality to those of the comprehensive data sets, but involving far fewer measurements and hence reduced computer memory and run time.

Reconstruction experiments were extended to resolving three anisotropic parameters at each model cell (dip angle of the symmetry axis in addition to the transverse and longitudinal resistivities). For a layered anisotropic model with model parameters described in different co-ordinate frames (Cartesian and the eigenframe) the Cartesian frame provided a more accurate inversion results and a smaller RMS data misfit. The eigenframe-based inversion instability was explained by means of the eigen-spectrum of the Hessian matrix which showed orders of magnitude difference between various parameters.

6. ACKNOWLEDGEMENTS

This research was supported by grants from the Australian Research Council and the Swiss National Science Foundation. The authors are grateful to Laurent Marescot and Mark Greenhalgh for many stimulating discussions.

7. REFERENCES

Al-Garnt, M. and Everett, M.E. 2003.The paradox of anisotropy in loop-loop electromagnetic response over a uniaxial halfspace. *Geophysics* **68**, 892-899.

Asten M.W. 1974. The influence of electrical anisotropy on mise a la masse surveys. *Geophysical Prospecting* **22**, 238-245.

Athanasiou E.N., Tsourlos P.I. and Papazachos C.B. 2009. Optimizing electrical resistivity array configurations by using a method based on the sensitivity matrix. 15th EAGE Near Surface meeting, Extended Abstract.

Bibby H.M., Caldwell T.G., Brown C. 2005.Determinable and non-determinable parameters of galvanic distortion in magnetotellurics. *Geophysical Journal International* **163**, 915-930.

Bhattacharya P.K and Patra H.P. 1968. Direct Current Geoelectric Sounding: Principles and Applications: Elsevier.

Blome M. 2009. Efficient measurement and data inversion strategies for large scale geoelectric surveys. PhD Thesis, ETH Zurich.

Blome M., Maurer H. and Greenhalgh S.A. 2011. Geoelectric experimental design – Efficient acquisition and exploitation of complete pole-bipole data sets. *Geophysics* **76**, 15-26.

Busby J.P. 2000.The effectiveness of azimuthal apparent resistivity measurements as a method for determining fracture strike orientations. *Geophysical Prospecting* **48**, 677-698.

Butler D. ed. 2005. Near Surface Geophysics, Society Exploration Geophysics, Tulsa.

Caldwell T.G. and Bibby H.M. 1998. The instantaneous apparent resistivity tensor: a visualisation scheme for LOTEM electric field measurements. *Geophysical Journal International* **135**, 817-834.

Collins J.L., Everett M.E. and Johnson B. 2006. Detection of near surface horizontal anisotropy in a weathered metamorphic schist by transient electromagnetic induction. *Physics of the Earth and Planetary Interior* **158**, 159-173.

Doetch J., Linde N., Coscia I., Greenhalgh S. and Green A. 2010. Zonation for 3D aquifer characterization based on joint inversions of multimethod crosshole geophysical data. *Geophysics* **75**, 53-64.

Dekker D.L.and Hastie L.M. 1980. Magnetotelluric impedance of an anisotropic layered earth model. *Geophysical Journal Royal Astronomical Society* **61**, 11-20.

deGroot-Hedlin C. and Constable S. 1990. Occam's inversion to generate smooth, two dimensional models from magnetotelluric data. *Geophysics* **55**, 1613-1624.

Dey A. and Morrison H.F. 1979. Resistivity modelling for arbitrarily shaped two-dimensional structures. *Geophysical Prospecting* **27**, 106–136.

Everett M.E and Constable S.C. 1999.Electric dipole field over an anisotropic seafloor. Theory and approach to the structure of the 40MA Pacific Ocean lithosphere. *Geophysical Journal International* **136**, 41-56.

Gianzero S. 1999. The Paradox of Anisotropy revisited. *The Log Analyst***40**, No. 6.

Greenhalgh S.A., Zhou B. and Green A. 2006. Solutions, algorithms and inter-relations for local minimization search geophysical inversion. *Journal of Geophysics and Engineering* **3**, 101-113.

Greenhalgh M., 2008. DC resistivity modelling and sensitivity analysis in anisotropic media. *PhD thesis*, University of Adelaide.

Greenhalgh S.A., Marescot L., Zhou B., Greenhalgh M., Wiese T., 2009a. Electric potential and Fréchet derivatives for a uniform anisotropic medium with a tilted axis of symmetry: *Pure and applied geophysics* **166**, 673 – 699.

Greenhalgh S.A., Zhou B., Greenhalgh M., Marescot L. and Wiese T. 2009b. Explicit expressions for the Fréchet derivatives in 3D anisotropic resistivity inversion. *Geophysics* **74**, 31-43.

Greenhalgh S.A., Wiese T. and Marescot L. 2010. Comparison of DC sensitivity patterns for anisotropic and isotropic media. *Journal of Applied Geophysics* **70**, 103-112.

Habberjam G.M. 1975. Apparent resistivity, anisotropy and strike measurements. *Geophysical Prospecting* **23**, 211-247.

Herwanger J.V., Pain C.C., Binley A., de Oliveira C.R.E. and Worthington M.H. 2004. Anisotropic resistivity tomography. *Geophysical Journal International* **158**, 409-425.

Hill D.G. 1972. A laboratory investigation of electrical anisotropy in precambrian rocks. *Geophysics* **37**, 1022-1038.

Keller G.V. and Frischknecht F.C. 1966.Electrical Methods in Geophysical Prospecting: Pergamon.

Kim J., Yi M., Cho S., Son J. and Song W. 2006. Anisotropic crosshole resistivity tomography for ground safety analysis of a high-storied building over an abandoned mine. *Journal of Environmental and Engineering Geophysics* **11**, 225-235.

LaBreque D.J., Heath G, Sharpe R. and Versteeg R. 2004. Autonomous monitoring of fluid movement using 3-D electrical resistivity tomography. *Journal of Environmental and Engineering Geophysics* **9**, 167-176.

Lehmann H., 1995. Potential representation by independent configurations on a multi-electrode array. *Geophysical Journal International* **120**, 331-338.

Le Masne D. and Vasseur G. 1981.Electromagnetic field of sources at the surface of a homogeneous halfspace with horizontal anisotropy: application to fissured media. *Geophysical Prospecting* **29**, 803-821.

Li Y. and Spitzer K. 2005. Finite element resistivity modelling for three-dimensional structures with arbitrary anisotropy. *Physics of the Earth and Planetary Interior* **150**, 15 - 27.

Linde N., Pedreson L.B. 2004. Evidence of electrical anisotropy in limestone formations using the RMT technique. *Geophysics* **69**, 909-916.

Loewenthal D. and Landisman M. 1973. Theory for magnetotelluric observation on the surface of a layered anisotropic half-space. *Geophysical Journal of the Royal Astronomical Society* **35**, 195-214.

Loke M.H., Wilkinson P.B. and Chambers J.E. 2010. Fast computation of optimized electrode arrays for 2D resistivity surveys. *Computers and Geoscience* **36**, 1414-1426.

Lu X., Alumbaugh D.L. and Weiss C.J. 2002. Electric fields and currents produced by induction logging instruments in anisotropic media. *Geophysics* **67**, 478-483.

Maillet R. 1947. The fundamental equations of resistivity prospecting. *Geophysics* **12**, 529-556.

Matias M.J.S. 2002. Square array anisotropy measurements and resistivity sounding interpretation. *Journal of Applied Geophysics* **49**, 185-194.

Maurer H. and Boerner D. 1998. Optimized and robust experimental design: a non-linear application to EM sounding. *Geophysical Journal International* **132,** 458-468.

Maurer H. and Freidel S. 2006. Outer space sensitivities in geoelectrical tomography. *Geophysics* **71**, 93-96.

Maurer H., Curtis A. and Boerner D. 2010. Recent advances in optimized geophysical survey design. *Geophysics* **75**, 177-194.

Menke W. 1989. Geophysical data analysis: Discrete inverse theory: Academic Press.

Pain C., Herwanger J., Saunders J, Worthington M and de Oliveira C. 2003. Anisotropic resistivity inversion. *Inverse Problems* **19**, 1081-1111.

Parkomenko E.I. 1967. Electrical properties of rocks: Plenum Press.

Reddy I.K. and Rankin D. 1971. Magnetotelluric effect of dipping anisotropies. *Geophysical Prospecting* **19**, 84-97.

Reynolds J.M. 2009. Introduction to Applied and Environmental Geophysics, 2nd Ed: John Wiley.

Rubin Y. and Hubbard S. eds. Hydrogeophysics: Springer Dordrecht.

Slater L., Sandberg S.K. and Jankowski M. 1998. Survey design procedures and data processing techniques applied to the EM azimuthal resistivity method. *Journal of Environmental Engineering Geophysics* **3**, 167-177.

Stummer P., Maurer H. and Green A. 2004. Experimental design: electrical resistivity data sets that provide optimum subsurface information. *Geophysics* **69**, 120-139.

Stummer P., Maurer H. and Horstmeyer H. 2002. Optimization of DC resistivity data acquisition: real-time experimental design and a new multielectrode system. *Geoscience and remote sensing* **40**, 2727-2735.

Wannamaker P.E. 2005. Anisotropy versus heterogeneity in continental solid earth electromagnetic studies: fundamental response characteristics and implications for physiochemical state. *Surveys in Geophysics***26**, 733-765.

Wang T. and Fang S. 2001. 3-D electromagnetic anisotropy modelling using finite differences. *Geophysics* **66**, 1386-1398.

Watson K.A and Barker R.D. 1999. Differentiating anisotropy and lateral effects using azimuthal resistivity offset soundings. *Geophysics* **64**, 739-745.

Weiss C.J. and Newman G.A. 2002. Electromagnetic induction in a fully 3D anisotropic earth. *Geophysics* **67**, 1104-1114.

Wiese T., Greenhalgh S.A. and Marescot L. 2009. DC resistivity sensitivity patterns for tilted transversely isotropic media. *Near Surface Geophysics* **7**, 125 – 139**.**

Wilkinson P.B., Meldrum P.I., Chambers J.E., Kuras O. and Ogilvy R.D. 2006. Improved strategies for the automatic selection of optimized sets of electrical resistivity tomograph measurements configurations. *Geophysical Journal International* **167**, 1119-1126.

Xu B. and Noel M., 1993. On the completeness of data sets with multi-electrode systems for electrical resistivity surveys. *Geophysical Prospecting* 41, 791-801.

Yi, M.J., Kim, J.H. and Chung, S.H. 2011. Three-dimensional anisotropic inversion of resistivity tomography data in an abandoned mine area. *Exploration Geophysics* **42**, 7-17.

Yin C. and Fraser D. 2004. The effect of electrical anisotropy on the response of helicopter-borne frequency-domain electromagnetic systems. *Geophysical Prospecting* **52**, 399-416.

Yu L. and Edwards N. 1992.The detection of lateral anisotropy of the ocean floor by electromagnetic methods. *Geophysical Journal International* **108**, 433-441.

Zhe J.P., Greenhalgh S., Marescot L. 2007. Multichannel full waveform and flexible electrode combination resistivity imaging system. *Geophysics* **72**, 57-64.

Zhou B. and Greenhalgh S.A. 2000. Crosshole resistivity tomography using different electrode configurations. *Geophysical Prospecting* **48**, 887-912.

Zhou B., Greenhalgh M. and Greenhalgh S.A. 2009. 2.5D/3D resistivity modelling in anisotropic media using Gaussian quadrature grids. *Geophysical Journal International* **16**, 938-950.

Chapter 7: Conclusions

7.1 Overall Significance

The non-invasive DC resistivity technique is used to supply critical information for delineation and interpretation of near-surface geological structures in engineering, environmental and mining applications. Successful inversions of field data to reconstruct the subsurface resistivity distribution are dependent on many factors:

- electrode configurations must be selected wisely to allow sufficient resolution with distance from the electrodes, while maintaining adequate signal to be detectable above noise limits.
- discretization of the model into forward and inversion grids must be chosen economically for processing time constraints. Also the model cell size should be chosen in accordance with the variability of the geology.
- sufficient measurements should be made or regularisation applied, in order to avoid an underdetermined problem.
- forward modelling code is needed to accurately compute the response of the given resistivity distribution, topography and anisotropy.
- sensitivity formulations are needed to update the inversion model correctly, so as to converge to the global minimum.

This thesis primarily addresses the last two key factors to ensure successful inversions. It concentrates on incorporating the influence of anisotropy on the resistivity technique, with emphasis on sensitivity calculations and inversion. In many geological settings the influence of anisotropy on the technique is significant. When it is not taken into account, anisotropy can produce erroneous results which can then be easily misinterpreted.

7.2 Contribution to Knowledge

This work presents analytic solutions for the electric potential, current density and Fréchet derivatives within a 3-D homogeneous TTI medium. The solution is valid for any point within or on the surface of such a medium. The equipotential contours are not orthogonal to the current density vectors, but display an elliptical pattern. This is a notable departure from the isotropic case.

The analytic solutions are supported by a numerical formulation to calculate sensitivity functions for a heterogeneous (2D, 3D), anisotropic medium. The formulation is based on Green's functions for the true and the adjoint source, which must be computed by numerical means such as the finite element method or the newly developed Gaussian quadrature grid approach. The equations also involve the derivatives of the conductivity tensor with respect to the principal conductivity values and the orientation angles of the symmetry axis. These are derived and presented in analytic form for a very general class of anisotropy, as well as a simplified TTI medium.

Using the presented formulations enabled a thorough investigation into anisotropic sensitivity for TTI media. Fréchet derivatives were computed and presented for a range of TTI model parameters: $\rho_L, \rho_T, \theta_0, \phi, \lambda, \rho_M$. The effects of various levels and orientations of anisotropy were tested along with different electrode configurations. General trends emerged for the

longitudinal and transverse resistivity Fréchet derivative patterns. A close link between the components of current density perpendicular and parallel to the axis of symmetry and the longitudinal and transverse resistivity is evident.

By reformulating the TTI model parameters in terms of the coefficient of anisotropy and the mean resistivity, comparison of isotropic and anisotropic sensitivity patterns were presented. This was achieved by computing and presenting the ratio of the respective sensitivities for various levels of anisotropy and orientations of the axis of symmetry. The results showed that significant divergence from a ratio of 1 (where anisotropic and isotropic sensitivity are equal) is observed for medium to strongly anisotropic rocks ($\lambda > 1.2$) and for steeply dipping planes of isotropy. Sensitivities were even found to be opposite in sign in some regions of the model. This would lead to very different and erroneous adjustments in the model parameters in these regions during an inversion, if an isotropic assumption is made and the ground is anisotropic.

Using the novel Gaussian quadrature grid forward modelling formulation, I have developed anisotropic resistivity inversion software. This is capable of handling complexities such as medium heterogeneity and the most general form of anisotropy. Throughout the thesis the complexity of anisotropy was chosen to be the widely used TTI class.

A large part of the research presented is in the area of anisotropic resistivity sensitivity. Understanding and formulating sensitivity correctly is a key step to almost all successful inversion strategies. Sensitivity patterns were investigated for different anisotropic parameters, electrode arrangements and levels of anisotropy/orientation of axis of symmetry. For the first time comparisons between anisotropic and isotropic sensitivity patterns were drawn, with divergence between the two becoming noticeable and possibly problematic for modest levels of anisotropy.

Having established successful sensitivity calculations, the next step was 2.5D inversion experiments in tilted transversely isotropic (TI) media. Synthetic data were computed for the true anisotropic models but the inversion scheme used forward solvers and sensitivity calculations for either the correct anisotropic assumption (two or three parameters at each cell to define the spatially variant conductivity tensor) or the incorrect isotropic assumption (single conductivity value for each cell). This enabled direct comparison of the effect of the assumption (anisotropic vs isotropic) on the image constructions.

Superior reconstructions in terms of data misfit, true anomaly shape and position, and the anisotropic background parameters were achieved when the correct anisotropic assumption was employed. When the false (but widely practiced) isotropic assumption was used the tomograms were dominated by patterns of banded artefacts. For increasing levels of anisotropy, the isotropic reconstructions became increasingly poor, having higher data misfits. For weakly anisotropic media, the isotropic inversions performed adequately, especially for surface-based arrays.

Reconstruction experiments were extended to resolving three anisotropic parameters at each model cell (dip angle of the symmetry axis in addition to the transverse and longitudinal resistivities). For a layered anisotropic model with model parameters described in different co-ordinate frames (Cartesian and the eigenframe), the Cartesian frame provided a more accurate inversion result and a smaller RMS data misfit. The eigenframe –based inversion instability was explained by means of the eigen-spectrum of the pseudo-Hessian matrix, which showed orders of magnitude difference between the different parameters.

The chapters in this thesis provide a solid foundation for incorporating electrical anisotropy into resistivity interpretations. The benefits to inversion of including anisotropy when it is present have been clearly demonstrated. A description of the anisotropic conductivity tensor

has been offered, along with sensitivity and inversion demonstrations for various anisotropic models. I believe that the foundations laid from this research will be a fruitful place to start for future research endeavours.

7.3 Future Directions

A valuable extension to research in the area of anisotropic resistivity inversion would be a series of laboratory- based experiments. To the best of the author's knowledge, this would be a novel area of research. It would provide definitive results proving or disproving the success of an anisotropic resistivity inversion scheme on real data where the true model is known. Analogue models are one-step closer to reality than an idealised mathematical (synthetic) model and the data are collected under realistic noise conditions. A physical scale model ("tank") could be built to simulate anisotropic TTI geology. This could be achieved in a number of ways: by carefully layering sand and clay material or by inserting PVC sheets in a preferential alignment or by using micro particles with an anisotropic geometry (i.e. ellipsoidal) that would settle in such a way to provide preferential current flow paths. An anisotropic body could be placed within an isotropic background. A number of different electrode geometries could be employed such as surface, surface-to-borehole, cross-hole, or combinations, with various data sets collected. Comparison of resolution of data sets by eigenanalysis of the Hessian matrix, calculation of resolution matrices and inversion results would be informative for the field practitioners in survey design. However, one drawback of such laboratory studies is the edge-effects of the tank on the resistivity measurements.

Developing improvements in parameterisation and regularisation would aid the accuracy of inversion results. In particular the effect of constraining the level of anisotropy and also anisotropic smoothing functions could be productive areas of future research. It would build on the work of Herwanger *et al.,* (2003) and Li *et al*., (2011).

This inversion methodology is readily extended into 3D experiments. It would be rewarding to numerically investigate tensor measurements in 3-D surface arrays, with current and voltage bipoles in various parallel and perpendicular orientations. An ambitious product of this investigation could be designing a survey capable of delineating effects of anisotropy and inhomogeneity, or simply as a means of detecting anisotropy. If a 3D tank model was built individual measurements could be evaluated for their practical sensitivity on components of the resistivity tensor, and results could be compared with predictions from numerical modelling.

Collecting the complete (linearly independent) data set is cost effective in the field. If repeated measurements are made then a data set with well defined error estimates can be obtained. It is then possible to reconstruct the comprehensive data sets from the complete data set. From a physical point of view, such a data augmentation is not expected to provide additional subsurface information because we are only including linear combinations of the basis set. However, the reconstruction is actually a method of pre-conditioning of the Hessian matrix. It is trivial (algebraic additions) to propagate the errors in the reconstruction process so as to construct a data weighting matrix for the comprehensive data set. Inversion results from comprehensive data sets acquired in the field and different reconstructions from the complete data set could be compared by error estimates and other means.

Appendix Gaussian Quadrature Grid Forward Modelling

The numerical forward modelling routine used in the numerical sensitivity calculation and inversion chapters of this thesis is based upon the Gaussian quadrature grid modelling technique. For a complete derivation and explanation the reader is pointed to the formulations published in: Zhou *et al.,* 2009. The modelling technique was selected because of the ease of incorporating arbitrary topography, heterogeneity and anisotropy. The formulation combines advantageous aspects of the finite element method and the spectral element method, such as the solution of the Variational Principle of the partial differential equation, Gaussian quadrature abscissae and local cardinal functions. The formulation can achieve similar convergence rates to the spectral element method, but does not require the element mesh or element mesh integrations.

A.1 Resistivity Forward Modelling – Basic Equations

The Variational Principle may be applied to 2.5D and 3D resistivity anisotropic forward modelling, in which the governing equations are:

$$2.5D: \begin{cases} \nabla\cdot(\boldsymbol{\sigma}\cdot\nabla G)+k_y^2\sigma_{yy}G=-\frac{1}{2}\delta(r-r_s), & r=(x,z)\in\Omega, \\ (\boldsymbol{\sigma}\nabla G)\cdot\mathbf{n}+\nu G=0, & r=(x,z)\in\Gamma, \end{cases} \tag{A1}$$

$$3D: \begin{cases} \nabla\cdot(\boldsymbol{\sigma}\cdot\nabla G)=-\delta(r-r_s), & r=(x,y,z)\in\Omega, \\ (\boldsymbol{\sigma}\nabla G)\cdot\mathbf{n}+\nu G=0, & r=(x,y,z)\in\Gamma, \end{cases} \tag{A2}$$

Here $\boldsymbol{\sigma}$ is in general a 3×3 symmetric conductivity matrix in the 3D case, $\mathbf{n}$ is the unit normal vector to the boundary Γ, ν is a known function of the spatial coordinates and the conductivity and specifies the mixed boundary condition, r_s is the current point-source location, and G is the Green's function (the potential response to a unit current injection). If the medium has elliptical anisotropy, i.e. defined by the three principal values ($\sigma_{x'x'}, \sigma_{y'y'}, \sigma_{z'z'}$) and with the symmetry-axis in the $\hat{\mathbf{z}}$ direction defined by the orientation angles (φ_0, θ_0).Therefore, we have the functional:

$$\Psi(G)=\frac{1}{2}\{\int_{\Omega}[(\boldsymbol{\sigma}\cdot\nabla G)\cdot\nabla G+k_y^2\sigma_{yy}G^2]d\Omega+\int_{\Gamma}\nu G^2 d\Gamma-G_s\} \tag{A3}$$

and

$$\Psi(G)=\frac{1}{2}\int_{\Omega}[(\boldsymbol{\sigma}\cdot\nabla G)\cdot\nabla G]d\Omega+\frac{1}{2}\int_{\Gamma}\nu G^2 d\Gamma-G_s \tag{A4}$$

for 2.5D and 3D modelling. Here, G_s is the value of G at the source position, which may be expressed by the interpolation formula of the neighbouring points (see the next section).

A.2 Discretization of a 2D Functional

For 2D resistivity modelling, the subsurface is often limited by a computational domain, i.e $(x, z) \in [x_1, x_{N_x}] \times [0, z_0(x)]$, where the function $z_0(x)$ gives the topography of the Earth's surface. The functional given in the previous section may be calculated by summation of successive integrals over the intervals L_i:$[x_i, x_{i+1}]$, (i = 1, 2, …,N_x -1; $N_x \geq 2$) in which the topography $z_0(x)$ is differentiable, i.e. $z_0(x) \in C^1(L_i)$, the integral becomes

$$\int_{\Omega} F(\boldsymbol{\sigma}, G, \nabla G) d\Omega = \sum_{i=1}^{N_x-1} [\int_{x_i}^{x_{i+1}} \int_{0}^{z_0(x)} F(\boldsymbol{\sigma}, G, \nabla G) dx dz], \tag{A5}$$

where the integrand $F(\boldsymbol{\sigma}, G, \nabla G)$ is a function of the conductivity tensor $\boldsymbol{\sigma}$, the field quantity G, e.g., the electric potential in equations (A1) and (A2), and its gradient ∇G, all of which in general vary with the spatial coordinates $(x,y,z) \in \Omega$. In order to calculate the inner integral along the z-axis, we may divide the elevation $Z_0(x)$ into N_z-1 ($N_z \geq 2$) parts and equation (A5) becomes

$$\sum_{i=1}^{N_x-1} [\int_{x_i}^{x_{i+1}} \int_{0}^{z_0(x)} F(\boldsymbol{\sigma}, G, \nabla G) dx dz = \sum_{i=1}^{N_x-1} \sum_{j=1}^{N_z-1} \int_{x_i}^{x_{i+1}} [\int_{\frac{(j-1)z_0(x)}{N_z-1}}^{\frac{z_0(x)}{(N_z-1)}j} F(\boldsymbol{\sigma}, G, \nabla G) dz] dx, \tag{A6}$$

to this we apply the variable replacement

$$\begin{aligned} x(\xi) &= (\frac{x_{i+1} - x_i}{2})\xi + (\frac{x_i + x_{i+1}}{2}), \qquad \xi \in [-1,1], \\ z(\xi,\eta) &= [\frac{z_0(x(\xi))}{2(N_z-1)}](\eta + 2j - 1), \qquad \eta \in [-1,1], \end{aligned} \tag{A7}$$

and obtain the Jacobian matrix:

$$\frac{\partial(x,z)}{\partial(\xi,\eta)} = \begin{vmatrix} \frac{\partial x}{\partial \xi} & \frac{\partial z}{\partial \xi} \\ \frac{\partial x}{\partial \eta} & \frac{\partial z}{\partial \eta} \end{vmatrix} = \frac{(x_{i+1} - x_i) z_0(x)}{4(N_z - 1)}. \tag{A8}$$

applying Gaussian quadrature formulae to the double intervals in equation (A6), yields

$$\begin{aligned} &\int_{x_i}^{x_{i+1}} [\int_{\frac{(j-1)z_0(x)}{(N_z-1)}}^{\frac{z_0(x)}{(N_z-1)}j} F(\boldsymbol{\sigma}, G, \nabla G) dz] dx = \int_{-1}^{1}\int_{-1}^{1} F(\boldsymbol{\sigma}, G, \nabla G) \left|\frac{\partial(x,z)}{\partial(\xi,\eta)}\right| d\xi d\eta \\ &= \sum_{k=1}^{N_\xi^i} \sum_{l=1}^{N_\eta^j} w_k^i w_l^j \frac{(x_{i+1} - x_i) z_0(x(\xi_k))}{4(N_z - 1)} F(\boldsymbol{\sigma}, G, \nabla G)\big|_{(\xi_k, \eta_l)}, \end{aligned} \tag{A9}$$

where (ξ_k, η_l) and (w_k^i, w_l^j) are the Gaussian quadrature abscissae (points) and weights respectively in the 2D case, and they can be analytically calculated once the integers N_ξ^i and N_η^j are given for the sub-domains Ω_{ij}: $[x_i, x_{i+1}] \times [\frac{(j-1)z_0(x)}{(N_z-1)}, \frac{z_0(x)}{(N_z-1)} j]$. Obviously, the Gaussian quadrature abscissae form a grid that spans the whole domain Ω and may easily fit the topography of the Earth's surface. From equation (A9), one can see that the key step is to calculate the values of $F(\boldsymbol{\sigma}, G, \nabla G)$ at the Gaussian quadrature points (ξ_k, η_l), which involves sampling the model parameters $\boldsymbol{\sigma}(x(\xi_k), z(\xi_k, \eta_l))$ and the field quantity $G(x(\xi_k), z(\xi_k, \eta_l))$, and calculating the gradient $\nabla G\big|_{x(\xi_k), z(\xi_k, \eta_l)}$ based on the grid. It is apparent that such grid may give the details of a complex model $\boldsymbol{\sigma}(x,z)$ and the field quantity $G(x,z)$. It differs from the traditional finite element method and the spectral element methods, both of which require a powerful element generator for fitting a complex topography in the modelling and assume that each element has constant model parameters.

In order to calculate the gradient $\nabla G = (\partial G / \partial x, \partial G / \partial z)$, we apply the differential chain rule:

$$\frac{\partial G}{\partial \xi}=\frac{\partial G}{\partial x}\frac{\partial x}{\partial \xi}+\frac{\partial G}{\partial z}\frac{\partial z}{\partial \xi}$$
$$=(\frac{x_{i+1}-x_i}{2})\{\frac{\partial G}{\partial x}+\frac{z_0'(x)}{2(N_z-1)}(\eta+2j-1)\frac{\partial G}{\partial z}\}, \tag{A10}$$

$$\frac{\partial G}{\partial \eta}=\frac{\partial G}{\partial x}\frac{\partial x}{\partial \eta}+\frac{\partial G}{\partial z}\frac{\partial z}{\partial \eta}=\frac{z_0(x)}{2(N_z-1)}\frac{\partial G}{\partial z} \tag{A11}$$

from which we have

$$\frac{\partial G}{\partial x}=\frac{2}{x_{i+1}-x_i}\frac{\partial G}{\partial \xi}-\frac{z_0'(x)}{z_0(x)}(\eta+2j-1)\frac{\partial G}{\partial \eta},$$
$$\frac{\partial G}{\partial z}=\frac{2(N_z-1)}{z_0(x)}\frac{\partial G}{\partial \eta}. \tag{A12}$$

We approximate the field quantity G in the domain $(\xi_k,\eta_l)\in[-1,1]\times[-1,1]$ (see equation A7) by Lagrange interpolation

$$G(\xi,\eta)=\sum_{p=1}^{N_\xi^i}\sum_{q=1}^{N_\eta^j}l_p(\xi)l_q(\eta)G_{pq} \tag{A13}$$

this leads to the derivatives with respect to the Gaussian quadrature points (ξ_k,η_l):

$$(\frac{\partial G}{\partial \xi})_{kl}=\sum_{p=1}^{N_\xi^i}\sum_{q=1}^{N_\eta^j}l_p'(\xi_k)l_q(\eta_l)G_{pq}=\sum_{p=1}^{N_\xi^i}l_p'(\xi_k)G_{pl},$$
$$(\frac{\partial G}{\partial \eta})_{kl}=\sum_{p=1}^{N_\xi^i}\sum_{q=1}^{N_\eta^j}l_p(\xi_k)l_q'(\eta_l)G_{pq}=\sum_{q=1}^{N_\eta^j}l_q'(\eta_l)G_{kq}. \tag{A14}$$

Substituting (A14) for (A12), we obtain the derivatives with respect to the original coordinates (x, z); they are

$$(\frac{\partial G}{\partial x})_{kl}=\sum_{p=1}^{N_\xi^i}(\frac{2}{x_{i+1}-x_i})l_p'(\xi_k)G_{pl}+\sum_{q=1}^{N_\eta^j}\frac{z'(x(\xi_k))}{z(x(\xi_k))}(\eta_l+2j-1)l_q'(\eta_l)G_{kq}$$
$$=\mathbf{N}_x(\xi_k,\eta_l)^T\mathbf{G}^{(x)}, \tag{A15}$$
$$(\frac{\partial G}{\partial z})_{kl}=\sum_{q=1}^{N_\eta^j}\frac{2(N_z-1)}{z(x(\xi_k))}l_q'(\eta_l)G_{kq}=\mathbf{N}_z(\xi_k,\eta_l)^T\mathbf{G}^{(z)},$$

where

$$\mathbf{G}^{(x)}=\mathbf{G}^{(l)}\cup\mathbf{G}^{(k)},\mathbf{G}^{(z)}=\mathbf{G}^{(k)},$$
$$\mathbf{G}^{(l)}=\{G_{pl},p=1,2,...,N_\xi^i\}, \tag{A16}$$
$$\mathbf{G}^{(k)}=\{G_{kq},q=1,2,...,N_\eta^j\},$$

and the components of the vectors $\mathbf{N}_x(\xi_k,\eta_l)$ and $\mathbf{N}_z(\xi_k,\eta_l)$ are calculated as follows:

$$N_x(\xi_k,\eta_l)_p=\begin{cases}(\frac{2}{x_{i+1}-x_i})l_p'(\xi_k), & (1\le p\le N_\xi^i);\\ \frac{z_0'(x(\xi_i))}{z_0(x(\xi_i))}(\eta_l+2j-1)l_p'(\eta_l), & (N_\xi^i<p\le N_\xi^i+N_\eta^j);\end{cases} \tag{A17}$$

$$N_z(\xi_k,\eta_l)_p=\frac{2(N_z-1)}{z_0(x(\xi_k))}l_p'(\eta_l),\quad (1\le p\le N_\eta^j) \tag{A18}$$

According to equation (A15), we have the following vector form of the integrand $F(\boldsymbol{\sigma},G,\nabla G)$ for the 2.5D resistivity case (see equation (A3)):

$$\begin{aligned} F(\boldsymbol{\sigma},G,\nabla G)\big|_{(\xi_k,\eta_l)} &= [\mathbf{G}^{(x)}]^T[\sigma_{xx}(\xi_k,\eta_l)\mathbf{N}_x(\xi_k,\eta_l)\mathbf{N}_x^T(\xi_k,\eta_l)]\mathbf{G}^{(x)} \\ &+ [\mathbf{G}^{(z)}]^T[\sigma_{zx}(\xi_k,\eta_l)\mathbf{N}_z(\xi_k,\eta_l)\mathbf{N}_x^T(\xi_k,\eta_l)]\mathbf{G}^{(x)} \\ &+ [\mathbf{G}^{(z)}]^T[\sigma_{zz}(\xi_k,\eta_l)\mathbf{N}_z(\xi_k,\eta_l)\mathbf{N}_z^T(\xi_k,\eta_l)]\mathbf{G}^{(z)} \\ &+ k_y^2\sigma_{yy}(\xi_k,\eta_l)G_{kl}. \end{aligned} \tag{A19}$$

therefore, equation (A6) becomes

$$\int_{x_i}^{x_{i+1}}\Big[\int_{\frac{(j-1)z_0(x)}{(N_z-1)}}^{\frac{z_0(x)}{(N_z-1)}j} F(\boldsymbol{\sigma},G,\nabla G)dz\Big]dx = \sum_{k=1}^{N_\xi^i}\sum_{l=1}^{N_\eta^j}\Big\{\sum_{\substack{p\in(x,z)\\ q\in(x,z)}}[\mathbf{G}^{(p)}]^T[w_{kl}^{(pq)}\mathbf{N}_p(\xi_k,\eta_l)\mathbf{N}_q^T(\xi_k,\eta_l)]\mathbf{G}^{(q)} + w_{kl}^{(yy)}k_y^2G_{kl}^2\Big\} \tag{A20}$$

where

$$w_{kl}^{(pq)} = \frac{(x_{i+1}-x_i)}{4(N_z-1)}z_0(x(\xi_k))w_k^i w_l^j(\sigma_{pq})_{(\xi_k,\eta_l)} \tag{A21}$$

The boundary integral in equation (A4) may be calculated in terms of the three sides: left (L), right (R) and bottom (B).They are

$$\begin{aligned} \int_L \nu G^2 d\Gamma &= \int_0^{z(x_1)}\nu G^2 dz = \sum_{j=1}^{N_z-1}\int_{\frac{(j-1)z_0(x_1)}{N_z-1}}^{\frac{z_0(x_1)}{N_z-1}j}\nu G^2 d\eta \\ &= \sum_{j=1}^{N_z-1}\sum_{l=1}^{N_\eta^j}\frac{z_0(x_1)}{2(N_z-1)}w_l^j\nu_l G_{jl}^2, \end{aligned} \tag{A22}$$

$$\begin{aligned} \int_R \nu G^2 d\Gamma &= \int_0^{z_0(x_{N_x})}\nu G^2 dz = \sum_{j=1}^{N_z-1}\int_{\frac{(j-1)z_0(x_{N_x})}{N_z-1}}^{\frac{z_0(x_{N_x})}{N_z-1}j}\nu G^2 d\eta \\ &= \sum_{j=1}^{N_z-1}\sum_{l=1}^{N_\eta^j}\frac{z_0(x_{N_x})}{2(N_z-1)}w_l^j\nu_l G_{jl}^2, \end{aligned} \tag{A23}$$

$$\begin{aligned} \int_B \nu G^2 d\Gamma &= \int_{x_1}^{x_{N_x}}\nu G^2 dx = \sum_{i=1}^{N_x-1}\frac{(x_{i+1}-x_i)}{2}\int_{-1}^{1}\nu G^2 d\xi \\ &= \sum_{i=1}^{N_x-1}\sum_{k=1}^{N_\xi^i}\frac{(x_{i+1}-x_i)}{2}w_k^i\nu_k G_{ik}^2. \end{aligned} \tag{A24}$$

Substituting equations (A20)–(A24) for (A3), we finally have the matrix form of the functional for 2.5D resistivity modelling

$$\Psi(\mathbf{G}) = \frac{1}{2}\mathbf{G}^{\mathrm{T}}\mathbf{M}\mathbf{G} + \mathbf{b}_s\mathbf{G}, \tag{A25}$$

where **G** is the vector consisting of the values at all points of the Gaussian quadrature grid, **M** is the matrix assembled by the local matrices $w_{kl}^{(pq)}\mathbf{N}_p(\xi_k,\eta_l)\mathbf{N}_q^T(\xi_k,\eta_l)$ and the coefficients in equations (A20)–(A24) and $\mathbf{b}_s$ is the source vector containing the interpolation functions so that the equation $G_s = \mathbf{b}_s^T\mathbf{G}$ is satisfied. Therefore, the forward modelling reduces to solving the linear equation system:

$$\mathbf{M}\mathbf{G} = \mathbf{b}_s \tag{A26}$$

The dimension of the linear equation system is defined by the number of electrodes used in the survey along with the total number of Gaussian quadrature points. Normally, electric resistivity imaging surveys involve a large number of current electrode positions so that

equation (A26) may have to be solved hundreds of times. In 3D applications, an efficient and accurate linear equation solver is usually required, such as a conjugate gradient method. The banded Cholesky decomposition method ($\mathbf{M} = \mathbf{L}\mathbf{L}^{\mathbf{T}}$) was applied to the linear equation system in the inversion routine used in this thesis. The advantage of the matrix method is that the decomposition is carried out only once for all the current electrodes.

Bibliography

Al-Garnt, M. & Everett, M.E. 2003.The paradox of anisotropy in loop-loop electromagnetic response over a uniaxial halfspace. *Geophysics* **68**, 892-899.

Archie G.E., 1942. The electrical resistivity log as an aid in determining some reservoir characteristics. *Trans. Am. Inst. Min. Metall. Pet. Eng.***146**, 52-62.

Asten, M.W., 1974. The influence of electrical anisotropy on mise-a-la masse surveys: *Geophysical Prospecting* **22**, 238-245.

Athanasiou E.N., Tsourlos P.I. & Papazachos C.B. 2009. Optimizing electrical resistivity array configurations by using a method based on the sensitivity matrix. EAGE *Near Surface*, Extended Abstract, Dublin, September 7-9, 2009.

Barker R.D. 1979. Signal contribution sections and their use in resistivity studies. *Geophysical Journal of the Royal Astronomical Society* **59**, 123 – 129.

Barker R.D., 1981. The offset system of electrical resistivity sounding and its use with a multicore cable. *Geophysical Prospecting* **29**, 128-143.

Bibby H.M., Dawson G.B., Rayner H.H., Stagpoole V.M. & Graham D.J., 1984. The structure of the Mokai geothermal field based on geophysical observations. *Journal of Volcanology and Geothermal Research* **20**(1-2), 1-20.

Bibby, H.M., Rust, G.F., Caldwell, T.G., Heise, W & Bennie, S.L. 2008.Resistivity structure of western Taupo Volcanic Zone, New Zealand. *New Zealand J. Geol. Geophys.* **51**, 231-244.

Bhattacharya, P.K., & H.P. Patra, 1968, Direct Current Geoelectric Sounding: Principles and Applications; Elsevier, Amsterdam.

Blome M., 2009. Efficient measurement and data inversion strategies for large scale geoelectric surveys. PhD thesis, ETH Zurich.

Blome M., Maurer H. & Greenhalgh S.A. 2011. Geoelectric experimental design – Efficient acquisition and exploitation of complete pole-bipole data sets. *Geophysics* **76**, F15-F26.

Boadu, F., Gyamfi, J.& Owusu, E., 2005. Determining subsurface fracture characteristics from azimuthal resistivity surveys: A case study at Nsawam, Ghana. *Geophysics* **70**, B35-B42.

Boerner D.E., West G.F. 1989. Fréchet derivatives and single scattering theory. *Geophysical Journal International* **98**, 385 – 390.

Bolshakov D.K., Pervago E.V., Modin I.N., Shevnin V.A. 1998. New steps in anisotropy studies: arrow-type array. IV EAGE meeting, Barcelona, Spain, proceedings, 857 – 860.

Brown B.H., 2003. Electrical impedance tomography (EIT): a review. *Journal of Medical Engineering and Technology* **27**(3), 97-108.

Broyden, C.G., 1965. A class of methods for solving nonlinear simultaneous equations: *Mathematics of Computation* **19**, 577-593.

Buckley R.G., Staines M.P., Robinson W.H., 1986. In situ measurements of the resistivity of Antarctic sea ice. *Cold Reg. Sci. Technol*. **12**, 285 – 290.

Busby J.P. 2000. The effectiveness of azimuthal apparent resistivity measurements as a method for determining fracture strike orientations. *Geophysical Prospecting* **48**, 677-698.

Busby, J., Jackson, P., 2006. The application of time-lapse azimuthal apparent resistivity measurements for the prediction of coastal cliff failure. *Journal of Applied Geophysics* **59**, 261-272.

Butler D. ed. 2005. Near Surface Geophysics. Society Exploration Geophysics, Tulsa.

Caldwell T.G. & Bibby H.M., 1998. The instantaneous apparent resistivity tensor: a visualisation scheme for LOTEM electric field measurements. *Geophysical Journal International* **135**, 817-834.

Cassiani, G., Godio, A., Stocco, S., Villa, A., Deiana, R., Frattini, P., 2009. Monitoring the hydrologic behaviour of a mountain slope via time-lapse electrical resistivity tomography. *Near Surface Geophysics* **7**(5-6), 475-486.

Claerbout J.F. and Muir F., 1973. Robust modelling with erratic data. *Geophysics* **38**(1), 826 – 844.

Collins J.L., Everett M.E. & Johnson B., 2006. Detection of near surface horizontal anisotropy in a weathered metamorphic schist by transient electromagnetic induction. *Physics of the Earth and Planetary Interior* **158**, 159-173.

Dahlin T., 1989. The development of a cable system for vertical electrical sounding and a comparsion of the Schlumberger and Offset Wenner methods. PhD thesis, Lund University.

Dahlin T., 2000. Short note on electrode charge-up effects in DC resistivity data acquisition using multi-electrode arrays. *Geophysical Prospecting* **48**(1), 181-187.

deGroot-Hedlin C., Constable S., 1990. Occam's inversion to generate smooth, two dimensional models from magnetotelluric data. *Geophysics* **55**, 1613-1624.

Dekker D.L. & Hastie L.M. 1980. Magnetotelluric impedance of an anisotropic layered earth model. *Geophysical Journal Royal Astronomical Society* **61**, 11-20.

Doetsch L., Linde N., Coscia I., Greenhalgh S. & Green A., 2010. Zonation for 3D aquifer characterization based on joint inversions of multi-method cross-hole geophysical data. *Geophysics* **75**(6), G53-G64.

Dorn O., Bertete-Aguirre H., Berryman J.G., Papnicolaou G.C., 2002. Sensitivity analysis of a nonlinear inversion method for a 3D electromagnetic imaging in anisotropic media. *Inverse Problems* **18**, 285-317.

Ellis, R.G., Oldenburg, D.W., 1994. Applied geophysical inversion. *Geophysical Journal International* **116**, 5-11.

Eloranta, E.H., 1988. The modelling of mise-a-la masse anomalies in an anisotropic half space by the integral equation method. *Geoexploration* **25**, 93-101.

Everett M.E & Constable S.C., 1999. Electric dipole field over an anisotropic seafloor. Theory and approach to the structure of the 40MA Pacific Ocean lithosphere. *Geophysical Journal International* **136**, 41-56.

Farquharson C.G. & Oldenburg D.W., 1998. Non-linear inversion using general measures of data misfit and model structure. *Geophysical Journal International* **134**, 213-227.

Friedel S., 2003. Resolution, stability and efficiency of resistivity tomography estimated from a generalized inverse approach. *Geophysical Journal International* **153**, 305 – 316.

Fujino K. and Suzuki Y., 1963. An attempt to estimate the thickness of sea ice by electrical resistivity method II. *Low Temp. Sci.* **A21**, 151 - 157

Furman A., Ferre T.P.A., Warrick A.W. 2003. A sensitivity analysis of electrical resistivity tomography array types using analytical element modelling. *Vadose Zone* **2**, 416 - 423.

Ghosh D.P., 1971. The application of linear filter theory to the direct interpretation of geoelectrical resistivity sounding measurements. *Geophysical Prospecting* **19**, 192-217.

Gianzero S. 1999. The Paradox of Anisotropy revisited. *The Log Analyst* **40**, No. 6.

Gish O. and Rooney W., 1925. Measurement of resistivity of large masses of undisturbed Earth. *Journal of Geophysical Research*, **30**(4), 161-188.

Geselowitz D.B. 1971. An application of electrocardiographic lead theory to impedance plethysmography. *.IEEE Transactions on Biomedical Engineering* **18**, 38-41.

Grant F.S., West G.F. 1965. Interpretation theory in applied geophysics. McGraw-Hill.

Greenhalgh M., 2008. DC resistivity modelling and sensitivity analysis in anisotropic media. PhD thesis, University of Adelaide.

Greenhalgh S.A., Zhou B. & Green A., 2006. Solutions, algorithms and inter-relations for local minimization search geophysical inversion. *Journal of Geophysics and Engineering* **3,** 101.

Greenhalgh S.A., Zhou B., Greenhalgh M., Marescot L. and Wiese T. 2009a. Explicit expressions for the Fréchet derivatives in 3D anisotropic resistivity inversion. *Geophysics* **74**, F31-F43.

Greenhalgh S.A., Marescot L., Zhou B., Greenhalgh M., Wiese T., 2009b. Electric potential and Fréchet derivatives for a uniform anisotropic medium with a tilted axis of symmetry. *Pure and Applied Geophysics* **166**, 673 – 699.

Greenhalgh S.A., Wiese T. & Marescot L., 2010. Comparison of DC sensitivity patterns for anisotropic and isotropic media. *Journal of Applied Geophysics* **70**, 103-112.

Habberjam, G.M., Watkins, G.E., 1967. The use of a square configuration in resistivity prospecting. *Geophysical Prospecting* **15**, 445-467.

Habberjam G.M., 1972. The effects of anisotropy on square array resistivity measurements. *Geophysical Prospecting* **20**, 249-266.

Habberjam G.M., 1975. Apparent resistivity, anisotropy and strike measurements. *Geophysical Prospecting* **23**, 211-247.

Hagrey, S.A., 1994. Electric study of fracture anisotropy at Falkenberg, Germany. *Geophysics* **59**, 881-888.

Hamilton, M.P., Jones, A.G., Evans, R.L., Eavns, S., Fourie, C.J.S., Garcia, X., Mountford, A., Spartt, J.E., 2006. Electrical anisotropy of South African lithosphere compared with seismic anisotropy from shear-wave splitting analyses. *Physics of the Earth and Planetary Interiors* **158**, 226-239.

Hansen P.C.,& O'Leary D.P., 1993. The use of l-curve in the regularization of discrete ill-posed problems. *SIAM J. Sci. Comput.* **14**, 1487 -1503.

Hart D. & Rudman A.J., 1997. Least-squares fit of an ellipse to anisotropic polar data: Application to azimuthal resistivity surveys in karst. *Computers and Geoscience* **23**(2), 189-194.

Herwanger J.V., Pain C.C., Binley A., de Oliveira C.R.E. & Worthington M.H., 2004. Anisotropic resistivity tomography. *Geophysical Journal International* **158**, 409-425.

Hill, D.G., 1972. A laboratory investigation of electrical anisotropy in Precambrian rocks. *Geophysics* **37**, 1022-1038.

Ingham M., Pringle D. & Eicken H., 2008. Cross-borehole resistivity tomography of sea ice. *Cold Regions Science and Technology* **52**, 263-277

Inman J.R., 1975. Resistivity inversion with ridge regression. *Geophysics* **40**, 798 – 917.

Keller, G.V., Frischknecht, F.C, 1966. Electrical Methods in Geophysical Prospecting, Pergamon.

Keller G.V., 1998. Rock and Mineral Properties, in Nabighian, M.N. (ed) Electromagnetic Methods in Applied Geophysics, Volume 1, Theory: Society of Exploration Geophysicists, Tulsa, 13-52.

Kim J., Yi M., Cho S., Son J. & Song W. 2006. Anisotropic crosshole resistivity tomography for ground safety analysis of a high-storied building over an abandoned mine. *Journal of Environmental and Engineering Geophysics* **11**, 225-235.

Kupke M., Schulte K. & Schuler R., 2001. Non-destructive testing of FRP by d.c. and a.c. electrical methods. *Composites Science and Technology* **61**(6), 837-847.

Kunz, K.S., Moran, J.H., 1958. Some effects of formation anisotropy on resistivity measurements in boreholes. *Geophysics* **23**, 770-794.

LaBreque D.J., Heath G, Sharpe R. & Versteeg R. 2004. Autonomous monitoring of fluid movement using 3-D electrical resistivity tomography. *Journal of Environmental and Engineering Geophysics* **9**, 167-176.

LaBrecque D. & Daily W., 2008. Assessment of measurement errors for galvanic-resistivity electrodes of different composition. *Geophysics* **73**(2), F55.

Lane, J.W., Haeni, F.P. Watson, W.M., 1995. Use of square array direct current resistivity methods to detect fractures in crystalline bedrock in New Hampshire. *Ground Water* **33**, 476-485.

Lehmann H., 1995. Potential representation by independent configurations on a multi-electrode array. *Geophysical Journal International* **120**(2), 331-338.

Le Masne D. & Vasseur G. 1981. Electromagnetic field of sources at the surface of a homogeneous halfspace with horizontal anisotropy: application to fissured media. *Geophysical Prospecting***29**, 803-821.

Lesur, V., M. Cuer, & A., Starch, 1999, 2D and 3D interpretation of electrical tomography experiments, Part 2: the inverse problem. *Geophysics* **64**, 396-402.

Li, P., & N.F. Uren, 1994, Analytical solution for the electric potential due to a point source in an arbitrarily anisotropic half-space. *Journal Engineering Mathematics* **33**, 129-140.

Li. X & Pedersen L.B. 1991. The electromagnetic response of an azimuthally anisotropic halfspace. *Geophysics* **56**, 1462-1473.

Li X.& Pedersen L.B. 1992. Controlled-source tensor magnetotelluric observation of a layered earth with azimuthal anisotropy. *Geophysical Journal International* **111**, 91-103.

Li Y. & Spitzer K., 2005. Finite element resistivity modelling for three-dimensional structures with arbitrary anisotropy. *Physics of the Earth and Planetary Interior* **150**, 15 - 27.

Linde, N., Pederson, L.B., 2004. Evidence of electrical anisotropy in limestone formations using the RMT technique. *Geophysics* **69**, 909-916.

Loewenthal D.& Landisman M., 1973. Theory for magnetotelluric observation on the surface of a layered anisotropic half-space. *Geophysical Journal of the Royal Astronomical Society* **35**, 195-214.

Loke, M.H., & Barker, R.D., 1995. Least-squares deconvolution of apparent resistivity pseudosections. *Geophysics* **60**, 1682-1690.

Loke, M.H., Barker R.D., 1996. Rapid least squares inversion of apparent resistivity pseudosections by a quasi-Newton method. *Geophysical Prospecting* **44**, 131-152.

Loke M.H., Wilkinson P.B., Chambers J.E., 2010. Fast computation of optimized electrode arrays for 2D resistivity surveys. *Computers and Geosciences* **36**, 1414 – 1426.

Lowry T., Allen M.B. & Shive P.N., 1989. Singularity removal: A refinement of resistivity modelling techniques. *Geophysics* **54**(6), 766 – 774.

Lu X., Alumbaugh D.L. & Weiss C.J., 2002. Electric fields and currents produced by induction logging instruments in anisotropic media. *Geophysics* **67**, 478-483.

Maillet R., 1947. The fundamental equations of resistivity prospecting. *Geophysics* **12**, 529-556.

Matias, M.J.S., Habberjam, G.M., 1986. The effect of structure and anisotropy on resistivity measurements. *Geophysics* **51**, 964-971.

Matias, M.J.S., 2002. Square array anisotropy measurements and resistivity sounding interpretation. *Journal of Applied Geophysics* **49**, 185-194.

Maurer H. & Freidel S., 2006. Outer space sensitivities in geoelectrical tomography. *Geophysics* **71**, G93-G96.

McGillivray, P.R, Oldenburg D.W., 1990. Method for calculating Fréchet derivatives for the non-linear inverse problem: a comparative study. *Geophysical Prospecting* **38**, 499-524.

Mendelson K. & Cohen M.H., 1982. The effect of grain anisotropy on the electrical properties of sedimentary rocks. *Geophysics* **47**(2), 257-263.

Menke W. 1989. Geophysical data analysis: Discrete inverse theory. Academic Press.

Marescot L., Rigobert S., Palma-Lopes S., Lagabrielle R. and Chapellier D., 2006. A generalised approach for DC apparent resistivity evaluation on arbitrarily shaped 3D structures. *Journal of Applied Geophysics* **60**(1), 55-67.

Moran, J.H., Gianzero, S., 1979. Effects of formation anisotropy on resistivity-logging measurements. *Geophysics* **44**, 1266-1286.

Nguyen, F., Garambois, S., Chardon, D., Hermite, D., Bellier, O., Jongmans, D., 2007. Subsurface electrical imaging of anisotropic formations affected by a slow active reverse fault, Provence, France. *Journal of Applied Geophysics* **62**, 338-353.

Noel M., Biwen X., (1991). Archaeological investigation by electrical resistivity tomography: a preliminary study. *Geophysical Journal International* **107**(1), 95-102.

Novák, A., Szarka, L., Varga, M., Szalas, S., Pap, Z & Károlyi, A., 2004. Tensor invariant based electrical potential mapping, and its use in an archaeological field study. Proceedings of 17th Workshop, Electromagnetic Induction in the Earth, Hyderabad, India, October 18-23.

Nunn, K.R., Barker, R.D., Bamford, D., 1983. In situ seismic and electrical measurements of fracture anisotropy in the Lincolnshire Chalk. *Quart. Journal of Engineering Geology and Hydrogeology* **16**, 187-195.

O'Brien D.P. & Morrison H.F., 1967. Electromagnetic fields in an n-layer half-space. *Geophysics* **32**, 668-677.

Oldenburg D.W., 1978. The interpretation of direct current resistivity measurements. *Geophysics* **43**, 610 – 625.

Owens W.H. & Bamford D., 1976. Magnetic, seismic and other anisotropic properties of rock fabrics. *Phil. Trans. R. Soc. Lond. A.* **283**, 55 – 68.

Pain C., Herwanger J., Saunders J, Worthington M & de Oliveira C. 2003. Anisotropic resistivity inversion. *Inverse Problems* **19**, 1081-1111.

Palacky G.J., 1987. Resistivity characteristics of geological targets. In: NabighianMN (ed) Electromagnetic methods in applied geophysics. Society of Exploration Geophysicists, Tulsa.

Papadopolous N.G., Tsourlous P., Papazachos C., Tsokas G.N., Sarris A., Kim J.H., 2011. An algorithm for fast 3D inversion of surface electrical resistivity tomography data: application on imaging buried antiquities. *Geophysical Prospecting* **59**(3), 557 -575.

Park, S.K., Van, G.P., 1991. Inversion of pole-pole data for 3-D resistivity structure beneath arrays of electrodes. *Geophysics* **56**, 951-960.

Parkomenko E.I., 1967. Electrical properties of rocks: Plenum Press.

Patera A., 1984. A spectral element method for fluid dynamics – laminar flow in a channel expansion. *Journal of Computational Physics* **54**, 468 – 488.

Penttinen, S., Sutinen, R., Hanninen, P., 1999. Determination of anisotropy of tills by means of azimuthal resistivity and conductivity measurements. *Nordic Hydrology* **30**, 4-5.

Pervago, E., Ousatov, A., & Shevnin, V., 2006. Analytic solution for the electric potential in arbitrary anisotropic layered media applying the set of Hankel transforms of integer order. *Geophysical Prospecting* **54**, 651-661.

Pettifer G., Wood W., O'Neill D.J., Bradley J., Baker P., Bolton H., Pratt M., Llewellyn B. & Macauley S., 2000. Bundaberg Groundwater Project – A unique groundwater geophysics and hydrogeological case study, ASEG, October, 25 – 30.

Plattner A., 2011. Adaptive wavelet methods for geoelectric modelling and inversion. PhD Thesis, ETH Zurich , Switzerland.

Ritzi R.W., Andolsek R.H. 1992. Relation between anisotropic transmissivity and azimuthal resistivity surveys in shallow, fractured, carbonate flow systems. *Ground Water* **30**, 774-780.

Reddy I.K. & Rankin D., 1971. Magnetotelluric effect of dipping anisotropies. *Geophysical Prospecting* **19**, 84-97.

Rey E. & Jongmans D., 2007. A 2D numerical study of the effect of particle shape and orientation on resistivity in shallow formations. *Geophysics*, **72**(1) F9-F17

Reynolds J.M., 2011. An Introduction to Applied and Environmental Geophysics. John Wiley & Sons, New York.

Roy A., Apparao A., 1971. Depth of investigation in direct current methods. *Geophysics* **36**, 943-959.

Robinson E.S. & Coruh C., 1988. Basic exploration geophysics. John Wiley & Sons Ltd.

Rubin Y. & Hubbard S, 2005. Hydrogeophysics. Springer Netherlands.

Rucker D.F., Fink J.B. & Loke M.H., 2011. Environmental monitoring of leaks using time lapsed long electrode electrical resistivity. *Journal of Applied Geophysics* **74**(4), 242-254.

Samouelian, A., Richard, G., Cousin, I., Guerin, R., Bruand, A., Tabbagh, A., 2004. Three-dimensional crack monitoring by electrical resistivity measurement. *European Journal of Soil Science* **55**, 751-762.

Sasaki, Y., 1994. 3-D resistivity inversion using the finite element method. *Geophysics* **59**, 1839-1848.

Schon J.H., 1976. The Physical Properties of Rocks: Fundamentals and Principles of Pertrophysics. Pergamon, New York.

Schlumberger C., 1920. Etude sur la Prospection Electrique du Sous-sol. Gaulthier-Villars etCie, Paris.

Schmutz M., Andrieux P., Bobachev A., Montoroi J.P. & Nasri S., 2006. Azimuthal resistivity surveying over a steep dipping anisotropic formation: a case history in central Tunisia. *Journal of Applied Geophysics* **60**, 213-224.

Shima, H., 1992. 2-D and 3-D resistivity imaging reconstruction using crosshole data. *Geophysics* **55**, 682-694.

Sinha A.K. & Bhattacharya P.K., 1967. Electric dipole over an anisotropic and inhomogeneous earth. *Geophysics* **32**, 652-667.

Skinner D., Heinson G., 2004. A comparison of electrical and electromagnetic methods for the detection of hydraulic pathways in a fractured rock aquifer, Claire Valley, South Australia. *Hydrogeology Journal* **12**(5) 576-590.

Skjernaa L. & Jorgensen N.O., 1993. Detection of local fracture systems by azimuthal resistivity surveys: examples from south Norway: Memoirs of the 24th Congress of International Assn. Hydrogeologists, 662 – 671.

Slater L., Sandberg S.K. & Jankowski M., 1998. Survey design procedures and data processing techniques applied to the EM azimuthal resistivity method. *Journal of Environmental Engineering Geophysics* **3**, 167-177.

Smith N.C., Vozoff K., 1984. Two-dimensional DC resistivity inversion for dipole-dipole data. *IEEE Geoscience and Remote Sensing* **GE 22**, 21-28.

Spitzer, K., 1998. The three-dimensional DC sensitivity for surface and subsurface sources. *Geophysical Journal International* **134**, 736-746.

Stummer P., 2003.New developments in electrical resistivity imaging. PhD Thesis, ETH Zurich, Switzerland.

Stummer P., Maurer H.R., Green A.G., 2004. Experimental design: electrical resistivity data sets that provide optimum subsurface information. *Geophysics* **69**, 120 – 139.

Szalai S., Szarka L., 2000. An approximate analytical approach for computing geoelectric response due to a small buried cube. *Geophysical Prospecting* **48**, 871-885.

Szalai S., Szarka L., 2002. Geoelectric mapping of near-surface karstic fractures by using null-arrays. *Geophysics* **67**, 1769-1778.

Szalai S., Szarka L., 2008a. Parameter sensitivity maps of surface geoelectric arrays, I. Linear arrays. *Acta. Geod. and Geoph.. Mont* **43**, 419-437.

Szalai S., Szarka L. 2008b. Parameter sensitivity maps of surface geoelectric arrays, II. Nonlinear and focussed arrays. *Acta. Geod. and Geoph. Mon* **43**, 439-447.

Szalai S., Szarka L. 2008. On the classification of surface geoelectric arrays. *Geophysical Prospecting* **56**, 159 – 175.

Taylor, R.W., Fleming, A.H., 1988. Characterising jointed systems by azimuthal resistivity surveys. *Ground Water* **26**, 464-474.

Tarantola A., 1978. Inverse Problem Theory. Elsevier, Amsterdam.

Telford W.M., Geldart L.P., Sheriff R.E. & Keys D.A., 1990. Applied Geophysics. Cambridge University Press.

Thomsen L., 1986. Weak elastic anisotropy. *Geophysics* **51**(10), 1954-1966.

Timco G.W., 1979. An analysis of the in-situ resistivity of sea ice in terms of its microstructure. *J. Glaciolology*. **22**, 461 – 471.

Thyssen F., Kohnen H., Cowan M.V., Timco G.W., 1974. DC resistivity measurements on the sea ice near pond inlet, N.W.T. (Baffin Island). *Polarforschung* **44**, 117 – 126.

Travelletti J., Sailhac P., Malet J.-P., Grandjean G., Ponton J., 2011. Hydrological response of weathered clay-shale slopes: water infiltration monitoring with time-lapse electrical resistivity tomography. *Hydrological Processes* **25**, 617-628.

Tripp A., Hohmann G.W. & Swift C.M., 1984. Two dimensional resistivity inversion. *Geophysics* **49**(10), 1708-1717.

Tsokas G.N., Tsourlos P.I., Szymanski J.E., 1997. Square array resistivity anomalies and inhomogeneity ratio calculated by the finite-element method. *Geophysics* **62**(2) 426 – 435.

Vogel C.R., 2002. Computational Methods for Inverse Problems. Frontiers in applied mathematics. Society for Industrial and Applied Mathematics.

Wannamaker, P.E., 2005. Anisotropy versus heterogeneity in continental solid earth electromagnetic studies: fundamental response characteristics and implications for physicochemical state. *Surveys in Geophysics* **26**, 733-765.

Wang T. & Fang S., 2001. 3-D electromagnetic anisotropy modelling using finite differences. *Geophysics* **66**, 1386-1398.

Ward S.H, 1990. Geotechnical and Environmental Geophysics. Investigations in Geophysics No. 5. Society of Exploration Geophysicists.

Watson K.A., Barker R.D., 1999. Differentiating anisotropy and lateral effects using azimuthal resistivity offset Wenner soundings. *Geophysics* **64**, 739-745.

Weller A., Gruhne M., Scichter M., Borner F.D., 1996. Monitoring hydraulic experiments by complex conductivity tomography. *Journal of Environmental Engineering and Geophysics* **1**, 209 – 228.

Wilkinson P. B., Meldrum P.I., Chambers J.C., Kuras O., Ogilvy R.D., 2006. Improved strategies for the automatic selection of optimized sets of electrical resistivity tomography measurement configurations. *Geophysical Journal International* **167**, 1119 – 1126.

Wilkinson, P.B., Meldrum, P.I, Kuras, O., Chambers, J.E., Holyoake, S.J. & Ogilvy, R.D. 2010 . High-resolution electrical resistivity tomography monitoring of a tracer test in a confined aquifer. *Journal of Applied Geophysics* **70**(4), 268-276.

Weiss C.J. & Newman G.A., 2002. Electromagnetic induction in a fully 3D anisotropic earth. *Geophysics* **67**, 1104-1114.

Wiese T., Greenhalgh S.A. & Marescot L., 2009. DC resistivity sensitivity patterns for tilted transversely isotropic media. *Near Surfac eGeophysics* **7**, 125 – 139.

Wilkinson P.B., Meldrum P.I., Chambers J.E., Kuras O. & Ogilvy R.D., 2006. Improved strategies for the automatic selection of optimized sets of electrical resistivity tomograph measurements configurations. *Geophysical Journal International* **167**, 1119-1126.

Wilson, T., Heinson, G., Endres, A., Halihan, T., 2001. Fractured rock geophysical studies in the Clare Valley, South Australia. *Exploration Geophysics* **31**, 255-259.

Wishart, D.N., Slater, L.D. & Gates, A., 2006. Azimuthal geoelectric characterization of fracture flow in the New Jersey highlands bedrock: Geological Society of America, annual meeting, **38**(7), 26.

Xu B., Noel M., 1993. On the completeness of data sets with multi-electrode systems for electrical resistivity surveys. *Geophysical Prospecting* **41**, 791-801.

Yi M.J., Kim J.H. & Chung S.H., 2003. Enhancing the resolving power of least-squares inversion with active constraint balancing. *Geophysics* **68**, 931 – 941.

Yi M.J., Kim J.H. & Chung S.H., 2011. Three-dimensional anisotropic inversion of resistivity tomography data in an abandoned mine area. *Exploration Geophysics* **42**, 7-17.

Ying C. & Wiedelt P., 1999. Geoelectrical fields in a layered Earth with arbitrary anisotropy. *Geophysics* **64**, 426-434.

Yin C. & Maurer H.M., 2001. Electromagnetic induction in a layered Earth with arbitrary anisotropy. *Geophysics* **66**, 1405-1415.

Yin C. & Fraser D., 2004. The effect of electrical anisotropy on the response of helicopter-borne frequency-domain electromagnetic systems. *Geophysical Prospecting* **52**, 399-416.

Zhe J.P., Greenhalgh S., Marescot L., 2007. Multichannel full waveform and flexible electrode combination resistivity imaging system. *Geophysics* **72**, F57-F64.

Zhou, B. & Greenhalgh S.A., 1999. Explicit expressions and numerical computation of the Fréchet and second derivatives in 2.5D Helmholtz equation inversion. *Geophysical Prospecting* **47**, 443-468.

Zhou B. & Greenhalgh S.A., 2000. Crosshole resistivity tomography using different electrode configurations. *Geophysical Prospecting* **48**, 887-912.

Zhou B. & Greenhalgh S.A., 2002. Rapid 2-d/3-d crosshole resistivity imaging using the analytic sensitivity function. *Geophysics* **67**(3), 755-765.

Zhou, B., Greenhalgh, M., Greenhalgh, S.A., 2009. 2.5D/3D resistivity modelling in anisotropic media using Gaussian quadrature grids. *Geophysical Journal International* **176**(1), 938-950.